

## Editorial corner – a personal view

### Knowledge and technology transfers: What is going on?

*J. Karger-Kocsis\**

Department of Polymer Engineering, Faculty of Mechanical Engineering, Budapest University of Technology and Economics, Műegyetem rkp. 3., H-1111, Budapest, Hungary

Grouping in materials science usually distinguishes ceramics, metals and polymers. Their developments were never independent of each other though sometimes the interaction might have been implicit (for example between metallic alloys and polymer blends). New findings, achieved with one of the above materials triggered interest to copy them in the others. The related knowledge transfer was, however, not always smooth. For example the concept of phase transformation toughening, working well in metals and especially in ceramics, could not be adapted for polymers (at least according to the original principle). By contrast, the success with shape memory alloys is the present driving force for the extensive research on shape memory polymers ('forerunners' of which were termed to heat shrinkable systems). Sol-gel techniques of ceramics' production are now adapted to prepare polymer nanocomposites. The winners among the research concepts were always those that have been 'borrowed' from the nature. The related bioinspired, biomimetical approaches have been followed in materials' development (self healing – not restricted for polymeric materials), design and construction (skeletal framing, local reinforcements), and even in the production (lean manufacturing, net shape processing). A strong interplay can be noticed also for processing/shaping technologies. Again, the related transfer was not always a success story. For example roll forming, extensively used for metallic sheets, did not reach breakthrough with polymeric

composites. On the other hand, the equal channel angular pressing/extrusion of metals is now a preferred research direction for polymers. This technology represents the revival of the solid phase forming processes of polymers whereby the knowledge and know-how, acquired for metals, are being fully exploited. Another recent 'metal triggered' development for polymers and related composites concerns joining. Friction stir welding for example seems to be well adaptable for polymeric systems. Solid phase high-energy ball milling, well established for the preparation of special metals and ceramics, may be a useful tool to disperse carbon nanotubes in suitable oligomers and polymers. How to keep updated with such 'transfer phenomena'? First, do not attend only the lectures of your peers at conferences, and second, as scientist or engineer be always ready to face new challenges. To be able to think in analogies is the minimum task for researchers, is not it?



Prof. Dr. Dr. h. c. József Karger-Kocsis  
Editor-in-Chief

\*Corresponding author, e-mail: [karger@pt.bme.hu](mailto:karger@pt.bme.hu)  
© BME-PT

# Thermo-mechanical characterization of epoxy nanocomposites with different carbon nanotube distributions obtained by solvent aided and direct mixing

A. Martone, C. Formicola, F. Piscitelli, M. Lavorgna, M. Zarrelli\*, V. Antonucci, M. Giordano

CNR – Research National Council, IMCB – Institute for Composite and Biomedical Materials, P.le E. Fermi 1, 80055 Portici, Italy

Received 24 October 2011; accepted in revised form 19 January 2012

**Abstract.** Two different routes, namely solvent aided dispersion and direct mixing, were employed to disperse Multi-Walled Carbon Nanotubes (MWCNTs) into a mono-component epoxy system used as matrix for advanced composites. In the first route, MWCNTs were diluted in three different solvents (acetone, sodium dodecyl sulfate and ethanol) and then mixed with the matrix by tip sonication. In the second case, carbonaceous nanoparticles were added directly into the hosting system and dispersion was carried out by using three different techniques (mechanical stirring, magnetic agitation and tip sonication). The effects of the solvents and agitation energy were investigated by optical microscopy at micron level, in order to assess the more efficient dispersion procedure for the considered epoxy system. It was demonstrated that parameters associated with direct mixing rather than solvent solubility govern MWCNT dispersion. Optical analysis of the nanocomposite morphology evidenced a very low density of MWCNTs micron sized aggregates in the case of direct mixed tip sonicated samples if compared to those obtained by solution aided dispersion. In addition, nanocomposites obtained by sonication showed the lowest density of MWCNTs micron sized aggregates, also when compared with mechanically and magnetically stirred system.

Dynamic Mechanical Analysis (DMA) and Thermo-Mechanical Analysis (TMA) results confirm the final result that among the considered direct mixing techniques, the direct tip sonication represents the most efficient route for MWCNT dispersion. Moreover, the mixing temperature of the hosting matrix system represents a fundamental feature in enhancing the MWCNT de-bundling and dispersion.

Small X-ray Scattering analysis revealed that a nanosized structure of nanotubes is formed in the case of the tip sonicated samples that is heuristically correlated with both the maximum enhancement of mechanical modulus and the maximum reduction of thermal expansion coefficients.

**Keywords:** nanocomposites, processing technologies, thermosetting resins

## 1. Introduction

The continuous demand for new high performance polymer composite for sectors as aerospace or lightweight structures for various structural elements has led many researchers to investigate the potential application of the CNT as nano-reinforcements for polymer matrix of fiber-reinforced composite. Polymer/CNT composites have attracted consider-

able attention due to their unique mechanical, surface, multi-functional properties and strong interactions with the matrix, depending on the nano-scale microstructure and large interfacial area [1–5]. Moreover, their impressive mechanical properties with stiffness and strength values falling within the range 100–1800 GPa and 2.5–3.5 GPa respectively, make them ideal candidates to develop novel com-

\*Corresponding author, e-mail: [mauro.zarrelli@imcb.cnr.it](mailto:mauro.zarrelli@imcb.cnr.it)

posites based on advanced polymer matrices [6–7]. Epoxy nanocomposite matrix could be the ideal solution for a new generation of composite materials: at mesoscopic level, for example, to attenuate the mismatch of thermal expansion coefficient between the reinforcement and the matrix system or to enhance matrix-based property; while at macro-level to reduce the development of residual stresses due different volume variations between the tooling materials and composite element. The dispersion process of carbon nanotubes represents a very complex phenomenon due to their natural tendency to bundle together due to van der Waals interactions. Nanotube attraction and, thus, bundle formation, are based on chemical and physical features: for single CNT, in fact, the attractive energy is of the order of 0.5 eV (about  $0.8 \cdot 10^{-19}$  J) per nanometer of nanotube-to-nanotube contact [8] at ambient temperature, for a 10 nm nanotube length this force increases to the order of 200 kJ/mol, which is equivalent to a typical covalent bond. The non-uniform dispersion due to microscopic nanotubes aggregates leads to many defect sites and resin-rich area limiting not only the efficiency of CNTs as reinforcement fillers for the polymer composite matrix [9–12], but also the electrical properties and the percolation threshold [13–15]. In the published literature [16–20], various techniques have been reported to disperse nanotubes in either thermosets or thermoplastics polymer resins. Among others, solvent aided dispersion and direct mixing stand as the most capable and efficient methodologies. Solution dispersion can be considered a suitable technique [21, 22], especially in the case of thermosets, even though some difficulties could arise from the choice of the most appropriate solvent and processing conditions (i.e. temperature and time). Solvent aided dispersion is carried out generally by a two-stage procedure, which includes firstly, the dispersion of nanotubes in the selected solvent (solvent mixing) and, then, the addition of the resin for the final mixing (resin solution mixing). Among different solvents, acetone and ethanol are the most common materials enabling the carbon nanotubes dispersion. The effect of acetone and ethanol on the properties of SWCNTs (0.5 wt%) epoxy nanocomposites was investigated in [22]. In particular, it was found that the acetone-SWCNTs dispersed samples are characterized by greater size of SWNT bundles diameter

and, conversely, higher values of hardness and flexural strength than those of ethanol-SWCNTs dispersed samples. Further, to disaggregate and uniformly disperse carbon nanotubes, another extensively studied approach is the use of surfactants [23] by altering the surface chemistry of the tubes either covalently (functionalization) or non-covalently (adsorption). Ionic surfactants are preferable for CNT/water-soluble solutions. Alternatively, non-ionic surfactants are proposed when organic solvents have to be used. Among the ionic surfactants, sodium dodecyl sulphate (SDS) and dodecyl-benzene sodium-sulfonate (NaDDBS) were commonly used to decrease CNT aggregative tendency in water. In particular, SDS is characterized by a hydrophilic and hydrophobic head at its end. Diluted in a water solution, SDS operates a separation of the nanotube agglomerates by intercalating the carbonaceous nano-structures [23] and the water molecules by chemical interaction at its ends. This effect will be lost during the degassing procedure as dense nanotube aggregations will form, while the solvent evaporates and the resin lowers its viscosity. Direct mixing operates directly on the mixture of (pristine or purified) nanotubes and hosting system, without any pre-dispersion stage. This single-stage procedure leads to a nanotubes/resin mixture directly used as matrix for composite materials. Various mixing techniques (i.e. magnetic stirring, roll milling, mechanical agitation or high-energy sonication) have been employed for both procedures to achieve dispersion and homogenization of CNT within the polymer matrix. However, achieved results in terms of repetitive morphology and performance of the final nanocomposite are still controversial and scattered [24, 25]. Nanomechanics and characterization testing of nanocomposite samples have shown that enhancement of the mechanical and electrical behaviour of the final nanocomposite is strongly dependent upon the level of dispersion and the final morphology of the nanofillers.

A review of the available literature data on mechanical elastic modulus of nanofilled resin was reported in [24]. Successful modelling of the data variability was achieved by introducing two fundamental features associated to nanofiller dispersed within a hosting matrix such as their effective aspect ratio (i.e. actual length over nominal diameter of the nanostructures) and excluded volume. Figure 1

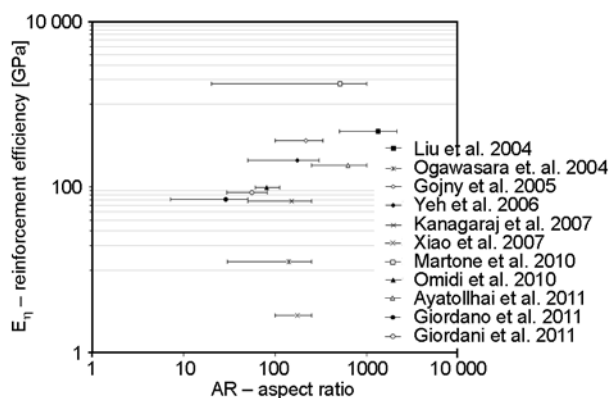


**Figure 1.** Available reinforcement efficiency data from 2004 to 2011 [25]

reports the reinforcement efficiencies of different experimental data found in the literature from 2004 to 2010. In the case of a thermally activated resin, the possible activation of the resin cure is a further issue, which may compromise the efficiency of the dispersion procedure, thus it needs to be taken into account. The final stage of mixing, either for solution dispersion or direct mixing, indeed, represents a critical phase due to the local raising of the temperature which may lead to the potential triggering of the cure reaction. An accurate control of the temperature and a suitable characterization of the rheological behaviour of the hosting matrix allow the identification of the most suitable temperature window preserving the unreacted state of the thermosetting matrix.

The aim of the present paper is to evaluate the effect of different mixing procedures on the resulting morphology of carbon nanotubes micrometric aggregates and, in turn, on the thermo-mechanical properties of the final epoxy matrix nanocomposite. The main novelty of this work is related to the explanation of the major efficiency of one technique (direct tip sonication) compared to the other ones, mainly investigating two principal features: potential application of this technique for scaled up process and achieved reinforcement efficiency of the nanofillers in the final nanocomposite. The adopted nanotube content corresponds to the statistical percolation threshold (0.1% wt/wt) according to previously published data for the same resin and nanotube type [25]. Statistical percolation threshold represent the minimum content at which the nanofiller give arise to a percolative network within the hosting matrix

thus effecting the overall macroscopic property of the final materials, i.e. percolation, ad example, represents the switching limit for these kind of system between electrical isolation and conductive behaviour. The dispersion of untreated MWCNTs into the chosen monocomponent epoxy has been performed by either using different solvents (*solvent aided dispersion*) and also by means of different agitation energy mechanisms (*direct mixing*). Preliminary thermal analysis and rheological tests were performed on the neat resin system in order to optimize the processing conditions in terms of the viscosity of the hosting system and ‘dwell’ period. The dispersion states of CNTs within the nanocomposite samples obtained by different dispersion routes have been characterised on the micron scale by optical microscopy (OM) and on the sub micrometric scale by Small Angle X-ray Scattering technique. Optical microscopy analysis of the nanocomposite morphology evidenced a very low density of MWCNTs micron sized aggregates in the case of direct mixed tip sonicated samples compared to nanocomposites obtained by solution aided dispersion technique and low energy mixing (magnetic and mechanical agitation). Small Angle X-ray Scattering analysis revealed that only in the case of tip sonicated samples carbon nanotubes are organised on a nanometric scale net. Such morphological feature corresponds on the macroscale to the highest increase of the bending elastic modulus and to the highest reduction of the thermal expansion coefficients among the manufactured nanocomposites.

## 2. Materials

The 7000 grade MWNTs carbon nanotubes, provided by Nanocyl S.A. (Belgium), were adopted. These nanotubes are grown by catalytic chemical vapor-deposition (CCVD) with a purity of 90%, a mean length of 10 micron and a mean diameter of 10 nm. These MWNTs were used directly without any purification. A commercial premixed epoxy-amine resin, denoted as RTM6, was used as matrix. This system, already degassed, fulfils the requirements of the aerospace industries in advanced liquid injection moulding processes and it was provided by Hexcel Composites (Duxford, UK). The solvent used in this work (acetone, ethanol and the sodium dodecyl sulphate) were acquired by Sigma Aldrich.



### 3. Preparation of MWCNT/epoxy samples

A fixed percentage content of MWCNT (0.1% w/w) has been used for the preparation of nanocomposites. The chosen percentage corresponds to the statistical percolation threshold considering the nominal aspect ratio of the nanotube ( $L/d \sim 1000$ ) as reported in [25]. In the case of solution dispersion, nanoparticles were dispersed in about 40 mL of solvent in a sealed beaker by an ultrasonic process (power has been set at 18 W), cooled with ice, for 30 minutes at room temperature. Then, the epoxy resin (40 gr) was added to the nanotubes solution, immersed in an oil bath at 80°C and sonicated for further 30 minutes until the removal of solvent residual content. The final solution was, then, poured in an aluminium mould, vacuum degassed for 30' at 90°C and then cured. For all nanocomposite samples, the cure schedule was 1.5 hour at 160°C and 2 hours at 180°C to assure the same conditions for comparison purpose.

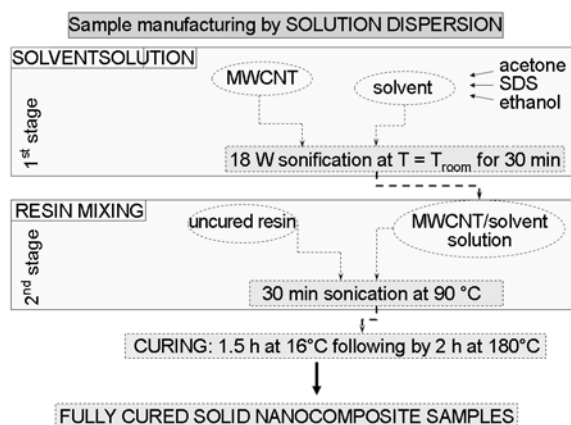


**Figure 2.** Flow chart of sample manufacturing by solution dispersion

The procedure, presented as direct mixing, was characterised by the following stages: pristine nanotube were added directly to the hosting epoxy matrix (40 gr) to perform the mixing stage at constant temperature (60, 90 and 120°C) for 60 minutes. In this case, the preliminary dispersion using the solvent was not carried out, but analogous conditions for the resin mixing, degassing and final polymerization were set. Magnetic agitation was performed by using FALC F60 (Falc Instruments, Italy) system equipped with a 20 W motor power and standard bar (15 mm length at 150 rpm); the mechanical stirring was performed by using a Heidolph RZR 2020 stirrer (50 W powered motor by Heidolph Instruments GmbH & Co. KG, Germany) equipped with a viscojet head and set at 1050 rpm. A Misonix S3000 sonicator (Misonix Inc., New York, USA) equipped with a titanium tapped horn with a 1/2" (12.7 mm) diameter tip was employed for the sonication stage. The process flow charts for each dispersion route are presented schematically in Figures 2 and 3.

### 4. Experimental methods

Optical microscopy analysis was carried out by using an Olympus system type BX51 (Olympus Italia S.r.l., Milan, Italy) in transmitted light configuration, to operate a preliminary classification of the nanotube dispersion. Differential Scanning Calorimetry (DSC) analysis has been performed by TA DSC instrument type 2920 (TA Instruments, Milan, Italy) with temperature ranging from -50 to 310°C at different heating rates and isothermal temperatures. The viscosity of the neat resin system was measured during cure, in both isothermal and

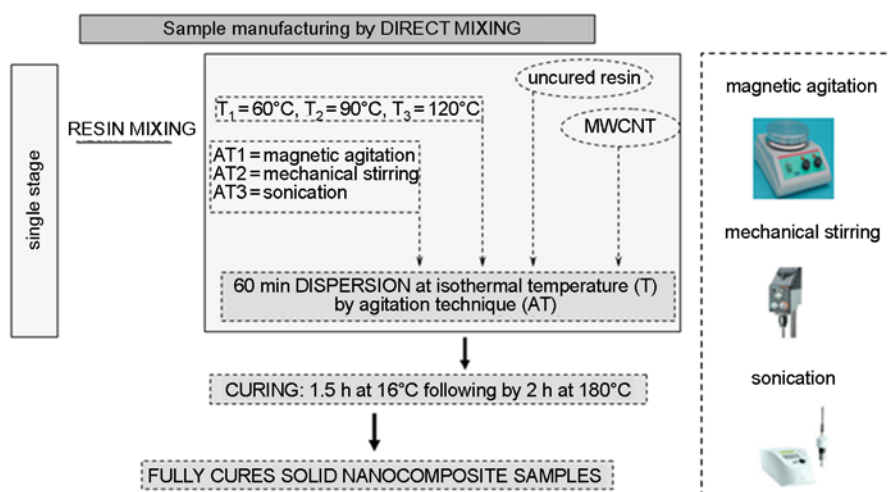


**Figure 3.** Flow chart of sample manufacturing by direct mixing at three different temperatures ( $T_1$ ,  $T_2$  and  $T_3$ ) by three agitation techniques (AT1, AT2, and AT3)

dynamic conditions by using an AntonPaar Instruments Rheometer (Anton Paar GmbH, Germany). The resin was drop onto a 40 mm parallel plate system with the bottom plate and the top plate (gap = 0.5 mm) oscillating at a fixed frequency of 0.5 Hz. Thermo-mechanical tests were performed by using a thermo-mechanical analyzer type TM60-WS from Shimadzu (M. Penati Strumenti srl, Milan, Italy), equipped with a macro-tip. The TMA scans were carried out on samples with rectangular cross section (3 mm × 3 mm) and maximum length of 15 mm according to the ISO 113598, with a 2°C/min temperature ramp. For each scan, the sample was placed in the cell and temperature equilibrated at 30°C for 10 minutes; linear dimension was monitored as the temperature arises up to 280°C. Nanocomposite specimens with nominal dimension of 60 × 10 × 2 mm were mechanically tested under three points bending mode by a TA 2980 Dynamic Mechanical Analyzer (TA Instruments, Milan, Italy), within the linear elastic region at given sub-glassy transition temperature (80°C) with an amplitude varying within the range from 20 to 60 μm. Wide and Small Angle X-ray Scattering (WAXS and SAXS) were performed with a SAXSess Instrument (Anton Paar GmbH, Germany), equipped with a 2D imaging plate detection system by using copper  $K_{\alpha}$  radiation  $\lambda = 0.1542$  nm. The X-Ray generator was operated at 40 kV and 50 mA and a line collimation was used to ensure high radiation intensity. All scattering data, dark current, background and incoherent scattering were subtracted, normalized for the primary beam intensity and finally desmeared. The scattering profile related to that of the neat epoxy resin was used as background for the composite scattering profiles.

## 5. Results and discussion

### 5.1. Chemo-rheological characterization of neat epoxy

Mono-component thermosetting polymers undergo a polymerization reaction, triggered by the temperature, which transforms the material from a liquid monomeric system to a fully reacted solid-like structure. During the curing, the viscosity of the system abruptly changes, reaching, theoretically, infinite values whenever the system crosses to the gelation point. Analysis of polymerization kinetics, therefore, is the most fundamental experimental data to be acquired before any mixing procedure could be attempted and validated.

A preliminary characterization of the neat epoxy system was performed to evaluate the chemo-rheological behaviour. The chemorheology at 5°C/min has been reported in Figure 4, as shows the minimum viscosity occurs around 120°C, which corresponds to the limiting processing temperature. Isothermal DMA characterization at 120°C, reported in Figure 4b, confirms that the system is very slowly reacting. According to previously reported data on the same epoxy system [25], a ‘dwell’ time of 60 min to mix the resin would not significantly affect the system viscosity.

### 5.2. Optical analysis of nanocomposites

Optical microscopy images have been qualitatively analyzed in terms of two main parameters: particles size and homogeneity of the sample, i.e. nanotubes clusters size and their spatial distribution through the sample. As a reference Figure 5 shows the micrographs of the nanocomposite samples obtained by hand mixing processed for 30 min at constant temperatures (60 and 90°C).

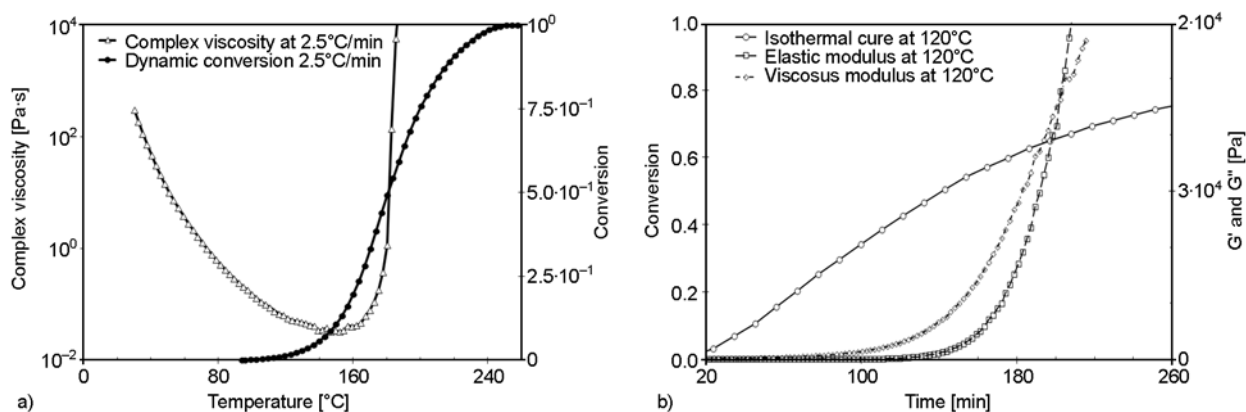
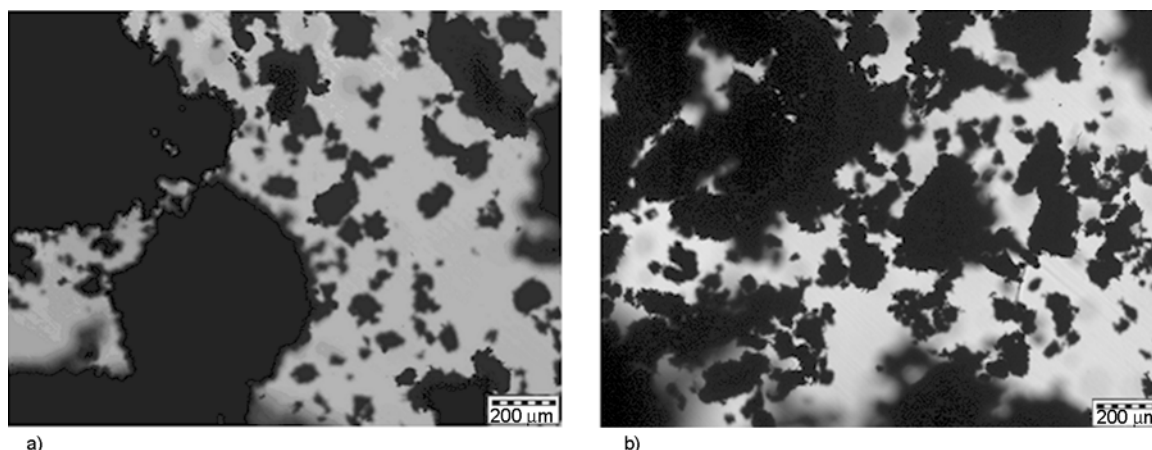


Figure 4. RTM6 chemorheology at 5°C/min a) and at 120°C isothermal temperature b)



**Figure 5.** Optical image of nanocomposite obtained by hand-dispersion at 60°C a) and 90°C b)

The nanotube agglomerates are preserved in their pristine shape appearing as unswollen. Hand mixing procedure led to a very poor level of pristine aggregates dispersion and homogenization with dense dark nanotube clusters surrounded by bright rich resin areas at both temperatures.

### 5.2.1. Solution dispersed samples

Different solvents were considered: acetone, ethanol and sodium dodecyl sulfate surfactant in water to improve the unwrapping and de-bundling the nanotubes agglomerates before adding them into the resin system.

The resin mixing with nanotubes/solvent solution was carried out by heating the oil bath up to 80°C and then holding this temperature for 30 minutes: higher temperatures would drastically reduce the available time for mixing before the solvents evaporation, while lower temperatures would induce a higher viscosity of the hosting system.

Table 1 reports details of all performed solution dispersion procedures. Optical micrographs are presented in Figure 6a, 6b and 6c for nanocomposite samples processed by solution dispersion and in Figure 6d for by sonication direct mixing at 60°C. Dispersion in acetone (Figure 6a) led to large CNT agglomerates characterised by indistinct bounds

with a denser central core. The average dimension of the agglomerations is of the order of 100 μm of the darker area. Optical images of samples dispersed in water/SDS (Figure 6b) show some residuals of solvent within a matrix of tiny spherical-shaped micro-agglomerates with an average diameter of few micrometers. In this case, the dispersion efficiency is quite promising although remarks remain either for the possibility to degas out completely the solvent content and for the chemical nature of the solvent during the dispersion solution. In the case of ethanol (Figure 6c), a coarse morphology is visible that is characterised by micro-sized nanotube agglomerates. Large semi-transparent areas can be noticed highlighting the sub optical resolution of dispersed nanotubes. A micrograph of a nanocomposite specimen obtained by tip sonication, without solvent, at 60°C is reported in Figure 6d. Very few nanotube aggregates are visible with sizes of few microns, very smaller than the pristine aggregates dimensions. The major part of the nanocomposite is semi-transparent and homogeneous, thus indicating that nanotubes are dispersed within the matrix forming CNT agglomerates, undetectable by the optical microscopy. In conclusion, optical microscopy demonstrate that by employing the tip sonication technique, without solvent, allows to obtain nano-

**Table 1.** Solution mixing procedure by using three different solvents

	Solvent/MWCNT solution	Resin mixing	Degassing	Curing
Figure 6a	30' at $T_{room}$ ultrasonication at 24 W in acetone	30' at 80°C, ultrasonication at 24 W	60 min at 90°C under vacuum	1.5 h at 160°C 2 h at 180°C
Figure 6b	30' at $T_{room}$ ultrasonication at 24 W in water/SDS	30' at 80°C, ultrasonication at 24 W	60 min at 90°C under vacuum	1.5 h at 160°C 2h at 180°C
Figure 6c	30' at $T_{room}$ ultrasonication at 24 W in ethanol	30' at 80°C ultrasonication at 24 W	60 min at 90°C under vacuum	1.5 h at 160°C 2 h at 180°C



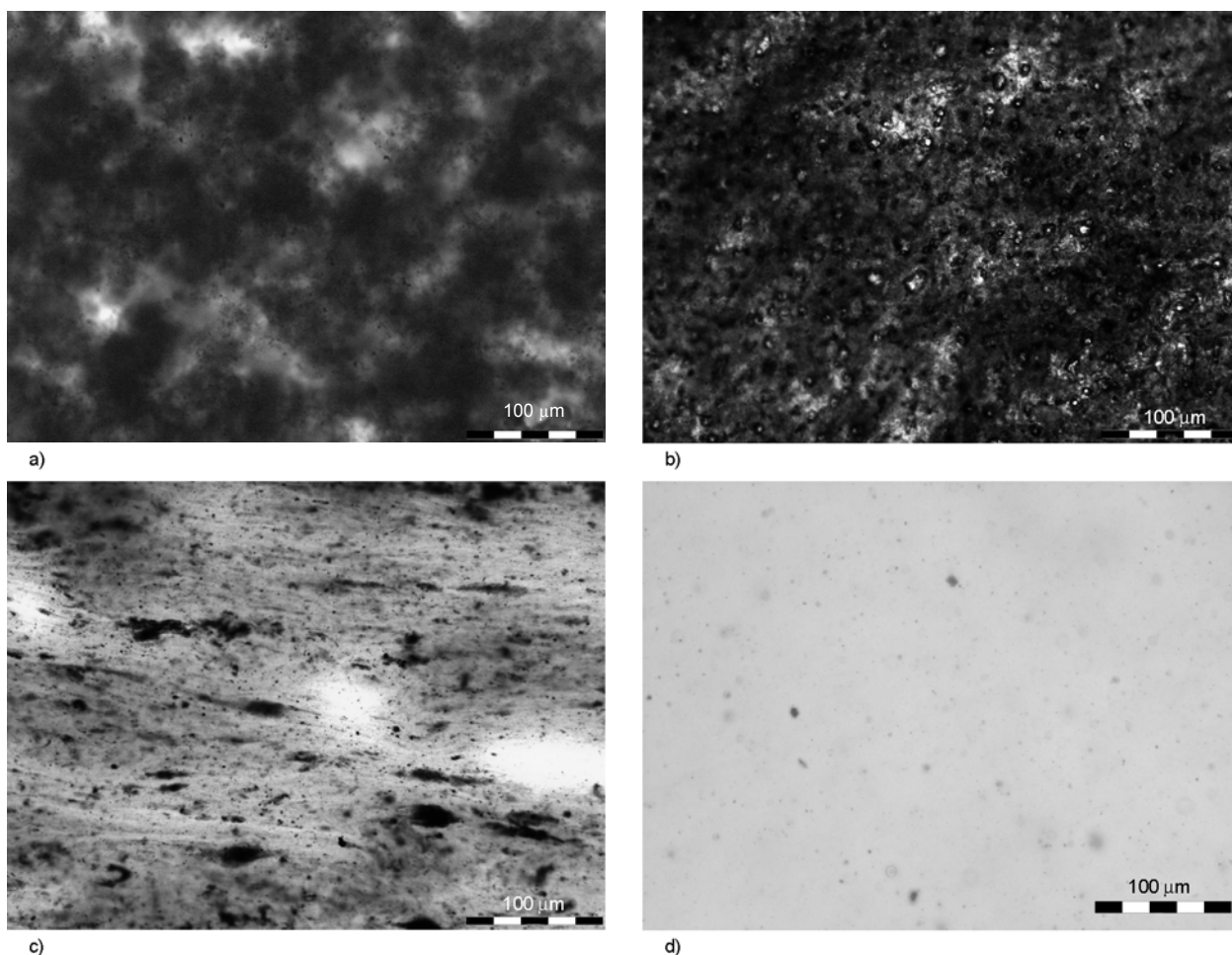


**Figure 6.** Optical microscopy for solution dispersed samples in (a) acetone (b) surfactant (c) ethanol and (d) direct mixed nanocomposite

composites with remarkable uniformity in CNT distribution and a sub-micron level of nanostructure texture.

### 5.2.2. Direct mixed samples

The direct mixing of MWCNT in RTM6 was performed at three different temperatures corresponding to three different levels of viscosity of the hosting system, 66, 190 and 692 mPa·s respectively 120, 90 and 60°C [25].

The containing beaker was immersed in an oil bath and opportunely temperature controlled until mixing temperature level was reached. Figure 7 reports a ‘mosaic’ of optical images for each used techniques. The disposition of the images in a 3 by 3 matrix shows the final composite morphology evolution with temperatures (60, 90 and 120°C) and with the employed mixing techniques (magnetic, mechanical and sonication). At all three considered temperatures, magnetic and mechanical stirring

lead optically highly non-homogeneous samples where nanotube agglomerates have dimensions lower than that of the hand mixed reference sample. In particular, mechanically mixed nanocomposites show lower sized micrometric nanotube clusters and a more homogeneous distribution of such clusters than the magnetically mixed samples. On the contrary nanocomposites obtained by sonication mixing are optically homogeneous with rare micron sized aggregates whose density decreases with the temperature. Nanotubes clusters are rarely optically visible at minimum viscosity temperature (120°C). For the first two mixing techniques, the temperature level does not much affect the final dispersion state.

### 5.3. X-ray analysis of nanocomposites obtained by direct mixing

The SAXS and WAXS profiles of epoxy matrix and both nanocomposites prepared by sonication, mechanical stirring and magnetical agitation at



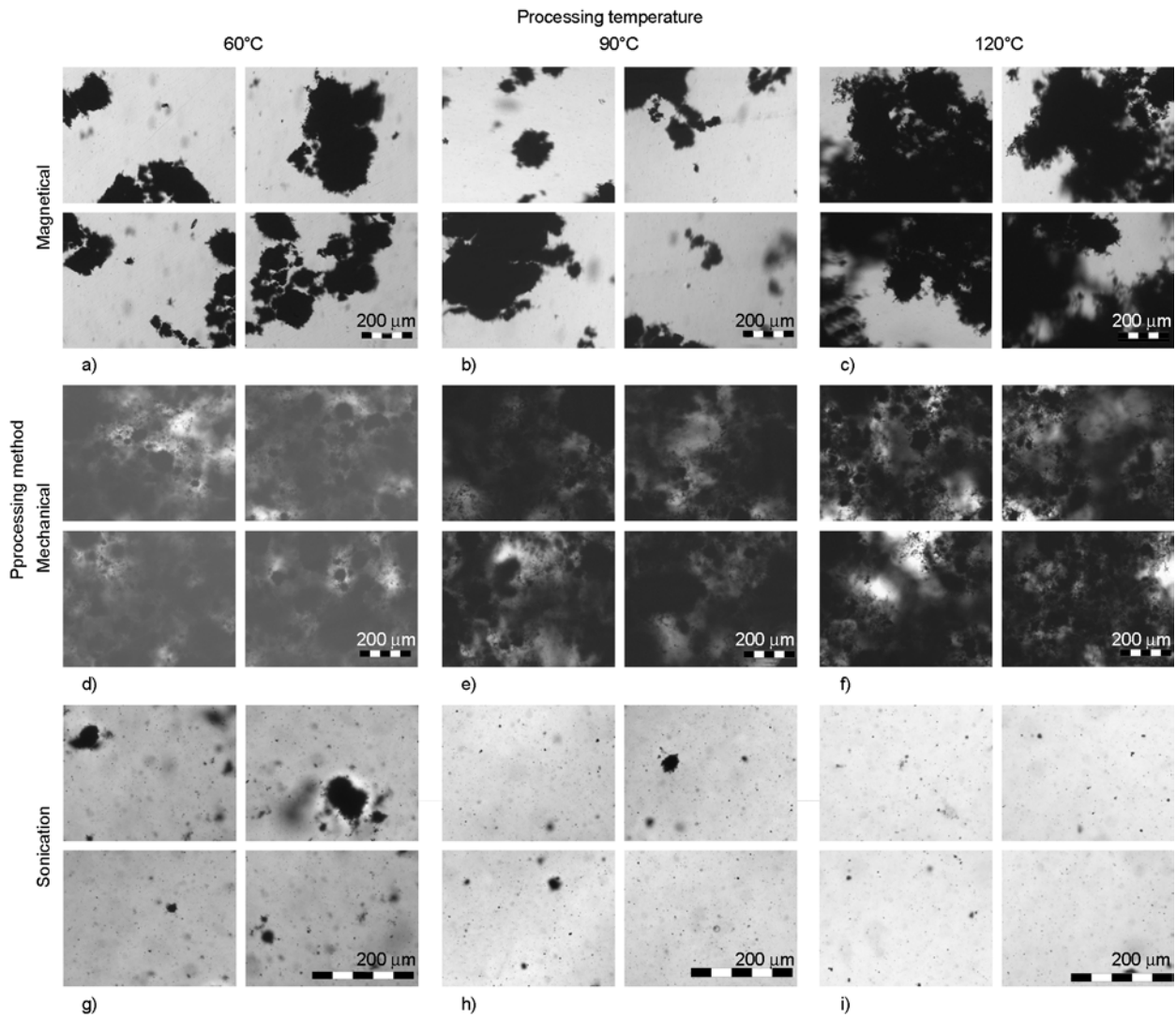


Figure 7. Optical images of nanocomposites prepared at various  $T$  by different mixing techniques

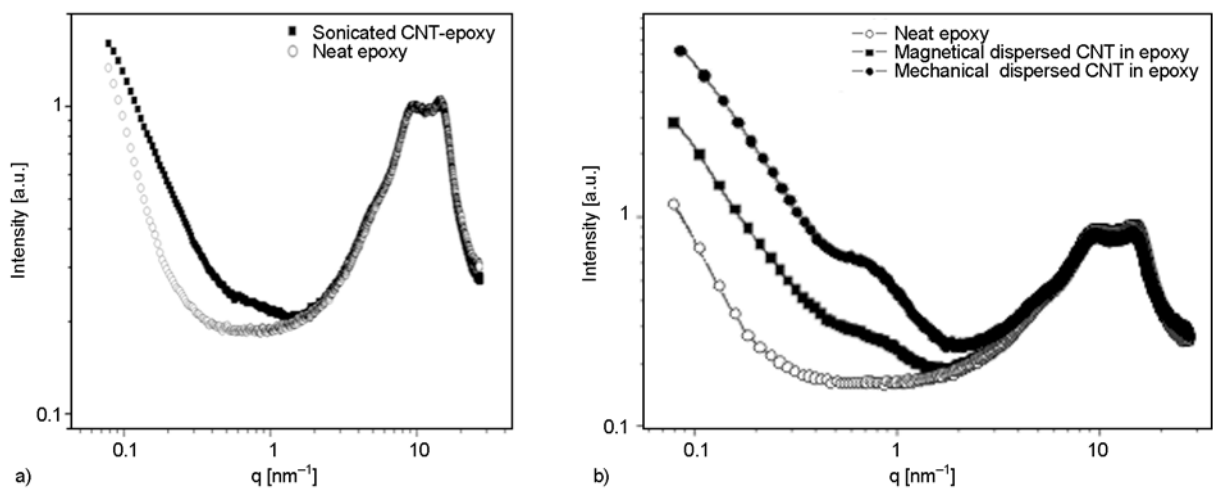
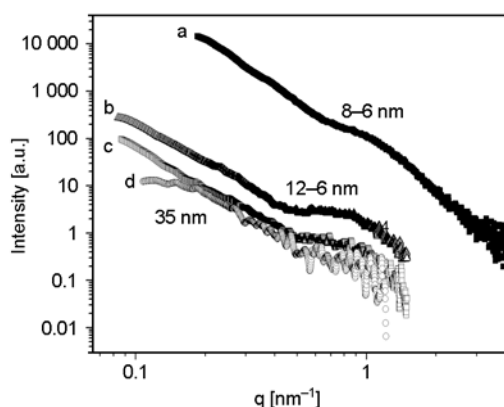


Figure 8. Scattering profiles for nanocomposites obtained by sonication vs neat system (a) and magnetical agitation, mechanical stirring vs neat system (b)



**Figure 9.** SAXS intensity Porod plots of the background a) and sample obtained by magnetic (b), mechanical (c) and sonication (d) dispersion methods

120°C are shown in Figure 8. It is worth noting that regardless the preparation procedure the nanocomposites display the typical halo featuring with the neat epoxy resin centred around 10 nm<sup>-1</sup>.

Since the presence of CNTs does not affect the intimate structure of epoxy matrix, the neat epoxy scattering profile can be used as background subtracted to the composites profiles, thus isolating the CNT contribution. The scattering profile related to the neat epoxy resin was superimposed. In the inset an enlargement at low  $q$  values is reported. The SAXS profiles of CNTs within composites prepared at 120°C by using the three above mentioned direct mixing methods are shown in Figure 9, as log-log Porod plot of the scattering intensity,  $I$  versus  $q$ .

The plot of CNT powders used to prepare the composites is also reported for comparison in Figure 9. The scattering profile of CNT powders is shown as comparison (a). The CNTs powders profile showed a knee-scattering feature corresponding to a size of

about 6–8 nm, assessed as  $d = 2\pi/q$  [26, 27]. Since the mean diameter of CNT was about 10 nm, it could be reasonably thought that this dimension corresponds to the cross-section of CNT when they were analysed vs. air, i.e. in powder state. The same characteristic feature is also highlighted in the scattering profiles of composites prepared by mechanical and magnetic dispersion mode, confirming the poor dispersion of CNTs bundles in the epoxy matrix as appeared by microscope analyses. On the other hand, in the scattering profile of the sonicated composite, it is worth noting a strong reduction of above mentioned knee-feature, together with an additional knee-scattering feature at about 0.18 nm<sup>-1</sup>, corresponding to a dimension of about 35 nm. As previously reported [24] this size could be associated to a bundle consisting of about 3 nanotubes side-by-side interacting.

#### 5.4. Mechanical and dilatometric analysis of nanocomposites obtained by direct mixing

Dynamic mechanical tests were performed on samples manufactured by direct mixing at 120°C to evaluate the bending modulus. Figure 10a reports the strain sweep scans of the three nanocomposite samples processed at the same isothermal temperature (120°C) by means of the different energy shear-based techniques. Figure 10b reports the flexural modulus and 40  $\mu$ m amplitude. Flexural modulus of the neat system was found equal to 2998±96.5 MPa, according to previously reported data, whilst sonicated samples revealed the maximum modulus enhancement of about 10% (3285±338.1 MPa). Flexural modulus of nanocomposite samples obtained by magnetic or mechanical mixing results slightly

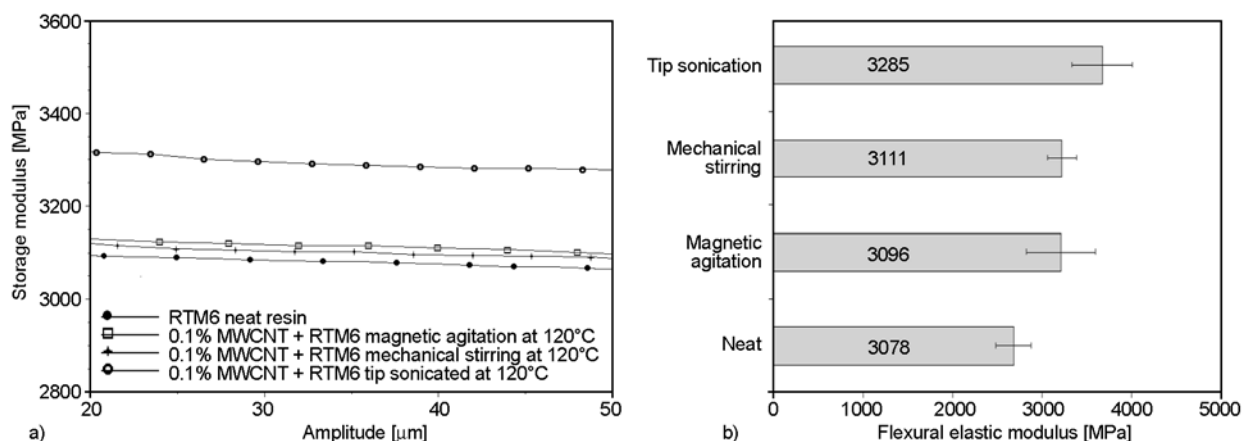


**Figure 10.** DMA tests performed on nanocomposite samples processed at 120°C by using three mixing techniques a) and flexural moduli for nanocomposite samples processed by direct mixing at 120°C b)

higher compared to the neat resin and respectively, equal to  $3096 \pm 384.6$  and  $3111 \pm 164.2$  MPa.

Morphology of the reinforcing phase, i.e. nanotubes clusters size and spatial distribution through the sample, strongly affects the flexural modulus of the nanocomposite. In particular, the presence of micron sized clusters of nanotubes has a detrimental effect of the flexural modulus. Reduction of clusters size leads to an improvement of the nanocomposite modulus.

Sonication will act in the direction of disaggregate the nanotube bundles giving rise to a sub-microlevel texture due to the cavitation effect induced by ultrasound waves. Moreover, the cooperative motion due to the density gradient induced by the cavitation under the sonicator tip leads to a uniform spatial distribution of the nanofiller within the hosting system. For these reasons, it seems reasonable to assume that a better impregnation of the carbon nanotube will amplify the effect of stress transfer under loaded condition by the overall final nanocomposite. On the other hand, large microsized clusters formed during the mechanical or magnetic agitation can present a different content of resin thus lowering the stress transfer efficiency with the matrix. It can be argued that microsized formation and therefore contractedness between of nanofiller will inevitably reduce the reinforcement efficiency. In fact, while for electrical behaviour contacts between tubes improve electron transport, their occurrence will inevitably reduce the nominal length of the nanofiller (CNT length is further reduced by the sonication effect, as reported in the literature) thus strongly affecting the stress transfer with the matrix. The positive effect associated with sonication technique could be reviewed mainly in

two fundamental features: firstly, sonication and high shear induced by the cavitation strongly disaggregate the microsized structure of pristine nanotubes thus enhancing the available area for stress transfer, whereas the CNT length reduction will act in the opposite direction. Concurrently also sample homogeneity (i.e. the spatial distribution of the nanotube filler within the matrix) plays a role in determining the nanocomposite mechanical modulus. Neat epoxy and nanocomposite samples were also tested by thermo-mechanical analyser (TMA) to evaluate the coefficient of thermal expansions (CTE), in both rubber and glassy regions [27]. Figure 11 shows the linear expansion dilatometric curves for the nanocomposite samples processed by direct mixing at isothermal temperature of  $120^\circ\text{C}$  along with the corresponding curve of neat epoxy system.

In the glassy region, all nanocomposites presented lower thermal dilatations than neat epoxy. Maximum reduction of about 6% has been found in the case of sonication produced samples. More accentu-

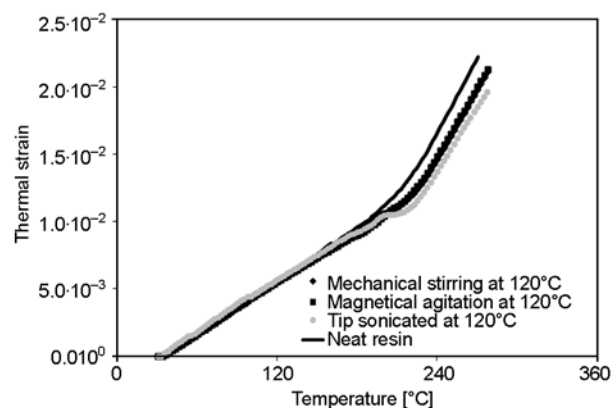


Figure 11. TMA scans of direct mixed nanocomposite samples under and above glass transition temperature

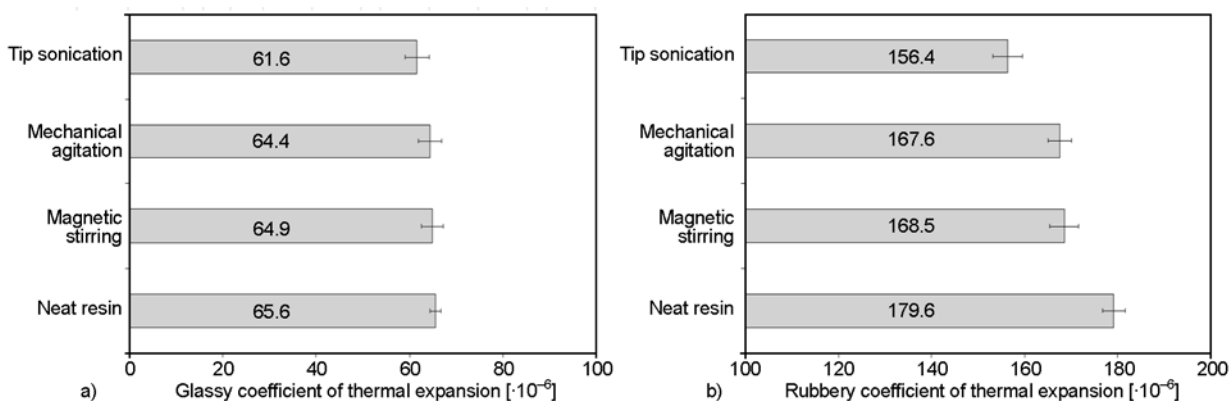


Figure 12. Bar diagram of coefficient of thermal expansion for the nanocomposite samples processed by direct mixing procedure a) rubbery and b) glassy values

ated effects have been observed in the rubbery coefficient of thermal expansion.

The values, in fact, result much lower for the nanocomposite processed by tip-sonication with an average variation of around 13%; while a change of about 5% is measured for the nanocomposite processed by magnetic and mechanical technique (Figure 12a and b).

## 6. Conclusions

Different dispersion procedures have been considered to disperse multi-walled carbon nanotubes within a commercial epoxy resin used as matrix for advanced composites namely solvent aided dispersion and direct mixing. The effect of selected solvents and mixing techniques on the final nanocomposite morphology has been qualitatively investigated with reference to the presence of micron sized nanotubes aggregates by optical microscopy. It was found that preliminary stage using solvent aided dispersion can be suitably avoided, simplifying the scaling-up of the dispersion procedure at industrial level. The final nanocomposite morphology by direct sonication leads to a submicron and more uniform texture compared to the others. This was mainly attributed to the different mechanisms involved into the dispersion process by using high-energy ultra-sonication: a) tip cavitation which induces pristine nanotube bundles disgregation and b) the overall convective motions of the resin due to the density gradient under the sonication tip which homogenises the spatial distribution of the dispersed nanofiller within the hosting matrix.

Small Angle X-ray diffraction analysis revealed that the sonication aided mixing produces nanocomposites with nanometric sized structures (bundles of 35 nm of diameter at 120°C) and a very low density of carbon nanotubes aggregates. As expected, the bending modulus of the nanocomposite increases with the reduction of the density of micrometric carbon nanotubes aggregates due to the higher reinforcement efficiency achieved in the final nanocomposite. In addition, the rubbery thermal expansion coefficient of the sonication produced sample showed also a significant reduction of 15% in respect to the matrix value where samples produced by lower energy manufacturing routes (magnetic and mechanical stirring) showed a modest reduction of 5%.

## References

- [1] Baughman R. H., Zakhidov A. A., de Heer W. A.: Carbon nanotubes – The route toward applications. *Science*, **297**, 787–792 (2002). DOI: [10.1126/science.1060928](https://doi.org/10.1126/science.1060928)
- [2] Coleman J. N., Khan U., Blau W. J., Gun'ko Y. K.: Small but strong: A review of the mechanical properties of carbon nanotube–polymer composites. *Carbon*, **44**, 1624–1652 (2006). DOI: [10.1016/j.carbon.2006.02.038](https://doi.org/10.1016/j.carbon.2006.02.038)
- [3] Xie X. L., Mai Y. W., Zhou X. P.: Dispersion and alignment of carbon nanotubes in polymer matrix: A review. *Materials Science and Engineering: R: Reports*, **49**, 89–112 (2005). DOI: [10.1016/j.mser.2005.04.002](https://doi.org/10.1016/j.mser.2005.04.002)
- [4] Ajayan P. M., Schadler L. S., Giannaris C., Rubio A.: Single-walled carbon nanotube–polymer composites: Strength and weakness. *Advanced Materials*, **12**, 750–753 (2000). DOI: [10.1002/\(SICI\)1521-4095\(200005\)12:10<750::AID-ADMA750>3.3.CO;2-Y](https://doi.org/10.1002/(SICI)1521-4095(200005)12:10<750::AID-ADMA750>3.3.CO;2-Y)
- [5] Schadler L. S., Giannaris S. C., Ajayan P. M.: Load transfer in carbon nanotube epoxy composites. *Applied Physics Letters*, **73**, 3842–3844 (1993). DOI: [10.1063/1.122911](https://doi.org/10.1063/1.122911)
- [6] Tibbetts G. G., Beetz C. P.: Mechanical properties of vapour-grown carbon fiber. *Journal of Physics D: Applied Physics*, **20**, 292–297 (1987). DOI: [10.1088/0022-3727/20/3/008](https://doi.org/10.1088/0022-3727/20/3/008)
- [7] Martone A., Formicola C., Giordano M., Zarrelli M.: Reinforcement efficiency of multi-walled carbon nanotube/epoxy nano composites. *Composites Science and Technology*, **70**, 1154–1160 (2010). DOI: [10.1016/j.compscitech.2010.03.001](https://doi.org/10.1016/j.compscitech.2010.03.001)
- [8] Dyke C. A., Tour J. M.: Covalent functionalization of single-walled carbon nanotubes for materials applications. *Journal of Physical Chemistry A*, **108**, 11151–11159 (2004). DOI: [10.1021/jp046274g](https://doi.org/10.1021/jp046274g)
- [9] Qian D., Dickey E. C., Andrews R., Rantell T.: Load transfer and deformation mechanisms in carbon nanotube-polystyrene composites. *Applied Physics Letters*, **76**, 2868–2871 (2000). DOI: [10.1063/1.126500](https://doi.org/10.1063/1.126500)
- [10] Park C., Ounaies Z., Watson K. A., Crooks R. E., Smith J., Lowther S. E., Connell J. W., Siochi E. J., Harrison J. S., St. Clair T. L.: Dispersion of single wall carbon nanotubes by in situ polymerization under sonication. *Chemical Physics Letters*, **364**, 303–308 (2002). DOI: [10.1016/S0009-2614\(02\)01326-X](https://doi.org/10.1016/S0009-2614(02)01326-X)
- [11] Ham H. T., Choi Y. S., Chung I. J.: An explanation of dispersion states of single-walled carbon nanotubes in solvents and aqueous surfactant solutions using solubility parameters. *Journal of Colloid and Interface Science*, **286**, 216–223 (2005). DOI: [10.1016/j.jcis.2005.01.002](https://doi.org/10.1016/j.jcis.2005.01.002)



- [12] Salvetat J-P., Briggs G. A. D., Bonard J-M., Bacsá R. R., Kulik A. J., Stöckli T., Burnham N. A., Forró L.: Elastic and shear moduli of single-walled carbon nanotube ropes. *Physical Review Letters*, **82**, 944–947 (1999).  
DOI: [10.1103/PhysRevLett.82.944](https://doi.org/10.1103/PhysRevLett.82.944)
- [13] Choi E. S., Brooks J. S., Eaton D. L., Al-Haik M. S., Hussaini M. Y., Garmestani H., Li D., Dahmen K.: Enhancement of thermal and electrical properties of carbon nanotube polymer composites by magnetic field processing. *Journal of Applied Physics*, **94**, 6034–6039 (2003).  
DOI: [10.1063/1.1616638](https://doi.org/10.1063/1.1616638)
- [14] Sandler J., Shaffer M. S. P., Prasse T., Bauhofer W., Schulte K., Windle A. H.: Development of a dispersion process for carbon nanotubes in an epoxy matrix and the resulting electrical properties. *Polymer*, **40**, 5967–5971 (1999).  
DOI: [10.1016/S0032-3861\(99\)00166-4](https://doi.org/10.1016/S0032-3861(99)00166-4)
- [15] Sandler J. K. W., Kirk J. E., Kinloch I. A., Shaffer M. S. P., Windle A. H.: Ultra-low electrical percolation threshold in carbon-nanotube-epoxy composites. *Polymer*, **44**, 5893–5899 (2003).  
DOI: [10.1016/S0032-3861\(03\)00539-1](https://doi.org/10.1016/S0032-3861(03)00539-1)
- [16] Lau K-T., Lu M., Lam C-K., Cheung H-Y., Sheng F-L., Li H-L.: Thermal and mechanical properties of single-walled carbon nanotube bundle-reinforced epoxy nanocomposites: The role of solvent for nanotube dispersion. *Composites Science and Technology*, **65**, 719–725 (2005).  
DOI: [10.1016/j.compscitech.2004.10.005](https://doi.org/10.1016/j.compscitech.2004.10.005)
- [17] Li J., Tong L., Fang Z., Gu A., Xu Z.: Thermal degradation behavior of multi-walled carbon nanotubes/polyamide 6 composites. *Polymer Degradation and Stability*, **91**, 2046–2052 (2006).  
DOI: [10.1016/j.polymdegradstab.2006.02.001](https://doi.org/10.1016/j.polymdegradstab.2006.02.001)
- [18] Wang Z., Liang Z., Wang B., Zhang C., Kramer L.: Processing and property investigation of single-walled carbon nanotube (SWNT) buckypaper/epoxy resin matrix nanocomposites. *Composites Part A: Applied Science and Manufacturing*, **35**, 1225–1232 (2004).  
DOI: [10.1016/j.compositesa.2003.09.029](https://doi.org/10.1016/j.compositesa.2003.09.029)
- [19] Wu J., Chung D. D. L.: Calorimetric study of the effect of carbon fillers on the curing of epoxy. *Carbon*, **42**, 3039–3042 (2004).  
DOI: [10.1016/j.carbon.2004.07.010](https://doi.org/10.1016/j.carbon.2004.07.010)
- [20] Xu X., Thwe M. M., Shearwood C., Liao K.: Mechanical properties and interfacial characteristics of carbon-nanotube-reinforced epoxy thin films. *Applied Physics Letters*, **81**, 2833–2835 (2002).  
DOI: [10.1063/1.1511532](https://doi.org/10.1063/1.1511532)
- [21] Lau K-T., Lu M., Lam C-K., Cheung H-Y., Sheng F-L., Li H-L.: Thermal and mechanical properties of single-walled carbon nanotube bundle-reinforced epoxy nanocomposites: The role of solvent for nanotube dispersion. *Composites Science and Technology*, **65**, 719–725 (2005).  
DOI: [10.1016/j.compscitech.2004.10.005](https://doi.org/10.1016/j.compscitech.2004.10.005)
- [22] Vaisman L., Wagner H. D., Marom G.: The role of surfactants in dispersion of carbon nanotubes. *Advances in Colloid and Interface Science*, **128–130**, 37–46 (2005).  
DOI: [10.1016/j.cis.2006.11.007](https://doi.org/10.1016/j.cis.2006.11.007)
- [23] Faiella G., Piscitelli F., Lavorgna M., Antonucci V., Giordano M.: Tuning the insulator to conductor transition in a multi walled carbon nanotubes/epoxy matrix composite at sub statistical percolation threshold. *Applied Physics Letters*, **95**, 153106/1–153106/3 (2009).  
DOI: [10.1063/1.3242017](https://doi.org/10.1063/1.3242017)
- [24] Martone A., Faiella G., Antonucci V., Giordano M., Zarrelli M.: Investigation of the effective reinforcement modulus of carbon nanotubes in an epoxy matrix. in ‘Carbon nanotubes – From research to applications’ (ed.: Bianco S.) InTech Publisher, Rijeka, 269–294 (2011).
- [25] Martone A., Faiella G., Antonucci V., Giordano M., Zarrelli M.: The effect of the aspect ratio of carbon nanotubes on their effective reinforcement modulus in an epoxy matrix. *Composites Science and Technology*, **71**, 1117–1123 (2011).  
DOI: [10.1016/j.compscitech.2011.04.002](https://doi.org/10.1016/j.compscitech.2011.04.002)
- [26] Hernández J. J., García-Gutiérrez M. C., Nogales A., Rueda D. R., Ezquerro T. A.: Small-angle X-ray scattering of single-wall carbon nanotubes dispersed in molten poly(ethylene terephthalate). *Composites Science and Technology*, **66**, 2629–2632 (2006).  
DOI: [10.1016/j.compscitech.2006.05.008](https://doi.org/10.1016/j.compscitech.2006.05.008)
- [27] Pizzutto C. E., Suave J., Bertholdi J., Pezzin S. H., Coelho L. A. F., Amico S. C.: Mechanical and dilatometric properties of carboxylated SWCNT/epoxy composites: Effects of the dispersion in the resin and in the hardener. *Journal of Reinforced Plastics and Composites*, **29**, 524–530 (2010).  
DOI: [10.1177/0731684408099924](https://doi.org/10.1177/0731684408099924)

# Polystyrene/nano-SiO<sub>2</sub> composite microspheres fabricated by Pickering emulsion polymerization: Preparation, mechanisms and thermal properties

W. H. Zhang, X. D. Fan, W. Tian\*, W. W. Fan

Department of Applied Chemistry, School of Science, Northwestern Polytechnical University, 710072 Xi'an, People's Republic of China

Received 4 November 2011; accepted in revised form 19 January 2012

**Abstract.** We report the preparation, mechanisms and thermal properties of core-shell structured polymer/inorganic nanoparticle composite microspheres prepared by Pickering emulsion polymerization. Stable Pickering emulsion was firstly fabricated by using surface-modified nano-SiO<sub>2</sub> particles as stabilizer. And then, two kinds of polystyrene/nano-SiO<sub>2</sub> (PS/SiO<sub>2</sub>) composite microspheres with different sizes and morphologies were synthesized using hydrophobic azobisisobutyronitrile (AIBN) and hydrophilic ammonium persulfate (APS) as initiator, respectively. The possible mechanisms of Pickering emulsion polymerization initiated by different initiators were proposed according to the results of transmission electron microscope (TEM) and scanning electron microscope (SEM). The chemical structure and molecular weight of the composite microspheres were characterized by Fourier transform infrared spectroscopy (FTIR), X-ray diffractometer (XRD) and gel permeation chromatography coupled with a multi-angle laser light scattering photometer (GPC-MALLS). Thermogravimetric analysis (TGA) and differential scanning calorimeter (DSC) were used to comparatively analyze the thermal properties of nanocomposites and corresponding pure polymer. The results indicated that the decomposition temperature and glass transition temperature ( $T_g$ ) of nanocomposites were elevated to a certain degree due to the existence of nano-SiO<sub>2</sub>.

**Keywords:** nanocomposites, Pickering emulsion polymerization, mechanism, thermal properties

## 1. Introduction

Organic/inorganic nanocomposite microspheres have attracted increasing attention because of their unique properties emerging from the combination of the advantageous properties of inorganic nanoparticles and polymers. In comparison with the pure polymers or their traditional composites, the resultant nanocomposites exhibit many markedly improved properties such as increased modulus and strength, enhanced barrier properties, improved heat resistance and decreased flammability [1, 2]. Therefore, the nanocomposite microspheres have been widely used in the various fields such as safety, protective

garments, aerospace, electronics and optical devices [3, 4].

Generally, organic/inorganic nanocomposite microspheres can be prepared by many methods such as miniemulsion polymerization [5], soap-free emulsion polymerization [6], seeded emulsion polymerization [7] and dispersion polymerization [8], etc. The composite microspheres with inorganic core and polymer shell are mostly fabricated by these conventional methods. In recent years, self-assembly of ultrafine solid particles at the oil/water interface to stabilize so-called Pickering emulsion has been well documented and offers a straightforward

\*Corresponding author, e-mail: [happytw\\_3000@163.com](mailto:happytw_3000@163.com)  
© BME-PT

pathway for the production of organic/inorganic nanocomposite microspheres [9–12]. In Pickering emulsions, solid nanoparticles possessing intermediate wettability are added as both a component and a stabilizer during the polymerization process. There is no need to use conventional low-molecular-weight surfactants. There are also no by-products produced in the process, and no unwanted contaminants are left in the polymer [13]. In contrast to the often reported core-shell structure in which inorganic particles serve as the core and polymer serves as the shell, the nanocomposite microspheres fabricated by Pickering emulsion polymerization has a polymer core and the nanoparticles shell. Such materials provide a new class of supramolecular building blocks and are likely to exhibit unusual, possibly unique properties [14].

So far, the preparation and forming principle of Pickering emulsion have been well documented by Binks and coworkers [15–17], Midmore [18], and Bon and coworkers [19, 20]. Moreover, a series of nanocomposite microspheres have been prepared. Bon and Colver [21] reported the fabrication of a variety of armored latex by Pickering miniemulsion polymerizations using Laponite clay discs as stabilizer. Zaragoza-Contreras *et al.* [22] described the synthesis of carbon black/polystyrene conductive nanocomposite by Pickering suspension polymerization technique. Zhang *et al.* [23] have prepared Poly(N-isopropylacrylamide)/poly(methyl methacrylate)/silica hybrid capsules via inverse Pickering emulsion polymerization. However, the suggested mechanisms of Pickering emulsion polymerization in these papers are preliminary. And, most of the mechanisms research only focused on the case in which monomer and initiator were in the same phase. Additionally, the thermal properties of the resultant composites have seldom been systematic studied. However, the evaluation of the thermal stability and degradation behaviors of composites is an effective method to verify synergistic effects between polymer and inorganic particles, and useful to modify the composites for further application. Herein, two kinds of polystyrene/nano-SiO<sub>2</sub> composite microspheres with core-shell structure were prepared by Pickering emulsion polymerization. The possible mechanisms of Pickering emulsion polymerization initiated by hydrophobic azobisisobutyronitrile (AIBN) and hydrophilic ammo-

nium persulfate (APS) were discussed, respectively. The chemical structure and molecular weight of the product were characterized by FTIR, XRD and GPC-MALLS. At last, the influences of nanoparticles on the decomposition temperature and on the glass transition temperature ( $T_g$ ) of the resultant nanocomposite microspheres were systematically studied by thermogravimetric analysis (TGA) and differential scanning calorimetry (DSC).

## 2. Materials and methods

### 2.1. Materials

Dodecyltrimethoxysilane (WD-10) was obtained from Wuhan University Silicone New Material Co. Ltd (China). Styrene, azobisisobutyronitrile (AIBN) and ammonium persulfate (APS) were purchased from Tianjin Chemical Reagent Corporation (China). Tetraethylorthosilicate (TEOS), methanol, ammonium hydroxide (NH<sub>3</sub> 25%) were all analytical reactant grade and were supplied by Xi'an Chemical Reagent Co. Ltd (China). Styrene was distilled under reduced pressure before use and the other reagents were used as received. Deionized water was used throughout the experiments.

### 2.2. Characterization

Laser particle size analyzer (Malvern Zetasizer Nano ZS3600) was used to obtain the average particle size and particle size distribution of the nano-SiO<sub>2</sub> before and after modification. The morphology and size of the composite microspheres were observed by TEM (JEM-3010, Japan) and SEM (JSM6380, Japan). FTIR spectra were obtained by a FTIR spectrometer (Nicolet is10, USA) in range of 4000–400 cm<sup>-1</sup>. The samples were prepared into KBr pellets. X-ray diffraction (XRD) analysis was carried out with a Rigaku D/max-IIIc X-ray diffractometer with graphite monochromatized Cu-K $\alpha$  radiation ( $\lambda = 0.1548$  nm), the scan rate of 4°/min allowed to record the patterns in the  $2\theta$  range of 10–60°. The molecular weight and molecular weight distribution of the resultant polystyrene (PS) after eliminating SiO<sub>2</sub> nanoparticles was measured by gel permeation chromatography coupled with a multi angle laser light scattering photometer (GPC-MALLS) with a Wyatt GPC instrument. The column temperature was 40°C and the chromatographic grade dimethylformamide (DMF) was used as solvent. TGA was performed with a thermal

analysis instrument (TA Q50, USA) under nitrogen gas. The flow rate was 40 cm<sup>3</sup>/min and heating rate was 20°C/min. DSC (TA 2910, USA) was used to obtain the glass transition temperature ( $T_g$ ) of the products. The sample was first heated from 20 to 140°C with the scan rate of 20°C/min to remove thermal history.  $T_g$  is obtained by the second scanning from 20 to 140°C with the scan rate of 10°C/min.

### 2.3. Preparation and modification of silica nanoparticles

Silica nanoparticles were prepared via an improved Stöber method as follows [24]. To a round-bottom flask of 500 mL capacity were added 10 mL TEOS and 100 mL methanol under sonication. After 5 min, 20 mL of 25% ammonium hydroxide and 200 mL of methanol were added into the reaction mixture synchronously. Sonication was continued for a further 3 h to get a bluish translucent nano-SiO<sub>2</sub> colloidal solution. Circulating water was used to maintain the temperature of the sonication bath below 30°C.

The hydrophilic nano-SiO<sub>2</sub> was hydrophobically modified with dodecyltrimethoxysilane (WD-10) to attach long chain alkyl on the surface and reduce the surface density of silanol groups. WD-10 (0.1 mL) was added to 100 mL of silica dispersion and the solution was refluxed at 80°C for 3 h. Before adding WD-10, the pH of the colloidal solution was adjusted to pH 7 with acetic acid under stirring conditions. After reaction, the reaction mixture was centrifuged (15 000 rpm, 15 min) and washed by repeating redispersion in anhydrous ethanol at least three times. The modified silica particles were collected and dried under vacuum at 40°C for 8 h.

### 2.4. Preparation of PS/nano-SiO<sub>2</sub> composite microspheres by Pickering emulsion polymerization

A representative preparation procedure was as follows. A given mass of modified nano-SiO<sub>2</sub> particles were ultrasonically dispersed into water for 15 min. For AIBN used as initiator, AIBN was dissolved in

styrene to form oil phase, and subsequently the oil phase was mixed with the nano-SiO<sub>2</sub> dispersions. A stable Pickering emulsion was generated using KUSON 500 W digital sonifier for 2 min at 80% amplitude. The resulted Pickering emulsion was poured into a 100 mL three-neck flask equipped with a nitrogen inlet and a reflux condenser. The emulsion was agitated mildly (200 rpm) and polymerized under nitrogen atmosphere at 75°C for 12 h. The precipitates after filtration were washed with water and ethanol for three times, respectively. The collected product was dried at 30°C under vacuum for 4 h and referred to as composite microspheres I. As for APS system, APS was dissolved in modified nano-SiO<sub>2</sub> dispersions to form water phase. Then styrene monomer was added into water phase and Pickering emulsion was generated by ultrasonic emulsification. The subsequent procedures were the same as AIBN system. The product was referred to as composite microspheres II. The compositions of recipe to prepare two kinds of polystyrene/nano-SiO<sub>2</sub> composite microspheres were listed in Table 1.

## 3. Results and discussion

### 3.1. Formation of Pickering emulsions stabilized by surface-modified nano-SiO<sub>2</sub>

The sizes of nano-SiO<sub>2</sub> before and after modification using the laser particle size analyzer are shown in Figure 1. Obviously, the particle size and poly-

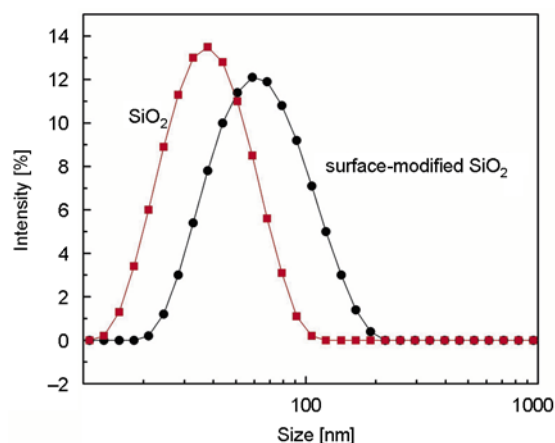


**Figure 1.** Results of particle size and particle size distribution of nano-SiO<sub>2</sub> and surface-modified nano-SiO<sub>2</sub>

**Table 1.** Recipe to prepare polystyrene/nano-SiO<sub>2</sub> composite microspheres

Sample	Styrene monomer [mL]	Initiator	Initiator dosage [mg]	Surface-modified SiO <sub>2</sub> [g]	Pure water [mL]
I	2	AIBN	12	0.2	20
II	2	APS	12	0.2	20



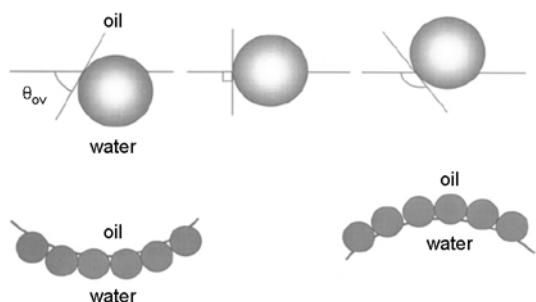


**Figure 2.** Schematic diagram of the relationship between three-phase contact angle and emulsion types [26]

dispersity index of modified nano-SiO<sub>2</sub> (z-average: 57.7 nm, PDI: 0.153) are larger than that of original nano-SiO<sub>2</sub> (z-average: 34.9 nm, PDI: 0.128). It may be ascribed to the agglomeration of nano-SiO<sub>2</sub> caused by some operating procedures such as pH adjusting, heating reflux reaction and high speed centrifugation in the entire process of surface modification [25].

The research results of Binks and Lumsdon [15] and Aveyard *et al.* [26] indicated that the type and stability of Pickering emulsion were determined mostly by the wettability (often expressed as a contact angle  $\theta$  at the three-phase boundary) of ultra-fine particles. As is shown in Figure 2, for

hydrophilic particles,  $\theta$  measured into the aqueous phase is normally smaller than 90° and a larger fraction of the particle surface resides in water than in oil. For hydrophobic particles,  $\theta$  is generally greater than 90° and the particle resides more in oil than in water. Thus, the monolayers of hydrophilic particles will curve and tend to form oil-in-water (O/W) emulsions whereas hydrophobic particles form water-in-oil (W/O) emulsions. For  $\theta = 90^\circ$ , it means that a particle is amphiphilic and the ability of stabilizing emulsions is the most powerful.

In general, it is difficult to measure the contact angle of individual particles when their primary particle sizes are below 100 nm. The three-phase contact angle of the nanoparticles could be measured using the compressed disk method reported by Yan *et al.* [27] and Kostakis *et al.* [28]. As shown in Figure 3a, the three-phase contact angle of pure SiO<sub>2</sub> is about 35°, meaning that the surfaces of them are more hydrophilic. While the  $\theta$  of modified nano-SiO<sub>2</sub> particles is nearly 90° (Figure 3b), implying that the surface of modified SiO<sub>2</sub> should be amphiphilic. In order to confirm the surface wettability, the behavior of modified nano-SiO<sub>2</sub> suspended in a toluene/ water dual-phase mixture was observed. As shown in Figure 4a, modified nano-

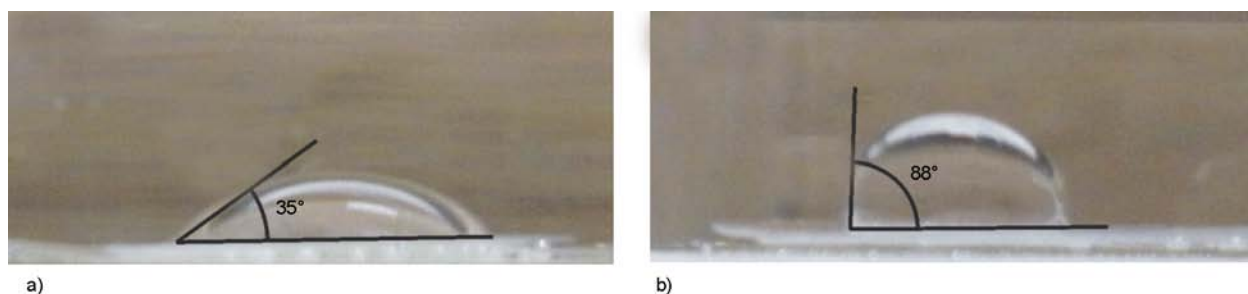


**Figure 3.** Three-phase contact angle determination photographs of pure SiO<sub>2</sub> (a) and modified SiO<sub>2</sub> (b)

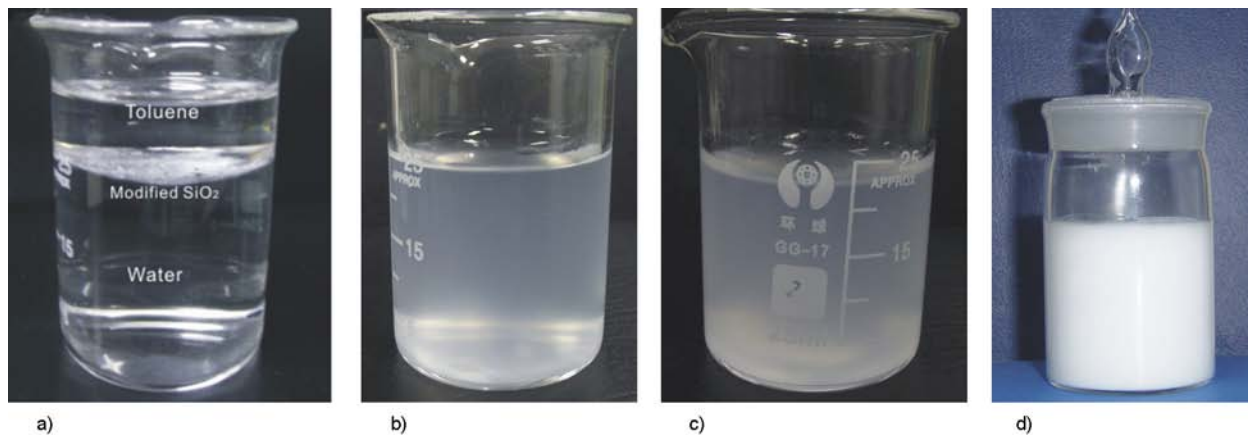


**Figure 4.** Digital photographs of distribution in toluene-water interface of modified nano-SiO<sub>2</sub> (a), aqueous modified nano-SiO<sub>2</sub> dispersions (b), dispersions of modified nano-SiO<sub>2</sub> in toluene (c) and O/W Pickering emulsion (d)

SiO<sub>2</sub> spread out and assemble spontaneously at the toluene-water interface. The subsequent dispersibility results demonstrate that the modified SiO<sub>2</sub> can easily disperse in both water and oily solvent such as benzene, toluene or liquid paraffin at nano-scale under ultrasonic conditions (Figure 4b and 4c). Based on the obvious amphipathic character, a stable O/W Pickering emulsion should be certainly obtained using this modified nano-SiO<sub>2</sub> as stabilizer (Figure 4d).

### 3.2. Mechanism analysis of PS/SiO<sub>2</sub> composite microspheres prepared by Pickering emulsion polymerization initiated by different initiators

The mechanism of conventional emulsion polymerization stabilized by surfactants has been discussed for several decades and some consensus has been reached [29–31]. That is, depending on the recipes and reaction conditions, one or more particle nucleation mechanisms, such as micelle nucleation, homo-

geneous nucleation and monomer droplet nucleation, are operative in emulsion polymerization [32]. Based on the fundamental understandings in conventional emulsion polymerization and taking into account the differences between modified nanoparticles and surfactant molecules, the possible Pickering emulsion polymerization mechanisms were studied by using oil-soluble AIBN and water-soluble APS as initiator respectively. Since the nanoparticles do not form micelles like surfactant molecules, micelle nucleation is excluded. Thus, there are two possible nucleation mechanisms involved. On the one hand, AIBN was used as the initiator in the initial stage of Pickering emulsion polymerization. Figure 5 shows the TEM (Figure 5a) and SEM (Figure 5b) images of composite microspheres I. It is clearly visible that the surfaces of polystyrene particles are covered with a dense layer of nano-SiO<sub>2</sub>. The microspheres are between 0.5~2.0 μm in diameter and the surfaces of them are rough. These observations suggest that the Pickering emulsion

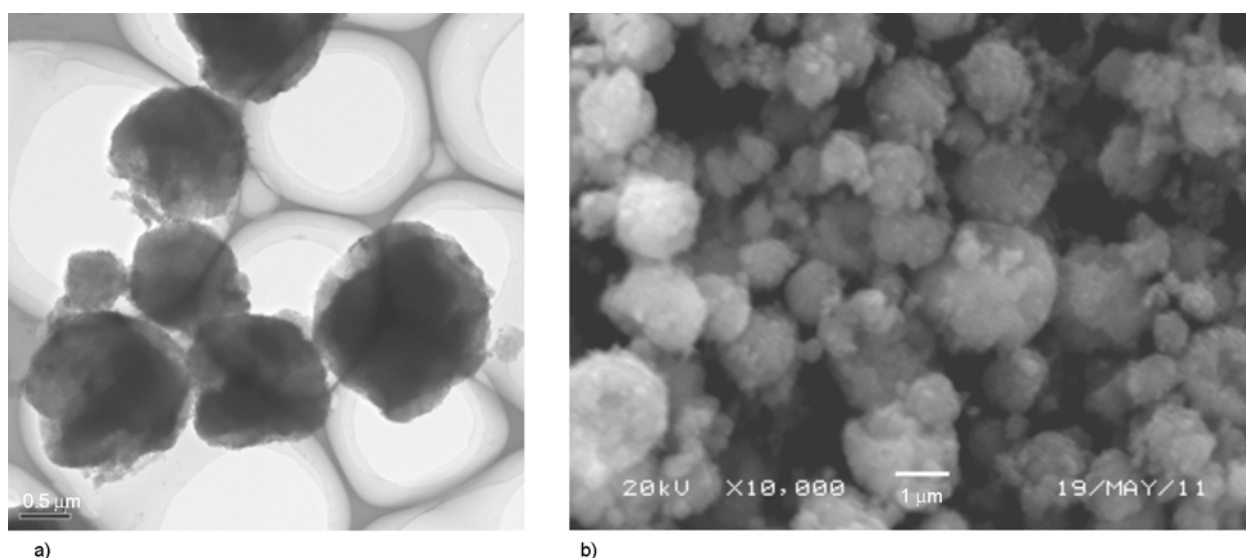


Figure 5. TEM image (a) and SEM image (b) of PS/SiO<sub>2</sub> composite microspheres I

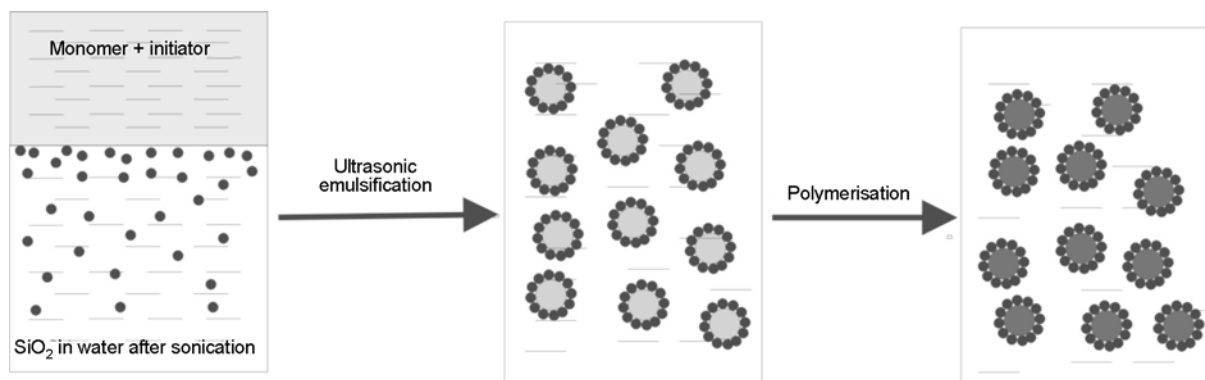
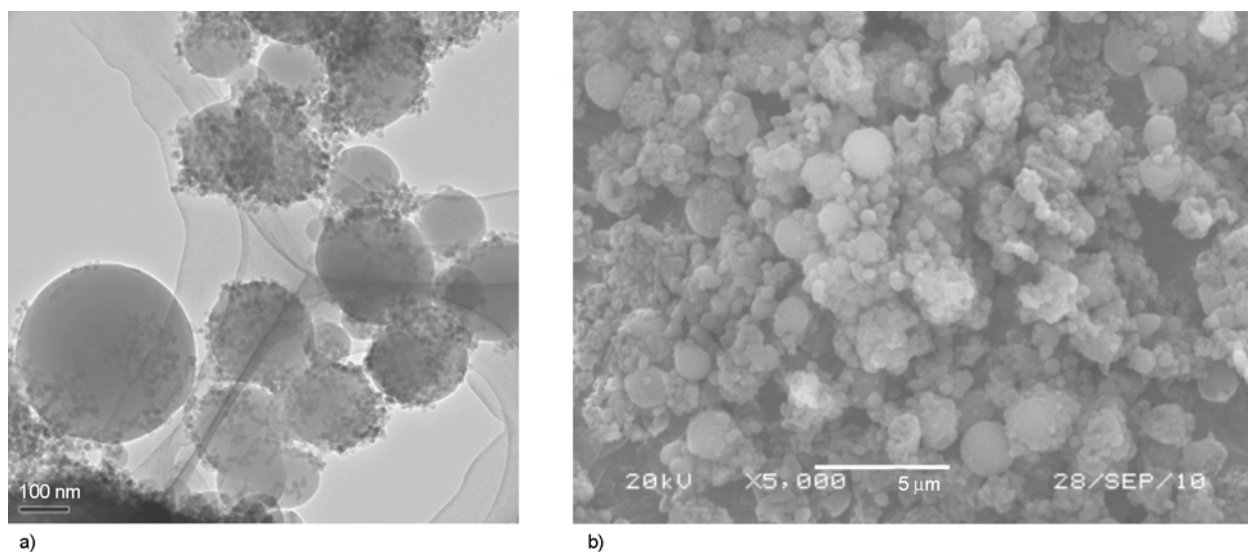


Figure 6. Schematic of the fabrication of composite microspheres I

polymerization using AIBN as the initiator mainly obeys the monomer droplet nucleation mechanism [33, 34]. Figure 6 shows the suggested formation mechanism of composite microspheres I. After being treated by ultrasound, nano-SiO<sub>2</sub> particles self-assemble at the O/W interface and act as effective stabilizers to generate O/W type Pickering emulsion droplets. Based on the hydrophobicity of AIBN, the polymerization reaction occurs mainly in inner oil phase composed of styrene monomer and AIBN. The silica nanoparticles initially adsorbed at droplet interfaces still remain at the interface during the polymerization as the droplets solidify, which could lead to high silica coverage of these composite microspheres, resulting in the compact core-shell morphology.

On the other hand, when the initiator was changed into hydrophilic APS, totally different results were observed. The TEM and SEM images of the composite microspheres II are shown in Figure 7a and Figure 7b, respectively. The diameters of the microspheres are sub-micron-sized (0.1~0.5 μm) and

smaller than those of composite microspheres I. It can be seen that a small amount of nano-SiO<sub>2</sub> are loosely located at the outside surfaces of polystyrene microspheres. For APS initiation Pickering emulsion system, initiator and monomer exist separately in water and oil phase, the homogeneous coagulative nucleation is likely to be the dominating mechanism. Figure 8 shows the possible formation mechanism of composite microspheres II. Upon APS decomposition, free radicals form in the aqueous phase, a small quantity of styrene monomers which dissolve in the water react with the decomposed initiator and form primary polymer chain, i. e. oligomers. After the growing oligomers reach a critical length, they are no longer dissolved in water, but coagulate to form nuclei and further grow into monomer swollen primary particles. With the continuous supply of styrene molecules from the monomer droplets through diffusion, the particles could grow either via swelling of particles by monomers or deposition of oligomers onto their surfaces. After the exhaustion of monomers in the



**Figure 7.** TEM image (a) and SEM image (b) of PS/SiO<sub>2</sub> composite microspheres II

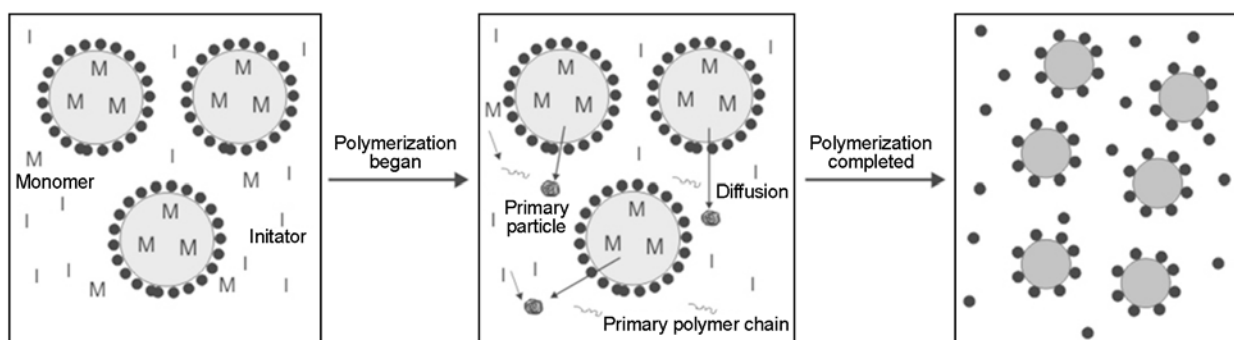


**Figure 8.** Illustration of the fabrication of composite microspheres II

droplets, the nano-SiO<sub>2</sub> initially adsorbed at droplets interfaces might re-disperse in the aqueous phase gradually, and some of them would self-assemble at the surfaces of the newly created polystyrene microspheres. However, it is likely due to the steric hindrance of nanoparticles or the repulsive interaction between the anionic initiator residues and the negatively charged nano-SiO<sub>2</sub> [35], the polystyrene microspheres are barely covered with silica nanoparticles and show loose core-shell morphology.

### 3.3. Characterization on the structure of PS/SiO<sub>2</sub> composite microspheres

The FTIR spectra of pure PS, modified SiO<sub>2</sub> and two kinds of PS/nano-SiO<sub>2</sub> composite microspheres are shown in Figure 9. In FTIR spectrum of pure PS (Figure 9a), the peak at 699 and 756 cm<sup>-1</sup> are attributed to flexural vibrations ( $\delta$ C–H) of the benzene ring and those at 1453, 1493, and 1602 cm<sup>-1</sup> correspond to benzene ring vibrations ( $\nu$ C–C) of polystyrene. The FTIR spectrum of modified SiO<sub>2</sub> (Figure 9b) shows the typical IR adsorption signal from silica at wave numbers of 472, 803 and 1100 cm<sup>-1</sup>, which are assigned to the bending vibration, symmetrical and asymmetrical stretching vibrations of Si–O–Si bonds. The absorption peaks at 2927 and 2855 cm<sup>-1</sup> correspond to the –CH<sub>2</sub> groups of dodecyltrimethoxysilane, showing that the long chain alkyl has bonded to the surface of nano-SiO<sub>2</sub> particles. In FTIR spectrum of two kinds of PS/nano-SiO<sub>2</sub> composite microspheres (Figure 9c and 9d), all the major characteristic spectral bands of composite are not significantly different from the FTIR spec-

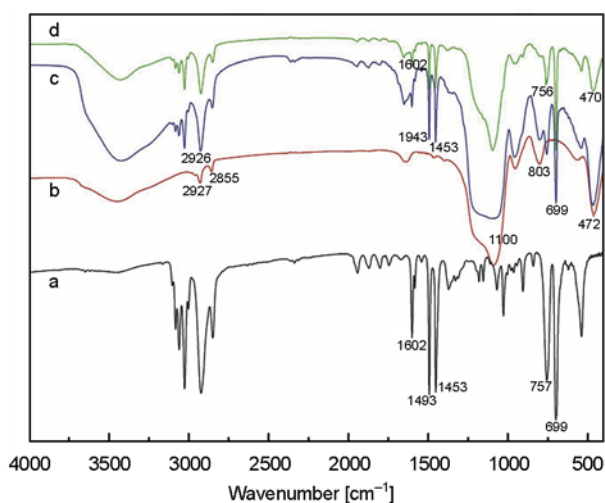


**Figure 9.** FTIR spectra of pure PS (a), modified SiO<sub>2</sub> (b) and two kinds of PS/nano-SiO<sub>2</sub> composite microspheres (c, d)

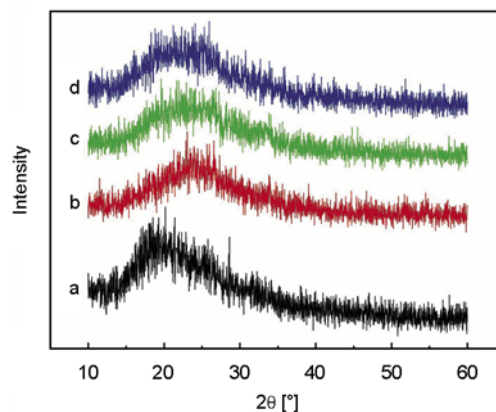


**Figure 10.** XRD patterns of: (a) PS; (b) nano-SiO<sub>2</sub>; (c) PS/SiO<sub>2</sub> composite microspheres I; (d) PS/SiO<sub>2</sub> composite microspheres II

trum of pure PS and modified SiO<sub>2</sub>. It indicates that PS/SiO<sub>2</sub> composite was successfully synthesized in this work.

The XRD patterns of the PS, nano-SiO<sub>2</sub> and as-prepared two kinds of composite microspheres are given in Figure 10. The broad non-crystalline diffraction peak at  $2\theta$  of about 19° (Figure 10a) corresponds to the amorphous polymer PS [36] and the wide peak at 22–26° (Figure 10b) is assigned to amorphous SiO<sub>2</sub> [37]. In Figure 10c and 10d, it is clearly observed that XRD patterns of two kinds of composite microspheres are more consistent with that of SiO<sub>2</sub> nanoparticles. This means that the main component in the surface of the composite microspheres is SiO<sub>2</sub>. The result again confirms the fact that SiO<sub>2</sub> particles are covered on the surface of PS cores and the core-shell structure is successfully formed.

After eliminating nano-SiO<sub>2</sub> located at the surfaces of composite microspheres by hydrofluoric acid

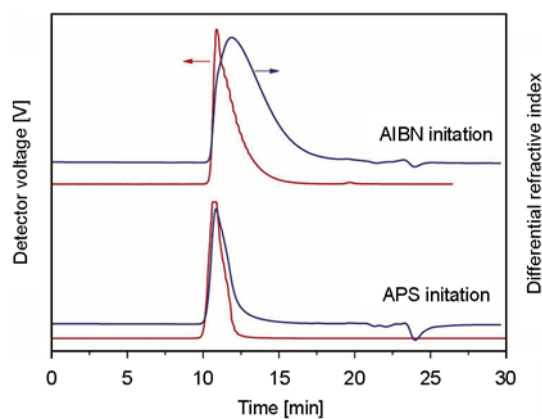


**Figure 11.** GPC curves of polystyrene prepared by Pickering emulsion polymerization initiated by different initiator



**Table 2.** Results of molecular weight and polydispersity of PS prepared by Pickering emulsion polymerization initiated by different initiator

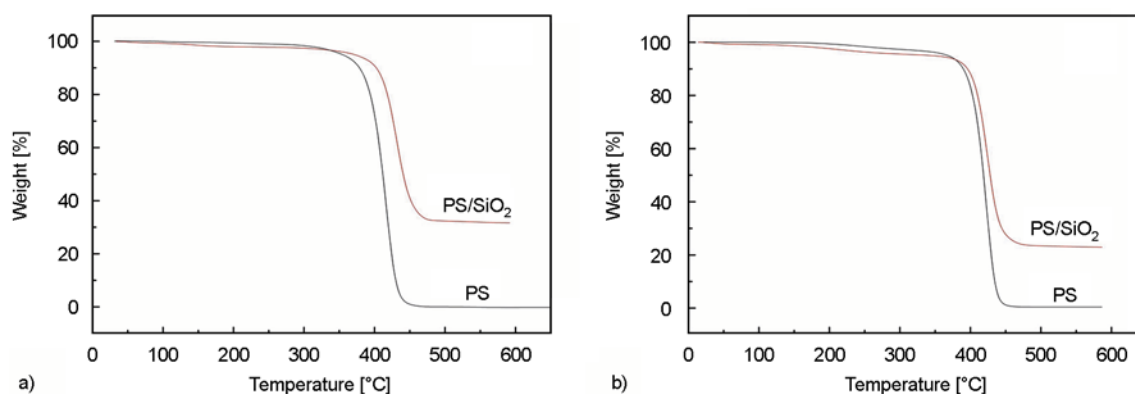
Sample name	Molar mass moments [g/mol]		Polydispersity index
	$M_n$	$M_w$	$M_w/M_n$
AIBN initiation	$2.300 \cdot 10^4$	$4.780 \cdot 10^4$	2.078
APS initiation	$2.215 \cdot 10^5$	$3.411 \cdot 10^5$	1.540

etching, the molecular weight and molecular weight distribution of the resultant PS were characterized by GPC-MALLS. The GPC curves are presented in Figure 11, and the according molecular weight and molecular weight distribution are summarized in Table 2. The results indicate that the molecular weight and molecular-weight distribution of PS using APS as initiator are higher and narrower than that of PS using AIBN as initiator. It can be explained according to the different nucleation mechanism analyzed above. For AIBN initiation system, hydrophobic AIBN and styrene monomer are both in the oil droplets during polymerization process, active chains are easier to terminate with free radicals generated by AIBN, so polystyrene with low molecular weight and broader molecular-weight distribution is obtained. When hydrophilic initiator APS is used, on the contrary, the free radicals generated by APS are captured by the nuclei in the aqueous phase. And they would remain active over a much longer time for the effect of isolation and embedding. In this case, polystyrene of higher molecular weight and narrower molecular weight distribution is synthesized.

### 3.4. Thermal properties analysis of PS/SiO<sub>2</sub> composite microspheres

The thermal decomposition behaviors of composite microspheres I and II were analyzed by TGA, as

shown in Figure 12a and 12b, respectively. Two samples including the composite microspheres and the corresponding pure PS after removal of the silica component were measured in each group. The results show that both of thermo decomposition temperatures of two composite microspheres are obviously higher than those of corresponding pure PS. This improvement on the thermal stability of composite microspheres is certainly attributed to the protective effect of nano-SiO<sub>2</sub> shell, which restricts the thermal motion of PS chains and shields the degradation of PS in the composite microspheres. Furthermore, there is an evident positive correlation between the content of silica in the composite and thermo decomposing temperatures. As indicated by the Figure 12a, the silica weight content is about 31.6% and the corresponding temperature of the fastest decomposing rate is about 424°C. However, the silica weight content is about 20.1% and the corresponding temperature of the fastest decomposing rate is about 417°C (Figure 12b). DSC curves of the composite microspheres I and II and their corresponding pure PS are shown in Figure 13a and 13b, respectively. Similarly,  $T_g$  of two kinds of composite microspheres are higher than those of corresponding pure PS. It is an further evidence that the existence of inorganic shells can contribute to improve the thermal performance of composite microspheres.

**Figure 12.** TGA curves of PS/SiO<sub>2</sub> composite and corresponding pure PS prepared by Pickering emulsion polymerization initiated by AIBN (a) and APS (b)

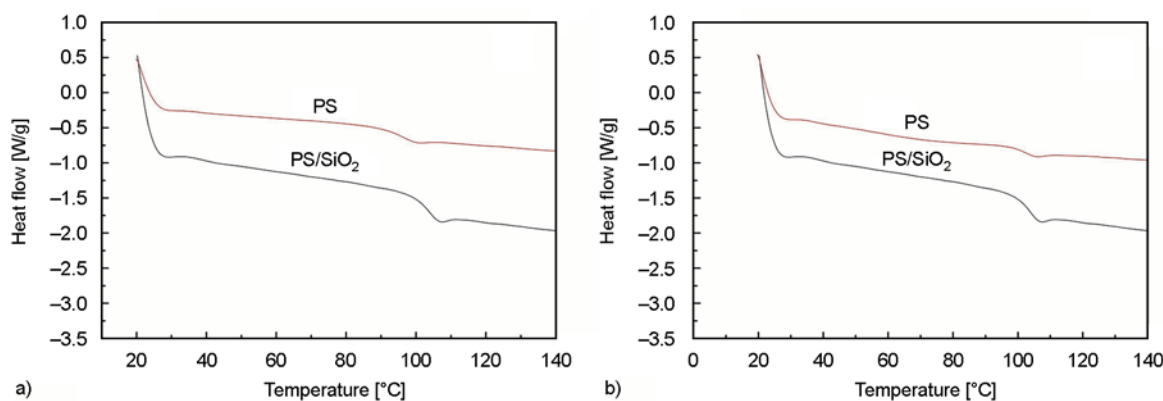


**Figure 13.** DSC curves of pure PS and PS/SiO<sub>2</sub> composite prepared by Pickering emulsion polymerization initiated by AIBN (a) and APS (b)

#### 4. Conclusions

In conclusion, two kinds of PS/SiO<sub>2</sub> composite microspheres with core-shell structure have been successfully synthesized via Pickering emulsion polymerization using amphiphilic silica nanoparticles as the stabilizers. When hydrophobic AIBN was used as the initiator, the composite microspheres could be micron-sized and high silica coverage. While the sub-micron-sized and barely covered composite microspheres could be obtained by using hydrophilic APS as the initiator. The monomer droplet nucleation was considered as the dominating mechanism in Pickering emulsion polymerization when using AIBN as the initiator, whereas homogeneous coagulative nucleation could be proposed as the polymerization mechanism in the system with APS. TG and DSC analysis suggests that the thermal stability of the composite microspheres is higher than that of the corresponding pure polystyrene.

#### Acknowledgements

The authors gratefully acknowledge the National Natural Science Foundation of China (Grant No. 21004049) and Scientific Research Fund of Xianyang Normal university (No. 10XSYK302) for financial support. W. Tian sincerely thanks the support from the ‘Soar Star’ project of NPU.

#### References

- [1] Jeon I-Y., Baek J-B.: Nanocomposites derived from polymers and inorganic nanoparticles. *Materials*, **3**, 3654–3674 (2010).  
DOI: [10.3390/ma3063654](https://doi.org/10.3390/ma3063654)

- [2] Berta M., Lindsay C., Pans G., Camino G.: Effect of chemical structure on combustion and thermal behaviour of polyurethane elastomer layered silicate nanocomposites. *Polymer Degradation and Stability*, **91**, 1179–1191 (2006).  
DOI: [10.1016/j.polymdegradstab.2005.05.027](https://doi.org/10.1016/j.polymdegradstab.2005.05.027)
- [3] Sanchez C., Julián B., Belleville P., Popall M.: Applications of hybrid organic–inorganic nanocomposites. *Journal of Materials Chemistry*, **15**, 3559–3592 (2005).  
DOI: [10.1039/B509097K](https://doi.org/10.1039/B509097K)
- [4] Agrawal M., Gupta S., Stamm M.: Recent developments in fabrication and applications of colloid based composite particles. *Journal of Materials Chemistry*, **21**, 615–627 (2011).  
DOI: [10.1039/C0JM02631J](https://doi.org/10.1039/C0JM02631J)
- [5] Hu J., Chen M., Wu L.: Organic-inorganic nanocomposites synthesized *via* miniemulsion polymerization. *Polymer Chemistry*, **2**, 760–772 (2011).  
DOI: [10.1039/C0PY00284D](https://doi.org/10.1039/C0PY00284D)
- [6] Nagao D., Yokoyama M., Saeki S., Kobayashi Y., Konno M.: Preparation of composite particles with magnetic silica core and fluorescent polymer shell. *Colloid and Polymer Science*, **286**, 959–964 (2008).  
DOI: [10.1007/s00396-008-1855-5](https://doi.org/10.1007/s00396-008-1855-5)
- [7] Guo Y., Wang M., Zhang H., Liu G., Zhang L., Qu X.: The surface modification of nanosilica, preparation of nanosilica/acrylic core-shell composite latex, and its application in toughening PVC matrix. *Journal of Applied Polymer Science*, **107**, 2671–2680 (2008).  
DOI: [10.1002/app.27310](https://doi.org/10.1002/app.27310)
- [8] Kai Z., Qiang F., Jinghui F., Dehui Z.: Preparation of Ag/PS composite particles by dispersion polymerization under ultrasonic irradiation. *Materials Letters*, **59**, 3682–3686 (2005).  
DOI: [10.1016/j.matlet.2005.06.063](https://doi.org/10.1016/j.matlet.2005.06.063)
- [9] Zhao Y., Wang H., Song X., Du Q.: Fabrication of two kinds of polymer microspheres stabilized by modified titania during Pickering emulsion polymerization. *Macromolecular Chemistry and Physics*, **211**, 2517–2529 (2010).  
DOI: [10.1002/macp.201000512](https://doi.org/10.1002/macp.201000512)

- [10] Liu H., Wang C., Gao Q., Chen J., Liu X., Tong Z.: One-pot fabrication of magnetic nanocomposite microcapsules. *Materials Letters*, **63**, 884–886 (2009). DOI: [10.1016/j.matlet.2009.01.034](https://doi.org/10.1016/j.matlet.2009.01.034)
- [11] Jeng J., Chen T-Y., Lee C-F., Liang N-Y., Chiu W-Y.: Growth mechanism and pH-regulation characteristics of composite latex particles prepared from Pickering emulsion polymerization of aniline/ZnO using different hydrophilicities of oil phases. *Polymer*, **49**, 3265–3271 (2008). DOI: [10.1016/j.polymer.2008.05.027](https://doi.org/10.1016/j.polymer.2008.05.027)
- [12] Wang C., Zhang C., Li Y., Chen Y., Tong Z.: Facile fabrication of nanocomposite microspheres with polymer cores and magnetic shells by Pickering suspension polymerization. *Reactive and Functional Polymers*, **69**, 750–754 (2009). DOI: [10.1016/j.reactfunctpolym.2009.06.003](https://doi.org/10.1016/j.reactfunctpolym.2009.06.003)
- [13] Hasell T., Yang J., Wang W., Li J., Brown P. D., Poliakoff M., Lester E., Howdle S. M.: Preparation of polymer–nanoparticle composite beads by a nanoparticle-stabilised suspension polymerisation. *Journal of Materials Chemistry*, **17**, 4382–4386 (2007). DOI: [10.1039/B705917E](https://doi.org/10.1039/B705917E)
- [14] Barthet C., Hickey A. J., Cairns D. B., Armes S. P.: Synthesis of novel polymer–silica colloidal nanocomposites via free-radical polymerization of vinyl monomers. *Advanced Materials*, **11**, 408–410 (1999). DOI: [10.1002/\(SICI\)1521-4095\(199903\)11:5<408::AID-ADMA408>3.0.CO;2-Y](https://doi.org/10.1002/(SICI)1521-4095(199903)11:5<408::AID-ADMA408>3.0.CO;2-Y)
- [15] Binks B. P., Lumsdon S. O.: Influence of particle wettability on the type and stability of surfactant-free emulsions. *Langmuir*, **16**, 8622–8631 (2000). DOI: [10.1021/la000189s](https://doi.org/10.1021/la000189s)
- [16] Binks B. P., Rodrigues J. A.: Types of Phase inversion of silica particle stabilized emulsions containing triglyceride oil. *Langmuir*, **19**, 4905–4912 (2003). DOI: [10.1021/la020960u](https://doi.org/10.1021/la020960u)
- [17] Binks B. P., Desforges A.: Synergistic stabilization of emulsions by a mixture of surface-active nanoparticles and surfactant. *Langmuir*, **23**, 1098–1106 (2007). DOI: [10.1021/la062510y](https://doi.org/10.1021/la062510y)
- [18] Midmore B. R.: Effect of aqueous phase composition on the properties of a silica-stabilized W/O emulsion. *Journal of Colloid and Interface Science*, **213**, 352–359 (1999). DOI: [10.1006/jcis.1999.6108](https://doi.org/10.1006/jcis.1999.6108)
- [19] Bon S. A. F., Mookhoek S. D., Colver P. J., Fischer H. R., van der Zwaag S.: Route to stable non-spherical emulsion droplets. *European Polymer Journal*, **43**, 4839–4842 (2007). DOI: [10.1016/j.eurpolymj.2007.09.001](https://doi.org/10.1016/j.eurpolymj.2007.09.001)
- [20] Colver P. J., Chen T., Bon S. A. F.: Supracolloidal structures through liquid-liquid interface driven assembly and polymerization. *Macromolecular Symposia*, **245–246**, 34–41 (2006). DOI: [10.1002/masy.200651306](https://doi.org/10.1002/masy.200651306)
- [21] Bon S. A. F., Colver P. J.: Pickering miniemulsion polymerization using laponite clay as a stabilizer. *Langmuir*, **23**, 8316–8322 (2007). DOI: [10.1021/la701150q](https://doi.org/10.1021/la701150q)
- [22] Zaragoza-Contreras E. A., Hernández-Escobar C. A., Navarrete-Fontes A., Flores-Gallardo S. G.: Synthesis of carbon black/polystyrene conductive nanocomposite. Pickering emulsion effect characterized by TEM. *Micron*, **42**, 263–270 (2011). DOI: [10.1016/j.micron.2010.10.005](https://doi.org/10.1016/j.micron.2010.10.005)
- [23] Zhang K., Wu W., Guo K., Chen J., Zhang P.: Synthesis of temperature-responsive poly(*N*-isopropyl acrylamide)/poly(methyl methacrylate)/silica hybrid capsules from inverse Pickering emulsion polymerization and their application in controlled drug release. *Langmuir*, **26**, 7971–7980 (2010). DOI: [10.1021/la904841m](https://doi.org/10.1021/la904841m)
- [24] He Y., Yu X.: Preparation of silica nanoparticle-armed polyaniline microspheres in a Pickering emulsion. *Materials Letters*, **61**, 2071–2074 (2007). DOI: [10.1016/j.matlet.2006.08.018](https://doi.org/10.1016/j.matlet.2006.08.018)
- [25] Choi H., Chen I-W.: Surface-modified silica colloid for diagnostic imaging. *Journal of Colloid and Interface Science*, **258**, 435–437 (2003). DOI: [10.1016/S0021-9797\(02\)00130-3](https://doi.org/10.1016/S0021-9797(02)00130-3)
- [26] Aveyard R., Binks B. P., Clint J. H.: Emulsions stabilised solely by colloidal particles. *Advances in Colloid and Interface Science*, **100–102**, 503–546 (2003). DOI: [10.1016/S0001-8686\(02\)00069-6](https://doi.org/10.1016/S0001-8686(02)00069-6)
- [27] Yan N., Masliyah J. H.: Effect of pH on adsorption and desorption of clay particles at oil–water interface. *Journal of Colloid and Interface Science*, **181**, 20–27 (1996). DOI: [10.1006/jcis.1996.0352](https://doi.org/10.1006/jcis.1996.0352)
- [28] Kostakis T., Ettelaie R., Murray B. S.: Effect of high salt concentrations on the stabilization of bubbles by silica particles. *Langmuir*, **22**, 1273–1280 (2006). DOI: [10.1021/la052193f](https://doi.org/10.1021/la052193f)
- [29] Harkins W. D.: A general theory of the mechanism of emulsion polymerization. *Journal of the American Chemical Society*, **69**, 1428–1444 (1947). DOI: [10.1021/ja01198a053](https://doi.org/10.1021/ja01198a053)
- [30] Kolthoff I. M., Meehan E. J., Carr E. M.: Mechanism of initiation of emulsion polymerization by persulfate. *Journal of the American Chemical Society*, **75**, 1439–1441 (1953). DOI: [10.1021/ja01102a048](https://doi.org/10.1021/ja01102a048)
- [31] Ma G., Li J.: Compromise between dominant polymerization mechanisms in preparation of polymer microspheres. *Chemical Engineering Science*, **59**, 1711–1721 (2004). DOI: [10.1016/j.ces.2004.01.027](https://doi.org/10.1016/j.ces.2004.01.027)
- [32] Chern C. S.: Emulsion polymerization mechanisms and kinetics. *Progress in Polymer Science*, **31**, 443–486 (2006). DOI: [10.1016/j.progpolymsci.2006.02.001](https://doi.org/10.1016/j.progpolymsci.2006.02.001)

- [33] Chen J. H., Cheng C-Y., Chiu W-Y., Lee C-F., Liang N-Y.: Synthesis of ZnO/polystyrene composites particles by Pickering emulsion polymerization. *European Polymer Journal*, **44**, 3271–3279 (2008).  
DOI: [10.1016/j.eurpolymj.2008.07.023](https://doi.org/10.1016/j.eurpolymj.2008.07.023)
- [34] Zhang K., Wu W., Meng H., Guo K., Chen J-F.: Pickering emulsion polymerization: Preparation of polystyrene/nano-SiO<sub>2</sub> composite microspheres with core-shell structure. *Powder Technology*, **190**, 393–400 (2009).  
DOI: [10.1016/j.powtec.2008.08.022](https://doi.org/10.1016/j.powtec.2008.08.022)
- [35] Ma H., Luo M., Sanyal S., Rege K., Dai L. L.: The one-step Pickering emulsion polymerization route for synthesizing organic-inorganic nanocomposite particles. *Materials*, **3**, 1186–1202 (2010).  
DOI: [10.3390/ma3021186](https://doi.org/10.3390/ma3021186)
- [36] Wu D., Ge X., Huang Y., Zhang Z., Ye Q.:  $\gamma$ -radiation synthesis of silver–polystyrene and cadmium sulfide–polystyrene nanocomposite microspheres. *Materials Letters*, **57**, 3549–3553 (2003).  
DOI: [10.1016/S0167-577X\(03\)00123-X](https://doi.org/10.1016/S0167-577X(03)00123-X)
- [37] Wang C., Yan J., Cui X., Wang H.: Synthesis of raspberry-like monodisperse magnetic hollow hybrid nanospheres by coating polystyrene template with Fe<sub>3</sub>O<sub>4</sub>@SiO<sub>2</sub> particles. *Journal of Colloid and Interface Science*, **354**, 94–99 (2011).  
DOI: [10.1016/j.jcis.2010.09.078](https://doi.org/10.1016/j.jcis.2010.09.078)



# Studies on positive conveying in helically channeled single screw extruders

L. Pan, M. Y. Jia, P. Xue\*, K. J. Wang, Z. M. Jin

Institute of Plastic Machinery and Engineering, Beijing University of Chemical Technology, 100029 Beijing, China

Received 5 November 2011; accepted in revised form 20 January 2012

**Abstract.** A solids conveying theory called double-flight driving theory was proposed for helically channeled single screw extruders. In the extruder, screw channel rotates against static barrel channel, which behaves as cooperative embedded twin-screws for the positive conveying. They turn as two parallel arc plates, between which an arc-plate solid-plug was assumed. By analyzing the forces on the solid-plug in the barrel channel and screw channel, the boundary conditions when the solid-plug is waived of being cut off on barrel wall, were found to have the capacity of the positive conveying. Experimental data were obtained using a specially designed extruder with a helically channeled barrel in the feeding zone and a pressure-adjustable die. The effects of the barrel channel geometry and friction coefficients on the conveying mechanism were presented and compared with the experimental results. The simulations showed that the positive conveying could be achieved after optimizing extruder designs. Compared with the traditional design with the friction-drag conveying, the throughput is higher while screw torque and energy consumption are decreased. Besides, the design criteria of the barrel channel were also discussed.

**Keywords:** processing technologies, double-flight driving theory, positive conveying, helical barrel channels, solids conveying

## 1. Introduction

Single screw extruders were widely used as one of the basic and convenient elements to melt and convey polymer materials. It was usual to consider single-screw extruders being composed of solids conveying zone, melting zone, and melt conveying zone. Attention was here paid to the solids conveying zone closely related to the performance of the extruders.

The classical solids conveying theory, called Darnell-Mol theory, demonstrated that the friction force on the barrel internal surface must be larger than that on the screw surface for effective solids conveying and steady extrusion. An effective solution to improve feeding efficiency is to groove barrel surface along the axial direction as introduced by Menges at the Institute of Plastics Processing

(IKV) in Aachen in 1960's because the grooves greatly increases the apparent friction coefficient at the barrel-solid plug interface. Later, the effects of structural parameters on the apparent friction coefficient of the barrel were studied by Rautenbach [1], Grünschloß [2] and Potente [3]. Due to the improved barrel friction coefficient, higher pressure results in higher throughput with better stability than conventional systems, which facilitates processing high molecular weight polymer and highly filled materials [4–6]. However, such screw consumes more energy as well as greater wearing than common screws [5, 7–9].

In recent years, some advances were made on the designs of the groove structural parameters to improve the performance of the solids conveying zone. Helical grooves were first invented in the

\*Corresponding author, e-mail: [buct\\_nme@sohu.com](mailto:buct_nme@sohu.com)  
© BME-PT

1970's for decreasing the deflection of the groove flow in the peripheral direction. Later, the superiority of helical grooves was testified by Kramer's experiment [10] and analyzed mathematically by Grünshloß [11, 12] and Miethlinger [13]. Their researches indicated that helical grooves improved the throughput much higher than axial grooves. Later, the groove adjustable continuously in geometry was used in extruders [14] and showed great advantages in controlling the solids conveying efficiency and in widening the range of materials, which was confirmed by Rauwendaal and Sikora [14], Kowalska [15] and Sikora [16]. However, the adjustable extruder has not been widely applied due to its complexity and high cost of the adjustable mechanism. The theory on solids conveying of grooved barrel extruders were also studied and modified. Rautenbach and Peiffer [17] proposed an in-depth model to determine the conveying performance of the grooved section in single-screw extruders in 1982. Potente [18] established a new throughput model in which the solids were divided into two parts, including pellets flow in the screw channel and those flow in the barrel grooves. The effects of the pressure gradient and particle size on the solids conveying angle were also analyzed by Potente [19]. Besides, optimal design of the groove helical angle was conducted by considering the effects of the pressure gradient and friction coefficient on the conveying efficiency by Rauwendaal [20]. In 2001, Potente and Phol [21] attempted to model the two-dimensional approach flow of pellets using the discrete element method. Moysey and coworkers [22–24] utilized the discrete element method to further analyze the flow characteristics of pellets with a three-dimensional model. Michelangelli *et al.* [25] extended Potente and Monysey's efforts and investigated the effect of the average pellet size on the dynamics of the granular flow.

However, in the previous models based on the friction-drag conveying mechanism, the effects of both axial and helical grooves were only assumed to increase the mean friction coefficient of the barrel on solid pellets, by which the friction force between the barrel and the solids is the active force and the friction force between the screw and the solids is the resistant force. Shear fracture occurs on the interface between the groove and screw channel in above friction-drag conveying mechanism, so there

is no positive conveying in single screw extruders. Thus, these designs based on the friction-drag conveying models have disadvantages such as larger motor load, energy consumption and rapid wear.

For solving these questions, large barrel channels, not grooves, were developed in this study to achieve the positive conveying in the solids conveying zone based on a new solids conveying theory called double-flight driving theory. In the theory, static helical barrel channels and rotating screw were regarded as a cooperative system similar to the counter-rotating twin-screws. The solids in the barrel channel and screw channel form one arc-plate solid-plug model, which is different from the traditional parallel-plate model as shown in Figure 1. From the mathematical model, the boundary condition equations for the positive conveying in single-screw extruders and the pressure equation in the solids conveying zone were established. Based on these, the design criteria for the helically channeled single screw extruders with the positive conveying were discussed, simulations were conducted, and experimental studies were carried out to verify this model.

## 2. Physical model

### 2.1. Arc-plate model

The physical model called arc-plate model in the double-flight driving theory is shown in Figure 1. The feeding barrel sleeve is helically channeled such that pellets flow into the screw channel and fill in the barrel channels. In the modeling, one solid-plug element is assumed to be composed of the solids filled in the screw channel and the connected ones limited in one helical barrel channel as Figure 1 shows. The element volume is formed by surrounding the plug element forward side and backward side along the helical screw channel, active flight

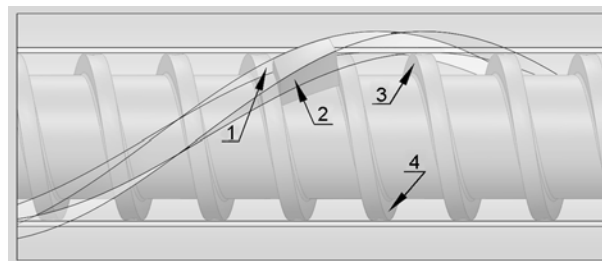


**Figure 1.** The arc-plate model for the screw extruder with the helically channeled barrel. 1. the active flight of the barrel channel, 2. the trailing flight of the barrel channel, 3. the trailing flight of the screw, 4. the active flight of the screw.

and trailing flight of the screw, and active flight and trailing flight of the barrel channel. The bottom surface and the top surface of the solid-plug element are in arcs parallel to the barrel channel bottom. The other four sides of the element are in planes. Thus, the element is called one arc-plate in modeling.

If no shear fracture occurs inside the arc-plate element with the screw rotating, the element will be pushed forward along the barrel channel direction by the barrel channel and screw flight. Such solids conveying process is called the positive conveying, similar to the counter-rotating twin-screw extruder. In the positive conveying, active forces from the active flights of the barrel channel and screw channel are driving forces, and friction forces from the barrel and screw surface are resistant forces. Thus, the barrel and screw can be manufactured smoothly to have low friction heat. More importantly, the material with low friction coefficient can be steadily conveyed along the barrel channel direction by the active forces. In order to achieve the positive conveying, we carried out the theoretical analysis in Section 3 and experimental study in Sections 4 and 5.

### 2.2. Basic assumptions

- (1) The granules or powder added in the hopper is compressed to form the solid-plug without internal slip in the solids conveying zone.
- (2) The solid-plug closely contacts with the six surfaces: the screw channel bottom, the active and trailing flight of the screw, the barrel channel bottom, and the active and trailing flight of the barrel channel.
- (3) The solid-plug is compressible and the bulk density is the function of the pressure.
- (4) The pressure of the solid-plug is the function of the distance along the screw channel direction.
- (5) In the barrel channel located in each screw pitch distance, the pressure gradient is ignored.
- (6) The friction coefficient, in terms of the Coulomb's Law, is a constant.
- (7) The barrel channels are approximated to be rectangular.
- (8) The clearance between the barrel and the screw is negligible.
- (9) The effects of the material gravity and the variation of the internal temperature inside the solid-plug are negligible.

## 3. Mathematical model

### 3.1. Velocities and accelerations of the solid-plug

In modeling, the barrel is assumed as the moving reference system relative to the static screw. The velocity of the solid-plug element is decomposed as shown in Figure 2. Axis  $Z$  is axial direction.  $\varphi$  is the screw channel helical angle at barrel wall,  $\varphi_N$  is the barrel channel helical angle in the barrel.  $V_b$  is the circumferential velocity of the barrel. The solids conveying mechanism is either the positive conveying or the friction-drag conveying. In the positive conveying, the solids move at a speed of  $V_S$  along the barrel channel direction while moving at  $V_r$  in the screw channel. In the friction-drag conveying, the solids are forwarded at  $V_{Sf}$  composited with  $V_{rf}$ . It can be seen that the conveying angle of the solid-plug in the positive conveying is much greater than that in the friction-drag conveying.

The inertia forces are not negligible in the solids moving, which make the solid pellets or powder into the barrel channels and further compact them. Figure 3 presents the acceleration decompositions of the solid-plug embedded in the barrel channel and screw channel.

Axis  $X$  is radial direction and axis  $Y$  is tangential direction. Due to the position variation of the mov-

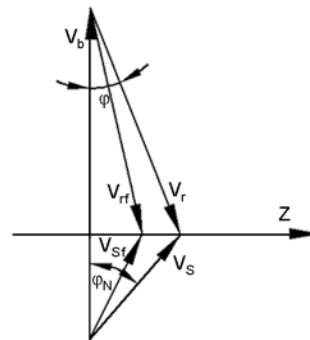


Figure 2. Velocity decompositions of the solid-plug in the positive conveying and the friction-drag conveying

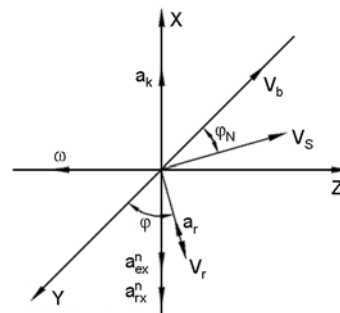


Figure 3. Acceleration decompositions of the solid-plug embedded in the barrel channel and screw channel

ing solid-plug against rotating screw, Coriolis acceleration is generated when the solid-plug moves at  $V_r$  along the screw channel direction as shown by Equation (1):

$$a_k = \frac{4V_b^2 \cos\varphi}{D \sin(\varphi_N + \varphi)} \quad (1)$$

The relative acceleration  $a_r$  resulting from the variation in  $V_r$  is given by Equation (2):

$$a_r = \frac{dV_r}{dt} \quad (2)$$

The velocities  $V_b$  and  $V_r$  can be decomposed into the tangential direction (Axis  $Y$ ). That is, normal acceleration  $a_n$  in the radial direction (Axis  $X$ ) includes  $a_{ex}^n$  and  $a_{rx}^n$  which can be calculated by Equation (3):

$$a_n = \frac{-2V_b^2 \sin^2\varphi \cos^2\varphi_N}{D \sin^2(\varphi_N + \varphi)} \quad (3)$$

where  $D$  is the outer diameter of the screw and  $t$  the time.

### 3.2. Force analysis

When pushing the solid-plug forward, the two active flights can be viewed as scissors resulting in a shear stress on the interface between the part of the solid-plug in the barrel channel and the rest in the screw channel. In order to determine the shear stress, the force analysis on the arc-plate model must be carried out. Figure 4 shows the forces on the solid-plug. Figure 5 displays the forces on the part embedded in the barrel channel. All of the forces are included in the following:

- (1) Main Inertia forces include  $I_n$ ,  $I_k$  and  $I_r$  caused by the centripetal acceleration, Coriolis acceleration and the relative acceleration, respectively.
- (2) Normal forces, some of them resulting from pressure  $P$ ,  $P_1$ ,  $P_2$ ,  $P_3$ ,  $P_4$ ,  $P_{51}$ ,  $P_{52}$ ,  $P_{61}$  and  $P_{62}$  per unit area on the surfaces of the solid-plug, others from friction  $F_{FP1}$ ,  $F_{FP2}$ ,  $F_{FP3}$ ,  $F_{FP4}$ ,  $F_{FP51}$  and  $F_{FP61}$ .

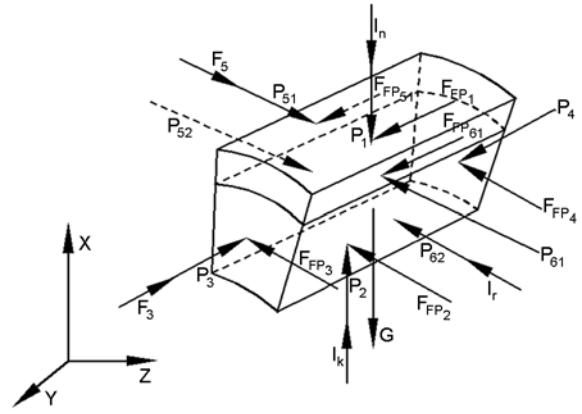


Figure 4. Forces on the solid-plug embedded in the barrel channel and screw channel

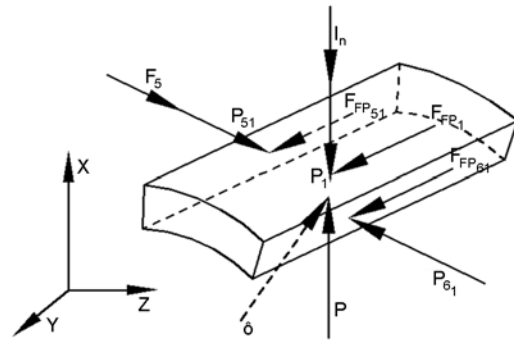


Figure 5. Forces on the solid-plug part embedded in the barrel channel

- (3) Active forces pushing solids forward are the force  $F_3$  from the active flight of the screw and the force  $F_5$  from the active flight of the barrel channel.
- (4) The screw rotates against the barrel such that there is an interface shear stress  $\delta$  between the part of the solid-plug in the barrel channel and the rest in the screw channel.

In all of these forces, the active force of the screw flight  $F_3$ , the active force of the barrel flight  $F_5$  and the interface shear stress  $\delta$  are unknown. Active forces  $F_3$  and  $F_5$  in Figure 4 can be determined from the torque balance around the screw axis (Axis  $Y$ ) and the force balance along the screw axis (Axis  $Z$ ). The following Equation (4) is obtained through the torque balance around the screw axis (Axis  $Y$ ):

$$\begin{aligned} & -F_{FP1} \cos\varphi_N \frac{D_{NS}}{2} + F_{FP2} \cos\varphi_S \frac{D_S}{2} + F_3 \sin\varphi_m \frac{D_m}{2} + F_{P3} \sin\varphi_m \frac{D_m}{2} + F_{FP3} \cos\varphi_m \frac{D_m}{2} - F_{P4} \sin\varphi_m \frac{D_m}{2} \\ & + F_{FP4} \cos\varphi_m \frac{D_m}{2} - F_5 \sin\varphi_N \frac{D_{Nm}}{2} - F_{P51} \sin\varphi_N \frac{D_{Nm}}{2} - F_{FP51} \cos\varphi_N \frac{D_{Nm}}{2} - I_r \cos\varphi_m \frac{D_m}{2} - F_{P52} \sin\varphi_N \frac{D_m}{2} \\ & + F_{P61} \sin\varphi_N \frac{D_{Nm}}{2} - F_{FP61} \cos\varphi_N \frac{D_{Nm}}{2} + F_{P62} \sin\varphi_N \frac{D_m}{2} = 0 \end{aligned} \quad (4)$$



The force balance along the screw axis (Axis Z) gives Equation (5):

$$\begin{aligned}
 & -F_{FP_1}\sin\varphi_N - F_{FP_2}\sin\varphi_S + F_3\cos\varphi_m + F_{P_3}\cos\varphi_m - F_{FP_3}\sin\varphi_m - F_{P_4}\cos\varphi_m - F_{FP_4}\sin\varphi_{mN} + F_5\cos\varphi \\
 & + F_{P_{51}}\cos\varphi_N - F_{FP_{51}}\sin\varphi_N + F_{P_{52}}\cos\varphi_N + I_t\sin\varphi_m - F_{P_{61}}\cos\varphi_N - F_{FP_{61}}\sin\varphi_N - F_{P_{62}}\cos\varphi_N = 0
 \end{aligned} \tag{5}$$

Combining Equations (4) and (5), it leads to Equation (6):

$$F_5 = (F_{P_1} + I_n) \frac{A_2}{A_1} + (F_{P_2} + I_k) \frac{A_3}{A_1} + F_{P_4} \frac{A_4}{A_1} - F_{P_{51}} + (F_{P_{62}} - F_{P_{52}}) \frac{A_5}{A_1} + F_{P_{61}} \frac{A_6}{A_1} - I_r \frac{A_7}{A_1} \tag{6}$$

where

$$A_1 = D_{Nm}(\cos\varphi_m - f_L\sin\varphi_m)(\sin\varphi_N + f_T\cos\varphi_N) + D_m(\sin\varphi_m + f_L\cos\varphi_m)(\cos\varphi_N - f_T\sin\varphi_N)$$

$$A_2 = f_T[\cos\varphi_N D_{NS}(f_L\sin\varphi_m - \cos\varphi_m) + \sin\varphi_N D_m(\sin\varphi_m + f_L\cos\varphi_m)]$$

$$A_3 = f_L[\cos\varphi_S D_S(\cos\varphi_m - f_L\sin\varphi_m) + \sin\varphi_S D_m(\sin\varphi_m + f_L\cos\varphi_m)]$$

$$A_4 = 2D_m f_L$$

$$A_5 = D_m[\sin\varphi_N(\cos\varphi_m - f_L\sin\varphi_m) + \cos\varphi_N(\sin\varphi_m + f_L\cos\varphi_m)]$$

$$A_6 = D_{Nm}(\cos\varphi_m - f_L\sin\varphi_m)(\sin\varphi_N - f_T\cos\varphi_N) + D_m(\sin\varphi_m + f_L\cos\varphi_m)(\cos\varphi_N + f_T\sin\varphi_N)$$

$$A_7 = D_m$$

$$F_{P_1} = P_1 b_N b$$

$$F_{P_2} = P_2 b_N b_S$$

$$F_{P_4} = P_4 b_N h$$

$$F_{P_{51}} = P_{51} b h_N$$

$$F_{P_{52}} = P_{52} b_m h$$

$$F_{P_{61}} = P_{61} b h_N$$

$$F_{P_{62}} = P_{62} b_m h$$

where  $A_i$  ( $i = 1, 2, 3, 4, 5, 6, 7$ ) are the parameters that are constant for a given barrel and screw as well as material,  $f_T$  the friction coefficient of the solids on the barrel,  $f_L$  the friction coefficient of the solids on the screw,  $D_{NS}$  the barrel channel root diameter,  $D_{Nm}$  the mean barrel channel diameter,  $D_S$  the screw root diameter,  $D_m$  the mean screw diameter,  $b_N$  the barrel channel width,  $b$  the screw channel width at barrel wall,  $b_S$  the screw channel width at screw root,  $b_m$  the mean screw channel width,  $h_N$  the barrel channel depth,  $h$  the screw channel depth,  $\varphi_S$  the

screw channel helical angle at screw root,  $\varphi_m$  the mean screw channel helical angle,  $F_{P_1}$ ,  $F_{P_2}$ ,  $F_{P_4}$ ,  $F_{P_{51}}$ ,  $F_{P_{52}}$ ,  $F_{P_{61}}$  and  $F_{P_{62}}$  the pressure forces acting on the surfaces of the solid-plug.

Once the active force  $F_5$  is known, the interface shear stress  $\hat{\sigma}$  in Figure 5 can similarly be obtained by the torque balance around the screw axis (Axis Y) and the force balance along the screw axis (Axis Z). In Figure 5, the torque balance around the screw axis (Y direction) is thus written as shown by Equation (7):

$$\begin{aligned}
 & -F_{FP_1}\cos\varphi_N \frac{D_{NS}}{2} + \hat{\sigma} b_N b \sin\alpha \frac{D_N}{2} - F_5 \sin\varphi_N \frac{D_{Nm}}{2} - F_{P_{51}} \sin\varphi_N \frac{D_{Nm}}{2} - F_{FP_{51}} \cos\varphi_N \frac{D_{Nm}}{2} + F_{P_{61}} \sin\varphi_N \frac{D_{Nm}}{2} \\
 & - F_{FP_{61}} \cos\varphi_N \frac{D_{Nm}}{2} = 0
 \end{aligned} \tag{7}$$

where  $\alpha$  is the angle between the direction of the interface shear stress  $\hat{\sigma}$  and the axial direction as shown in Figure 6 and the barrel channel diameter at barrel wall.

The equilibrium of forces on the solid-plug part embedded in the barrel channel along the screw axis (Axis Z) is:

$$-F_{FP1}\sin\varphi_N + \hat{\sigma}b_N b \cos\alpha + F_5 \cos\varphi_N - F_{P51}\cos\varphi_N - F_{FP51}\sin\varphi_N - F_{P61}\cos\varphi_N - F_{FP61}\sin\varphi_N = 0 \quad (8)$$

By substituting  $F_5$  in Equation (8) into Equation (7), the interface shear stress  $\hat{\sigma}$  amounts to:

$$\hat{\sigma} = \frac{\sqrt{F_{P1}^2 f_T^2 + F_5^2(1 + f_T^2) + 4F_{P51}^2 f_T^2 + 2F_{P1} F_5 f_T^2 + 4F_{P51} F_5 f_T^2 + 4F_{P1} F_{P51} f_T^2}}{b_N b} \quad (9)$$

### 3.3. Boundary conditions for positive conveying

In order to have the capacity of the positive conveying, the shear stress  $\hat{\sigma}$  must be less than the internal friction force per unit area at the interface between the part of the solid-plug embedded in the barrel channel and the rest in the screw channel so that the

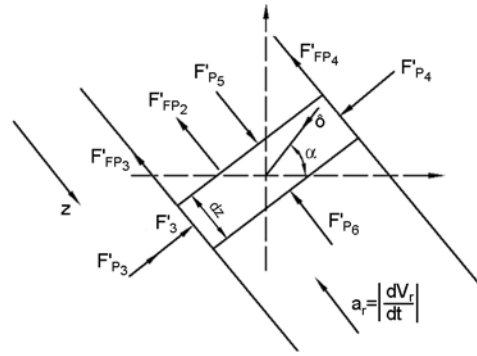


Figure 6. Motion and forces on the differential element in the screw channel

plug could move as a whole. Therefore, the first boundary condition equation is:

$$\hat{\sigma} \leq P f_i \quad (10)$$

Substituting Equation (9) into Equation (10), it becomes Equation (11):

$$\frac{\sqrt{F_{P1}^2 f_T^2 + F_5^2(1 + f_T^2) + 4F_{P51}^2 f_T^2 + 2F_{P1} F_5 f_T^2 + 4F_{P51} F_5 f_T^2 + 4F_{P1} F_{P51} f_T^2}}{b_N b} \leq P f_i \quad (11)$$

or

$$F_{P1}^2 f_T^2 + F_5^2(1 + f_T^2) + 4F_{P51}^2 f_T^2 + 2F_{P1} F_5 f_T^2 + 4F_{P51} F_5 f_T^2 + 4F_{P1} F_{P51} f_T^2 \leq (P b_N b f_i)^2 \quad (12)$$

When Equation (12) is divided by  $F_{P1}^2 f_T^2$ , the first boundary condition equation can approximately be simplified as follows:

$$\left(\frac{F_5}{F_{P1}}\right)^2 \left[1 + \frac{1}{f_T^2}\right] + \frac{F_5}{F_{P1}} \left[2 + 4\frac{F_{P51}}{F_{P1}}\right] + \left[2\frac{F_{P51}}{F_{P1}} + 1\right]^2 \leq \left(\frac{f_i}{f_T}\right)^2 \quad (13)$$

where  $f_i$  is internal friction coefficient in solids, and

$$\frac{F_5}{F_{P1}} = \frac{A_2}{A_1} + \frac{A_3}{A_1} + \frac{h}{b} \frac{A_4}{A_1} - \frac{h_N}{b_N} + \frac{h_N}{b_N} \frac{A_6}{A_1}$$

$$\frac{F_{P51}}{F_{P1}} = \frac{h_N}{b_N}$$

From Equation (13), it can be seen that the boundary condition is the function of the friction coefficients and structural parameters.  $h_N/b_N$  is defined as the barrel channel aspect ratio. It is known from

Equation (13) that the lower the friction coefficient of the barrel surface is, the easier the positive conveying can be achieved. More importantly, when the solid-plug is positively conveyed by the two active forces of the barrel and screw channel flights, the extruder has an operating mode where the solids conveying is independent of the friction coefficient on the barrel surface. Therefore, different friction coefficients on the barrel surface only induce different energy consumption and pressure peak at the end of the solids conveying zone and don't affect

the solids conveying process. If the friction coefficient on the barrel surface becomes nil, the solid-plug is also conveyed along the barrel channel helical angle. However, in the case of the friction-drag conveying, an effective solids conveying is dependent on a sufficient high friction coefficient on the barrel surface. The greater the friction coefficient of the barrel surface is, the steadier the friction-drag conveying is. As a result, higher energy consumption is required for the friction-drag conveying, compared to that in terms of the positive conveying.

### 3.4. Pressure equation

Continuity equation and kinematic equation are used to analyze the motion and forces of the differential element in the screw channel. The pressure equation in the solids conveying zone can be obtained after resolving the two equations.

A down-channel differential element is displayed in Figure 6, where  $z$  is the distance along the screw channel direction. The continuity equation is given by Equation (14):

$$\frac{\partial \rho}{\partial t} + V_r \frac{\partial \rho}{\partial z} + \rho \frac{\partial V_r}{\partial z} = 0 \quad (14)$$

Where the material density is varied along the screw channel, given by Equation (15) [26]:

$$\rho = \rho_m - (\rho_m - \rho_0)e^{-C_0 P} \quad (15)$$

Inserting Equation (15) into Equation (14), the continuity equation becomes Equation (16):

$$\frac{\partial P}{\partial t} + V_r \frac{\partial P}{\partial z} + \frac{1}{C_0} \left[ \frac{\rho_m e^{C_0 P}}{\rho_m - \rho_0} - 1 \right] \frac{\partial V_r}{\partial z} = 0 \quad (16)$$

where  $\rho$  is the density under pressure  $P$  at time  $t$ ,  $\rho_m$  the density under utmost pressure,  $\rho_0$  the bulk density under the atmospheric pressure and  $C_0$  a coefficient.

The kinematics equation can be determined by the application of the force balance to the differential element in Figure 6 in both the down-channel direction and the direction perpendicular to the screw channel.

The equilibrium of forces in the direction perpendicular to the screw channel is given by Equation (17):

$$F'_3 = \hat{\delta} \cos(\alpha - \varphi) b dz_b \quad (17)$$

The equilibrium of forces in the down-channel direction gives Equation (18):

$$F'_{FP2} + F'_{FP3} + F'_{FP4} + (F'_{P6} - F'_{P5}) - \hat{\delta} \sin(\alpha - \varphi) b dz_b = m' |a_r| \quad (18)$$

where  $m'$  is the mass of the differential element in the screw channel,  $F'_{P3}$ ,  $F'_{P4}$ ,  $F'_{P5}$ ,  $F'_{P6}$ ,  $F'_{FP2}$ ,  $F'_{FP3}$ ,  $F'_{FP4}$  the normal forces on the differential element in the screw channel and  $F'_3$  the active force on the differential element from the active flight of the screw.

Substituting Equation (17) into Equation (18) leads the kinematic equation to be expressed as shown by Equation (19):

$$\frac{\partial P}{\partial z} + PD_1 + \rho \left[ V_r^2 D_2 + D_3 \left( \frac{dV_r}{dt} \right) \right] = 0 \quad (19)$$

where  $D_i$  ( $i = 1, 2, 3$ ) are the parameters that are constant for a given barrel and screw as well as material.

The boundary conditions for the movement of solids are:

$$\begin{aligned} V_r(z,t)|_{z=0} &= V_0 = V_b \cos \varphi, & V_r(z,t)|_{t=0} &= V_0 \\ P(z,t)|_{z=0} &= P_0, & P(z,t)|_{t=0} &= \bar{P} \end{aligned}$$

where  $V_0$  is the inlet velocity of solids along the screw channel direction,  $P_0$  the inlet pressure and  $\bar{P}$  the average pressure.

Equations (16) and (19) are resolved using Laplace transformation, Laplace ultimate theory and dimensional transformation [27]. The pressure on the solid-plug along the screw channel direction can be written as shown by Equation (20):

$$P = P_0 \cdot e^{\frac{-\beta z}{L}} + \frac{\gamma^2 \rho_m V_0^2 D_2}{D_1} \cdot \left( e^{\frac{-\beta z}{L}} - 1 \right) \quad (20)$$

where  $\gamma$  is the modification factor,  $L$  the length of the barrel channel along the axial direction (Axis  $Z$ ) and

$$\beta = \frac{\rho_0 L D_1}{\rho_0 - \gamma^2 C_0 \rho_m V_0^2 D_3 (\rho_m - \rho_0)} D_1 = \frac{\sin \varphi \left( b_s f_L \frac{\sin \varphi_m}{\sin \varphi_s} + 2 f_L h \right) + \sin \varphi_m \left( b C_1 + b_s C_2 + h C_3 + \frac{b h_N C_5}{b_N} \right)}{b_m h [\sin \varphi + \sin \varphi_m C_4]}$$

$$D_2 = \frac{\sin\varphi}{\sin\varphi + \sin\varphi_m C_4} \left[ \frac{2\sin\varphi_m \left(1 + \frac{bh_N}{b_m h}\right) C_n (\sin\varphi \cot\varphi_N)^2}{D \sin\varphi} + \left( \frac{\sin\varphi_m \left(1 + \frac{bh_N}{b_m h}\right) C_k}{\sin\varphi} + f_L \right) \frac{4\cos\varphi \sin(\varphi_N + \varphi)}{D \sin\varphi_N} \right]$$

$$D_3 = \frac{\sin\varphi}{\sin\varphi + \sin\varphi_m C_4} \left[ 1 - \frac{\sin\varphi_m \left(1 + \frac{bh_N}{b_m h}\right) C_t}{\sin\varphi} \right]$$

$$C_1 = C_n = (f_L \cos\varphi + \sin\varphi) \left[ f_T \sin\varphi_N + \frac{A_2}{A_1} (f_T \sin\varphi_N - \cos\varphi_N) \right] + \left[ f_T \cos\varphi_N D_{NS} + \frac{A_2}{A_1} D_{Nm} (\sin\varphi_N + f_T \cos\varphi_N) \right] \frac{f_L \sin\varphi - \cos\varphi}{D_N}$$

$$C_2 = C_k = (f_L \cos\varphi + \sin\varphi) \frac{A_3}{A_1} (f_T \sin\varphi_N - \cos\varphi_N) + \frac{A_3}{A_1} D_{Nm} (\sin\varphi_N + f_T \cos\varphi_N) \frac{f_L \sin\varphi - \cos\varphi}{D_N}$$

$$C_3 = (f_L \cos\varphi + \sin\varphi) \frac{A_4}{A_1} (f_T \sin\varphi_N - \cos\varphi_N) + \frac{A_4}{A_1} D_{Nm} (\sin\varphi_N + f_T \cos\varphi_N) \frac{f_L \sin\varphi - \cos\varphi}{D_N}$$

$$C_4 = (f_L \cos\varphi + \sin\varphi) \frac{A_5}{A_1} (f_T \sin\varphi_N - \cos\varphi_N) + \frac{A_5}{A_1} D_{Nm} (\sin\varphi_N + f_T \cos\varphi_N) \frac{f_L \sin\varphi - \cos\varphi}{D_N}$$

$$C_5 = (f_L \cos\varphi + \sin\varphi) \left[ (\cos\varphi_N + f_T \sin\varphi_N) + \frac{A_6}{A_1} (f_T \sin\varphi_N - \cos\varphi_N) \right] + D_{Nm} \left[ (f_T \cos\varphi_N - \sin\varphi_N) + \frac{A_6}{A_1} (\sin\varphi_N + f_T \cos\varphi_N) \right] \frac{f_L \sin\varphi - \cos\varphi}{D_N}$$

$$C_t = (f_L \cos\varphi + \sin\varphi) \frac{A_7}{A_1} (\cos\varphi_N - f_T \sin\varphi_N) + \frac{A_7}{A_1} D_{Nm} (\sin\varphi_N + f_T \cos\varphi_N) \frac{f_L \sin\varphi - \cos\varphi}{D_N}$$

Equation (20) indicates that the pressure on the solids conveying zone is not only the function of the friction coefficients, material density and structural parameters, but also the function of the circumferential velocity. More importantly, it also discloses that the pressure can be well established along the screw channel direction when the inlet pressure is equal to zero, which can not be effectively explained by the Darnell-Mol theory.

In Equation (20), when the parameter  $\beta$  is larger than zero, the pressure is minus along the screw channel direction, which is no practical significance. If the parameter  $\beta$  is negative, the pressure is positive and can be built along the screw channel

direction. Therefore, the second boundary equation can be obtained and showed as Equation (21):

$$\beta = \frac{\rho_0 L D_1}{\rho_0 - \gamma^2 C_0 \rho_m V_0^2 D_3 (\rho_m - \rho_0)} < 0 \quad (21)$$

Equations (13) and (21) are used to determine whether the given parameters of the barrel channel and screw are good or not so that the optimal barrel channel and screw channel can be designed for larger positive conveying.

To summarize, the important components of the double-flight driving theory were established: two positive conveying boundary equations and the pressure equation in the solids conveying zone.



Sections 4 and 5 will present the experiments used to verify the double-flight driving theory with our extruder.

#### 4. Experimental

##### 4.1. Apparatus

One helically channeled extruder was specially designed and manufactured to study the positive conveying mechanism as shown in Figure 7. The extruder can be used to measure the pressure value on-line at the end of the solids conveying zone and the throughput that was only composed of the solids conveying zone and equipped with one detachable feeding barrel sleeve, one screw and one pressure-adjustable die. One taper barrel sleeve with two rows of small circular holes shown in Figure 8 is installed between the screw and diversion cone. Two rows of circular holes with their axis leaning to screw axis are evenly and alternately arranged along the circumferential direction. Their gross area is equal to the total area of the barrel channels and screw channel. While the extruder working, small circular holes are used as the outlets of the die for extruding solids so that solids pellets are extruded evenly in the peripheral direction. Therefore, the motion trace of the solids is approaching in the real case. The outlet area of the die is constant to make sure the steady extrusion.

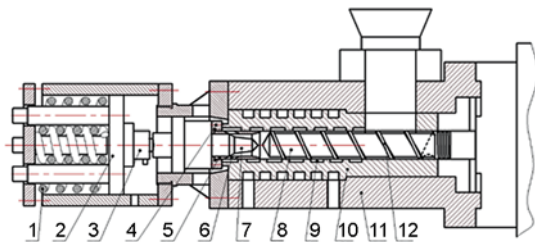


**Figure 7.** A schematic diagram of the extruder specially designed for the experiments. 1. spring, 2. spring bumper, 3. weighing sensor, 4. flange, 5. taper sleeve, 6. outlets, 7. diversion cone, 8. screw channel, 9. barrel channel, 10. feeding sleeve, 11. barrel, 12. screw.

Besides, in order to discuss the effects of the geometrical parameters on the positive conveying mechanism and the performance of the solids conveying zone, two helically channeled sleeves with different barrel channel widths and two screws with different pitches were made, as shown in Figure 9. The mean barrel channel helical angles are both  $50^\circ$  with eight barrel channels in the two helically channeled sleeves. The screws are of diameter 45 mm and

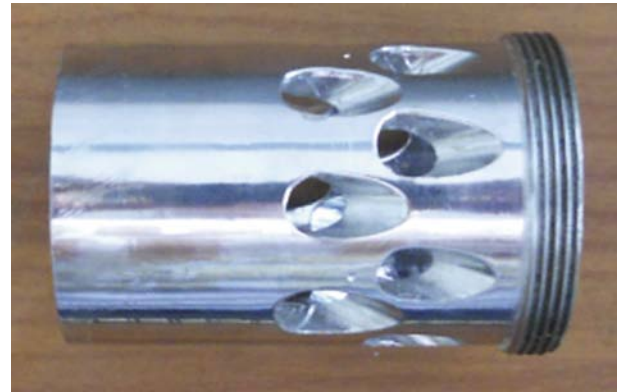


**Figure 8.** A taper sleeve with two rows of small circular holes



a)



b)

**Figure 9.** A schematic diagram of the feeding sleeves and screws. (a) two helically channeled sleeves with different barrel channel widths and one axially grooved sleeve, (b) two screws with different pitches.

**Table 1.** Geometrical parameters of the solids conveying zone of the experimental extruder

Experimental components	Thread number	Lead [mm]	Length [mm]	Barrel channel depth [mm]	Barrel channel width [mm]	Flight width [mm]
Sleeve <i>a</i>	8	From 180 to 156	261	2.0	From 8.5 to 7.7	5.5
Sleeve <i>b</i>	8	From 180 to 156	261	2.0	From 7.0 to 6.2	7.0
Sleeve <i>IKV</i>	8	–	261	1.5	8	9.6
Screw <i>c</i>	1	45	261	3.2	–	4.5
Screw <i>d</i>	1	From 45 to 39	261	3.2	–	4.5

**Table 2.** Physical properties of LDPE used in the experiments

Material	Melt flow index [g/10 min]	Bulk density [kg/m <sup>3</sup> ]	Density under utmost pressure [kg/m <sup>3</sup> ]	External friction coefficient ( $f_L = f_T$ )	Internal friction coefficient ( $f_i$ )	Mean diameter of particles [mm]
LDPE	7.5	485	920	0.13	0.45	1.6–2.0

have a length to diameter ratio of 5.8. In addition, the feeding sleeve *IKV* with axial grooves was also designed to compare the effects of the geometrical parameters on the solids conveying mechanism. The basic geometrical parameters of the experimental extruder are given in Table 1.

**4.2. Materials**

Low-density Polyethylene (LDPE, LD607 type) from Beijing Yanshan Plant was used with the physical properties listed in Table 2. In the experiments,

$$X_1 = \left(\frac{F_5}{F_{P1}}\right)^2 \left(1 + \frac{1}{f_T^2}\right) + \frac{F_5}{F_{P1}} \left(2 + 4\frac{F_{P51}}{F_{P1}}\right) + \left(2\frac{F_{P51}}{F_{P1}} + 1\right)^2 - \left(\frac{f_i}{f_T}\right)^2 = 0 \tag{22}$$

If  $\beta = 0$ , the second critical condition equation can be written as Equation (23):

$$X_2 = \frac{\rho_0 L D_1}{\rho_0 - \gamma^2 C_0 \rho_m V_0^2 D_3 (\rho_m - \rho_0)} = 0 \tag{23}$$

When the geometrical parameters of the screw, the physical parameters of material and the screw rotation are known, the unknown barrel channel aspect ratio  $h_N/b_N$  is resolved from Equations (22) and (23) as a function of the barrel channel helical angle. Thus, two critical curves can be drawn.

the friction coefficients were assumed to be constant.

**5. Results and discussions**

**5.1. Boundary conditions for positive conveying**

Two critical condition equations (Equation (22) and (23)) for the positive conveying can be obtained from the two boundary condition Equations (13) and (21).

When  $\delta = Pf_i$ , the first critical condition Equation can be determined as follows:

In order to compare with the experimental data directly, theoretical simulations are carried out using the same parameters in Table 1. The two critical curves for the given screw *c* and *d* and material can be drawn at the screw rotation speed of 40 rpm, shown in Figure 10. It can be seen that only when the values of the barrel channel aspect ratio and barrel channel helical angle are both simultaneously less than their corresponding critical points in the critical curves, the boundary condition Equations (13) and (21) can be both maintained. There-

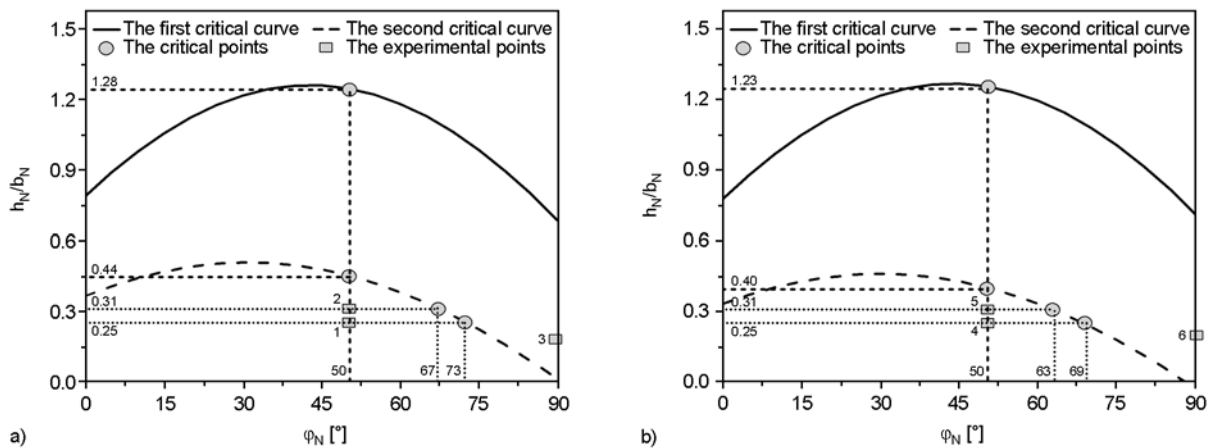


**Figure 10.** Predicted critical curves for positive conveying and experimental data. (a) the predicted critical curves and experimental values 1, 2 and 3 for the case with screw *c*, (b) the predicted critical curves and experimental values 4, 5 and 6 for the case with screw *d*. 1, 2, 3, 4, 5 and 6 are the experimental values for the combination *c-a* of the screw *c* and the feeding sleeve *a*, *c-b*, *c-IKV*, *d-a*, *d-b* and *d-IKV*.

fore, it can be concluded that, to have the capacity of the positive conveying, both the barrel channel aspect ratio and barrel channel helical angle must be beneath the two critical curves so that they are simultaneously less than their corresponding critical points. Otherwise, it is the friction-drag conveying. On the one hand, it can be seen from Figure 10a and 10b that the four experimental points 1 with the combination *c-a* of the screw *c* and the feeding sleeve *a*, 2 with *c-b*, 4 with *d-a* and 5 with *d-b* are all in the area beneath the two critical curves, which means that the positive conveying works in the four experiments. As for the experimental point 3 with the combination *c-IKV* of the screw *c* and the feeding sleeve *IKV*, and point 6 with *d-IKV*, they both fall out of the area beneath the two critical curves, so it is the friction-drag conveying in the two experiments. Positive conveying can be achieved in axial grooves only in the case of the minimum aspect ratio (zero), which has no practical significance. Thus, the feeding sleeve *IKV* with axial grooves can not achieve positive conveying in practice. On the other hand, it can be calculated by Equations (22) and (23) that the critical values of the barrel channel aspect ratio for the two experimental points 1 and 2 are 1.27 and 0.44 corresponding to the first and second critical curves respectively in Figure 10a while those for the two experimental points 4 and 5 are 1.23 and 0.4 respectively in Figure 10b with the given barrel channel helical angle of  $50^\circ$  in feeding sleeve *a* and *b*. Based on the theoretical analysis of two critical curves, the positive conveying can be achieved if the maximum values of the barrel channel aspect ratio are less than 0.44 in Figure 10a and 0.4 in Figure 10b with the given barrel channel helical angle of  $50^\circ$ . Otherwise, the friction-drag conveying works. Similarly, The maximum barrel channel helical angle in Figure 10a must be less than  $73^\circ$  for the point 1 to get positive conveying with the given value of the barrel channel aspect ratio of 0.25 in the feeding sleeve *a* and that is  $67^\circ$  for the point 2 with the given value of the barrel channel aspect ratio of 0.31 in the feeding sleeve *b*. Besides, the maximum barrel channel helical angle in Figure 10b must be less than  $69^\circ$  for the point 4 with the given value of the barrel channel aspect ratio of 0.25 in the feeding sleeve *a* and that is  $63^\circ$  for the point 5 with the given value of the barrel channel aspect ratio of 0.31 in the feeding sleeve *b*.

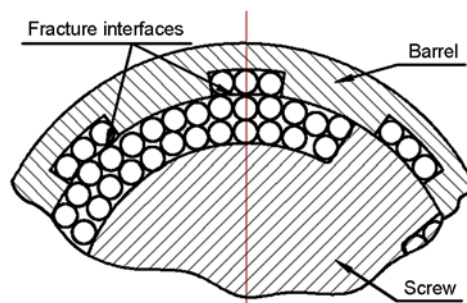
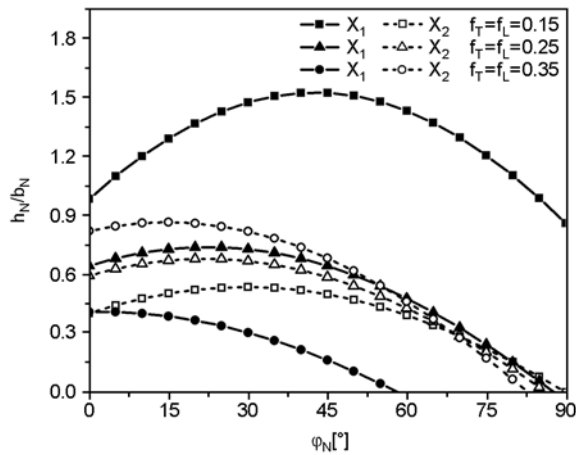


Figure 11. A schematic diagram of fracture interfaces inside the solid-plug

Therefore, the critical curves define such two characteristics in the positive conveying mechanism. One characteristic is that the maximum barrel channel helical angle can be determined when the barrel channel aspect ratio is known. It can be explained by the fact that the interface shear stress is raised remarkably with the increasing barrel channel helical angle. When the interface shear stress is bigger than the internal friction force, the solid-plug can be cut off at the interface as shown in Figure 11, and then the conveying is not the positive conveying. The other characteristic is that the maximum barrel channel aspect ratio also can be obtained when the barrel channel helical angle is given. It can be known from above theoretical studies that the friction forces from the barrel channel are the resistant forces and the active forces of the screw and barrel channel flight are the driving forces when the solid-plug in the barrel channel and screw channel is positively conveyed. However, it is worthwhile to mention that the active forces of the screw and barrel channel flight are both derived from the interface shear stress. Therefore, the deeper the barrel channel depth is, the greater the resistant force is. The wider the barrel channel width is, the greater the active force is. If the maximum barrel channel aspect ratio is exceeded, the active forces will not be enough so that the solid-plug will be cut off at the interface and there is no barrel channel conveyance. This is also the reason why the friction-drag conveying prevails in the experimental points 3 and 6. Thus, single screw extruders with the positive conveying can be designed by the two critical curves.

Figure 12 shows the theoretical simulations about the effects of different external friction coefficients on the critical curves using the same parameters as



**Figure 12.** Effect of different external friction coefficients on the critical curves

screw *c* at the screw rotation speed of 40 rpm at a constant internal friction coefficient of 0.6. It can be found from Figure 12 that different external friction coefficients lead to the variation of the two critical curves corresponding to different critical barrel channel aspect ratios and barrel channel helical angles. When the external friction coefficient increases, the location of the first critical curve descends while the location of the second critical curve ascends. Besides, it can also be seen that the greater the external friction coefficient is, the smaller the available area for positive conveying beneath the two critical curves is. It can be concluded that big external friction coefficients can result in the transformation from the positive con-



**Figure 13.** A whole solid-plug sample in a steady solids conveying process in the experimental extruder

veying to the friction-drag conveying, which is due to the fact that great friction coefficient of the barrel surface induces high resistance force for barrel channel conveyance in the positive conveying so that the solid-plug is cut off at barrel wall.

Figure 13 shows a whole solid-plug sample in a steady solids conveying process using the experimental extruder with the combination *c-a* at a screw rotation speed of 40 rpm. When the extruder runs steadily, we stop the screw suddenly to disassemble the pressure-adjustable die and to subsequently peel off the polymer sample located in the screw head. It can be seen from the sample in Figure 13 that the solids in the barrel channel and screw channel were extruded as a whole solid-plug indicating no internal circumferential shear fracture at the shear interface and the positive conveying prevailing. This experiment showed the typical positive conveying using the combination *c-a*, which is close to the predicted results from the point 1 in Figure 10a.

### 5.2. Pressure distribution

In order to verify the positive conveying mechanism further, some theoretical simulations about the effects of the geometrical parameters on the pressure distribution in the solids conveying zone were carried out at a screw rotation speed of 40 rpm. Moreover, the on-line measured results of experimental pressure were compared with theoretical analysis.

The pressure distribution curves in the solids conveying zone with different solids conveying mechanisms and external friction coefficients are presented in Figure 14. The first experiment was made using the combination *c-IKV* for the friction-drag conveying. The second experiment was carried out using the combination *c-a* for the positive conveying. It can be found from Figure 14 that the simulated pressure distribution in the friction-drag conveying by the Darnell-Mol theory increases sharply and is seriously deflected from the experimental data. The reason may be that the density of the solid-plug is assumed to be invariable and the acceleration of the solid-plug is not considered. In contrast, the simulated pressure distribution in the positive conveying by the present model increases linearly and is well consistent with the experimental data at the end of the solids conveying zone. This confirms that the double-flight driving theory can



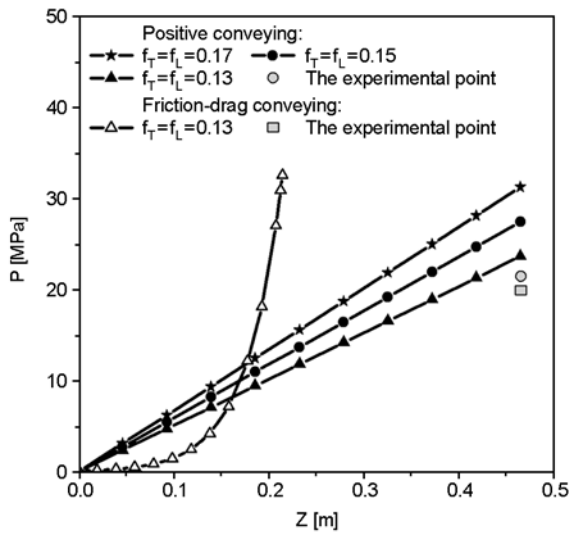


**Figure 14.** Pressure distribution in the solids conveying zone with different mechanisms and different friction coefficients

better describe the pressure distribution in the solids conveying zone than the Darnell-Mol theory. Besides, it is worthwhile to notice that the two experimental values in different solids conveying mechanisms are not obviously different indicating that both positive and friction-drag conveying mechanisms also have the good building pressure capability. In addition, it also can be seen that bigger external friction coefficients induce higher pressure increase in the solids conveying zone, which is consistent with researches of Fang *et al.* [28]. Effect of the barrel channel helical angle on the pressure value at the end of the solids conveying zone is shown in Figure 15. The experiment was performed with the combination *c-a*. The pressure value at the end of the solids conveying zone was

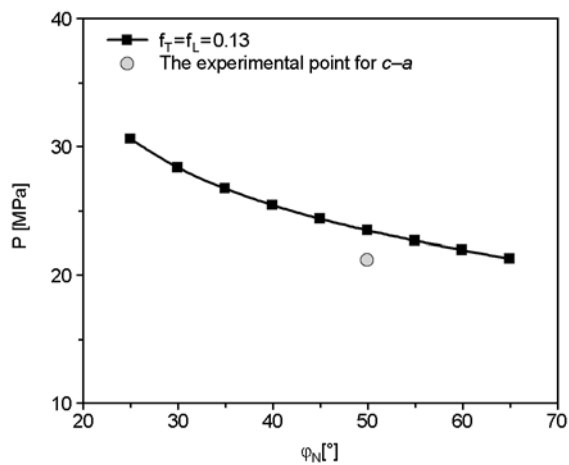


**Figure 15.** Effect of the barrel channel helical angle on the pressure value at the end of the solids conveying zone

found to decrease with the increasing barrel channel helical angle. In the case of the positive conveying, the conveying angle of the solid-plug in the screw channel is equal to the barrel channel helical angle. Thus, high barrel channel helical angle induces big conveying angle of the solid-plug in the screw channel, which improves the conveying rate of the solids in the screw channel resulting in low pressure value. In addition, it also can be known from the figure that the experimental value approaches to the theoretical data with the given external friction coefficient of 0.13, which confirms the accuracy of the theory.

Figure 16 displays the effect of the screw pitch on the pressure value at the end of the solids conveying zone, including the experimental data for the combinations *c-a* and *d-a*, respectively. It can be found that the simulated pressure value at the end of the solids conveying zone is raised with the increasing screw pitch size because the throughput in the screw channel is higher at a constant barrel channel conveying angle, which is helpful to compact solid-plug. The predicted values are consistent with the experimental data. However, such tendency is not that obvious at high barrel channel helical angle, which can be due to the fact that increasing barrel channel helical angle results in the decrease of the pressure value.

Figure 17 presents the predicted pressure value and experimental data at the end of the solids conveying zone for the combinations *c-a* and *c-b*. The simulated pressure values at the end of the solids conveying zone vary insignificantly with different barrel channel widths, as is consistent with the experimen-

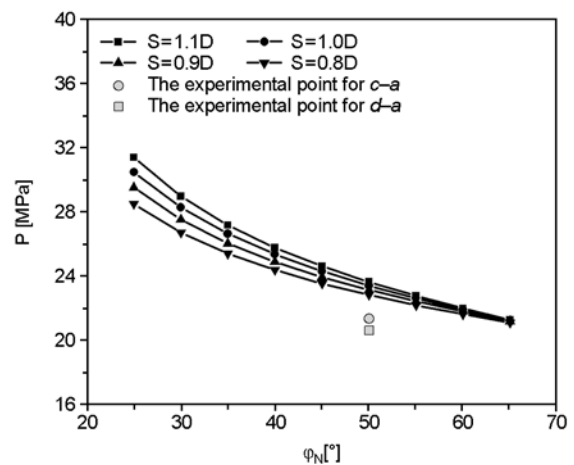


**Figure 16.** Effect of the screw pitch size on the pressure value at the end of the solids conveying zone

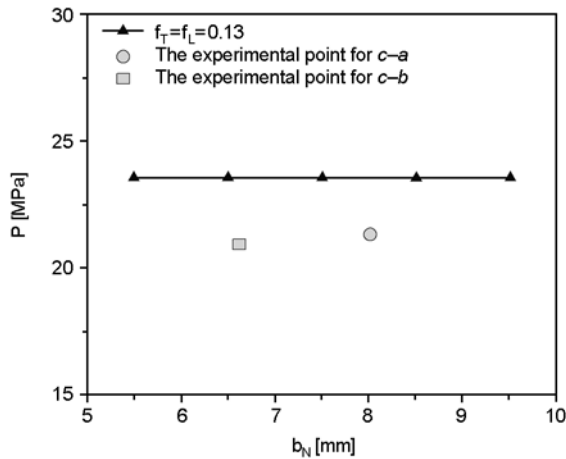


Figure 17. Effect of the barrel channel width on the pressure value at the end of the solids conveying zone

tal data. This can well be understood by comparing the difference between the double-flight driving theory and the Darnell-Mol theory. In the case of the friction-drag conveying, the barrel friction force is the active force and the mean friction coefficient of the barrel is raised greatly with the increasing barrel channel width by some previous reports [1–3, 13], which results in high pressure value at the end of the solids conveying zone. In contrast, all the friction forces from the barrel and screw surface are

$$m = n\pi\bar{D}_m \left[ \frac{\pi}{4}(D_{NS}^2 - D_S^2) - M\frac{e_1h}{\sin\varphi_m} - N\frac{e_2h_N}{\sin\varphi_N} \right] \frac{\sin\varphi\sin\varphi_N}{\sin(\varphi + \varphi_N)} \rho_0 \cdot 60 \quad (24)$$

where  $n$  is the screw rotation,  $\bar{D}_m$  the average diameter of the solid-plug,  $e_1$  and  $e_2$  the flight land width of the screw and barrel channel respectively, and  $M$  and  $N$  the thread numbers of the screw channel and barrel channel respectively.

Figure 18 describes the throughput measured and simulated for the combinations of *c-a*, *c-b* and *c-IKV*. It can be seen that the measured and simulated throughput data of the extrusion system are all improved greatly with the increasing screw rotation for the three combinations. The simulated throughput by the positive conveying mechanism for the combinations *c-a* and *c-b* are both close to the experimental values, which shows that the positive conveying mechanism is achieved during extrusion. Based on the positive conveying mechanism, greater barrel channel width induces larger barrel channel conveying square, which is consistent with the fact that the experimental throughput using the feeding

resistance forces in the double-flight driving theory for the positive conveying and the solid-plug is only pushed forward along the barrel channel helical angle by the two active flights of the barrel channel and screw. Therefore, the solids conveyance in the screw channel in the case of the positive conveying is hardly affected by the variation of the barrel channel width with a steady pressure value at the end of the solids conveying zone.

### 5.3. Throughput and energy consumption

According to above theoretical analysis on the positive conveying mechanism, the advantages of high throughput and low energy consumption can be revealed when one extruder works with the positive conveying. Experimental verifications for the positive conveying mechanism were also implemented from the view of throughput and energy consumption.

In the case of the positive conveying, the solids embedded in the barrel channel and screw channel as a whole plug are conveyed. Thus, taking the material velocity along the axial direction and the barrel channel and screw channel area around the screw axis into consideration, the total throughput  $m$  is given by Equation (24):

sleeve *a* with great barrel channel width is larger than that of the feeding sleeve *b* with small barrel channel width. Thus, the positive conveying mechanism is confirmed by the above experiments. In addition, it also can be seen that the measured

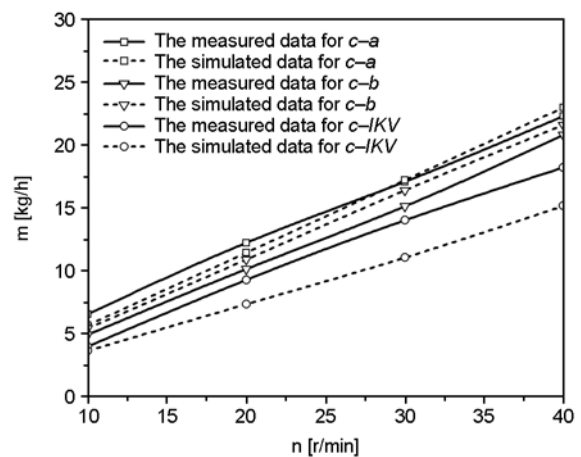


Figure 18. The measured and simulated throughput with the combinations *c-a*, *c-b* and *c-IKV*

**Table 3.** Experimental electric currents, total power and theoretically useful power at different screw rotations

n [r/min]	Combination <i>c-a</i>			Combination <i>c-b</i>			Combination <i>c-IKV</i>		
	Experimental data		Theoretical data by the present model	Experimental data		Theoretical data by the present model	Experimental data		Theoretical data by Darnel-Mol theory
	$I_1$ [A]	$P_{W1}$ [kW]	$P_{W11}$ [kW]	$I_2$ [A]	$P_{W2}$ [kW]	$P_{W22}$ [kW]	$I_3$ [A]	$P_{W3}$ [kW]	$P_{W33}$ [kW]
10	3.7	1.41	1.13	3.3	1.24	0.94	5.2	1.95	56.96
20	6.1	2.31	1.96	5.2	1.96	1.68	8.8	3.35	113.92
30	8.6	3.25	2.93	7.6	2.89	2.52	11.3	4.29	170.88
40	11.6	4.41	3.80	10.4	3.95	3.45	14.5	5.51	227.82

throughput with the combination *c-IKV* is less than those of the combinations *c-a* and *c-b*. This is because the solid-plug experiences fracture at barrel wall and the friction-drag conveying prevails during extrusion, which results in the decrease of the barrel channel conveyance. Besides, it is worth noticing that the simulated results for the combination *c-IKV* are seriously deflected from the measured results because only the solids in the screw channel are considered and those in the barrel channel are neglected when the friction-drag conveying prevailing in the Darnell-Mol theory.

The experimental electric currents, total power and theoretically useful power at different screw rotations for the three combinations *c-a*, *c-b* and *c-IKV* are listed in Table 3.

$I_1$ ,  $I_2$  and  $I_3$  are the experimental electric currents for the three combinations *c-a*, *c-b* and *c-IKV* respectively and  $P_{W1}$ ,  $P_{W2}$  and  $P_{W3}$  are the total power corresponding to  $I_1$ ,  $I_2$  and  $I_3$ .  $P_{W11}$  and  $P_{W22}$  are the theoretically useful power for the combinations *c-a* and *c-b* by the positive conveying theory and  $P_{W33}$  the theoretically useful power for the combination of *c-IKV* by the Darnell-Mol theory.

The variation of the electric current reflects the change of the total power in the motor because the total power of a three-phase induction motor is proportional to the electric current. In the present model for the combinations *c-a* and *c-b*, only the useful power of  $P_{W11}$  and  $P_{W22}$  for solids conveyance are calculated. That results in the theoretical data less than the experimental data of  $P_{W1}$  and  $P_{W2}$ , respectively. It can be noticed that because the deviation between the experimental and theoretical data still keeps in a small range with the increase of the screw rotation, the experimental data shows the actual energy consumption indicating that the positive conveying mechanism works during extrusion.

In addition, the comparison of  $P_{W11}$  and  $P_{W22}$  also shows that the simulated useful power in the positive conveying mechanism is enhanced with the increasing barrel channel width for the combinations *c-a* and *c-b*, which can also be explained by the fact that the active forces of the barrel channel and screw flight are improved with the increase of the barrel channel width resulting in higher friction heat on the active flights of the barrel channel and screw. It also can be seen that the experimental value of the total power for the combination *c-IKV* with friction-drag conveying is remarkably higher than those for the combinations *c-a* and *c-b* with positive conveying. This may be due to that the solid-plug in the barrel channel and screw channel experiences fracture at barrel wall for the combination *c-IKV* when the friction-drag conveying mechanism prevails during extrusion resulting in high friction heat. From Table 3, it also can be found that the theoretical value of  $P_{W33}$  for the combination *c-IKV* is much greater than the experimental value due to the high pressure value predicted by the Darnell-Mol theory.

## 6. Conclusions

A solids conveying theory called double-flight driving theory was proposed for helically channeled single screw extruders where the solids embedded in the barrel channel and screw channel behaving as a whole solid-plug were pushed forward along the barrel channel helical angle direction by active flights of the barrel channel and screw. In order to achieve positive conveying in the double-flight driving theory, two boundary conditions for the positive conveying were determined by analyzing force equations and pressure equation. On the basis of the theoretical and experimental studies on the helically channeled feed zone, the positive convey-

ing mechanism was confirmed by the results measured and simulated by our theory.

From the boundary condition equations, the maximum barrel channel helical angle could be determined with a given barrel channel aspect ratio. Vice Versa, the maximum barrel channel aspect ratio also could be obtained with a given barrel channel helical angle for positive conveying. The external friction coefficients determine if the conveying is the positive conveying or the friction-drag conveying. More importantly, an extruder with the positive conveying can be designed from the analysis of boundary condition equations.

Compared with the sharp increase of the pressure value in the friction-drag conveying theory of the Darnel-Mol Model, the pressure distribution in the positive conveying increases linearly. In addition, the pressure value at the end of the solids conveying zone in the positive conveying is higher at lower barrel channel helical angle, higher external friction coefficients and larger screw pitch size. However, the effect of the barrel channel width is not significant. Therefore, the ability to build pressure in the solids conveying zone can be effectively controlled. The extruder designed on the positive conveying mechanism showed higher throughput and lower energy consumption than that on the friction-drag conveying mechanism. Besides, bigger barrel channel width is helpful to obtain a steady solids conveying and high throughput in the case of the positive conveying.

### Acknowledgements

The authors would like to acknowledge the support of the National Natural Science Foundation of China (No. 50873014).

### Nomenclature

$X$  radial direction  
 $Y$  tangential direction  
 $Z$  axial direction  
 $z$  distance along screw channel direction  
 $V_b$  circumferential velocity of barrel  
 $V_S$  velocity along barrel channel direction in positive conveying  
 $V_r$  velocity along screw channel direction in positive conveying  
 $V_{Sf}$  velocity along barrel channel direction in friction-drag conveying

$V_{rf}$  velocity along screw channel direction in friction-drag conveying  
 $V_0$  inlet velocity of solids along screw channel direction  
 $n$  screw rotation  
 $a_n$  normal acceleration  
 $a_k$  coriolis acceleration  
 $a_r$  relative acceleration  
 $I_n, I_k, I_r$  inertia forces  
 $P, P_1, P_2, P_3, P_4, P_{51}, P_{52}, P_{61}, P_{62}$  pressure  
 $P_0$  inlet pressure  
 $\bar{P}$  average pressure  
 $F_{P_1}, F_{P_2}, F_{P_3}, F_{P_4}, F_{P_{51}}, F_{P_{52}}, F_{P_{61}}, F_{P_{62}}$  normal forces on the solid-plug resulting from pressure  
 $F_{FP_1}, F_{FP_2}, F_{FP_3}, F_{FP_4}, F_{FP_{51}}, F_{FP_{61}}$  normal forces on the solid-plug resulting from friction  
 $F_3$  active force on solid-plug from active flight of screw  
 $F_5$  active force on solid-plug from active flight of barrel channel  
 $F'_{P_3}, F'_{P_4}, F'_{P_5}, F'_{P_6}$  normal forces on differential element in screw channel resulting from pressure  
 $F'_{FP_2}, F'_{FP_3}, F'_{FP_4}$  normal forces on differential element in screw channel resulting from friction  
 $F'_3$  active force on differential element from active flight of screw  
 $\hat{\sigma}$  interface shear stress between part of solid-plug in barrel channel and the rest in screw channel  
 $A_i (i = 1, 2, 3, 4, 5, 6, 7)$  parameters that are constant for given barrel and screw as well as material  
 $D_i (i = 1, 2, 3)$  parameters that are constant for given barrel and screw as well as material  
 $f_T$  friction coefficient of solids on barrel  
 $f_L$  friction coefficient of solids on screw  
 $f_i$  internal friction coefficient in solids  
 $t$  time  
 $\rho$  density at pressure  $P$  at time  $t$   
 $\rho_m$  density at utmost pressure  
 $\rho_0$  bulk density at atmospheric pressure  
 $C_0$  coefficient of material



$\alpha$	angle between direction of interface shear stress and axial direction
$\gamma$	modification factor
$L$	length of barrel channel along axial direction
$D_N$	barrel channel diameter at barrel wall
$D_{NS}$	barrel channel root diameter
$D_{Nm}$	mean barrel channel diameter
$D$	outer diameter of screw
$D_S$	screw root diameter
$D_m$	mean screw diameter
$\bar{D}_m$	average diameter of the solid-plug
$b_N$	barrel channel width
$b$	screw channel width at barrel wall
$b_S$	screw channel width at screw root
$b_m$	mean screw channel width
$h_N$	barrel channel depth
$h$	screw channel depth
$\varphi_N$	barrel channel helical angle
$\varphi$	screw channel helical angle at barrel wall
$\varphi_S$	screw channel helical angle at screw root
$\varphi_m$	mean screw channel helical angle
$e_1$	flight land width of screw
$e_2$	flight land width of barrel channel
$M$	thread numbers of screw channel
$N$	thread numbers of barrel channel
$m$	total throughput in solids conveying zone
$m'$	mass of differential element in screw channel in Figure 6
$I_i$ ( $i = 1, 2, 3$ )	experimental electric current
$P_{W_i}$ ( $i = 1, 2, 3$ )	total power
$P_{W_{ii}}$ ( $i = 1, 2, 3$ )	theoretically useful power

## References

- [1] Rautenbach R.: Model tests on the transport of plastics powders in the feed section of single-screw extruders. *Kunststoffe-German Plastics*, **69**, 377–380 (1979).
- [2] Grünschloß E.: Calculation of the mean coefficient of barrel friction in grooved feed sections. *Kunststoffe-German Plastics*, **74**, 405–409 (1984).
- [3] Potente H.: Methods of calculating grooved extruder feed sections. *Kunststoffe-German Plastics*, **75**, 439–441 (1985).
- [4] Franzkoch B., Menges G.: Grooved forced-feeding zones can improve extruder performance. *Plastics Engineering*, **34**, 51–54 (1978).
- [5] Rautenbach R., Peiffer H.: Throughput and torque characteristics of grooved feed sections in single-screw extruders. *Kunststoffe-German Plastics*, **72**, 262–266 (1982).
- [6] Davis B. A., Gramann P. J., Del P. Noriega E. M., Osswald T. A.: Grooved feed single screw extruders – Improving productivity and reducing viscous heating effects. *Polymer Engineering and Science*, **38**, 1199–1204 (1998). DOI: [10.1002/pen.10288](https://doi.org/10.1002/pen.10288)
- [7] Menges G., Feistkorn W., Fischbach G.: Hot-operated grooved bushes increase the output and reduce the energy consumption of single screw extruders. *Kunststoffe-German Plastics*, **74**, 695–699 (1984).
- [8] Grünschloß E.: Process improvements in single-screw extruders with grooved feed sections. *Kunststoffe-German Plastics*, **75**, 850–854 (1985).
- [9] Schuele H., Fritz H. G.: Minimizing the abrasive wear in the feed zone of grooved barrel extruders. *Kunststoffe-German Plastics*, **77**, 387–393 (1987).
- [10] Kramer A.: Experience in using extruders with grooved feed zones. *Kunststoffe-German Plastics*, **78**, 21–26 (1988).
- [11] Grünschloß E.: A new style single screw extruder with improved plastification and output power. *International Polymer Processing*, **17**, 291–300 (2002).
- [12] Grünschloß E.: A powerful universal plasticating system for single-screw-extruders and injection-moulding machines. *International Polymer Processing*, **18**, 226–234 (2003).
- [13] Miethlinger J.: Modelling the solids feed section in grooved-feed extruders. *Kunststoffe Plast Europe*, **93**, 49–53 (2003).
- [14] Rauwendaal C., Sikora J.: The adjustable grooved feed extruder. *Plastics Additives and Compounding*, **2**, 26–30 (2000). DOI: [10.1016/S1464-391X\(00\)88882-0](https://doi.org/10.1016/S1464-391X(00)88882-0)
- [15] Kowalska B.: Grooved feed sections: Design variants for single-screw extruders. *Kunststoffe Plast Europe*, **90**, 10–11 (2000).
- [16] Sikora J. W.: The effect of the feed section groove taper angle on the performance of a single-screw extruder. *Polymer Engineering and Science*, **41**, 1636–1643 (2001). DOI: [10.1002/pen.10861](https://doi.org/10.1002/pen.10861)
- [17] Rautenbach R., Peiffer H.: Model calculation for the design of the grooved feed section of single-screw extruders. *Kunststoffe-German Plastics*, **72**, 137–143 (1982).
- [18] Potente H.: The forced feed extruder must be reconsidered. *Kunststoffe-German Plastics*, **78**, 355–363 (1988).
- [19] Potente H., Schöppner V.: A throughput model for grooved bush extruders. *International Polymer Processing*, **10**, 289–295 (1995).
- [20] Rauwendaal C.: *Polymer extrusion*. Hanser, Munich (2010).

- [21] Potente H., Phol T. C.: Polymer pellet flow out of the hopper into the first section of a single screw. *International Polymer Processing*, **17**, 11–21 (2001).
- [22] Moysey P. A., Thompson M. R.: Investigation of solids transport in a single-screw extruder using a 3-D discrete particle simulation. *Polymer Engineering and Science*, **44**, 2203–2215 (2004).  
DOI: [10.1002/pen.20248](https://doi.org/10.1002/pen.20248)
- [23] Moysey P. A., Thompson M. R.: Modelling the solids inflow and solids conveying of single-screw extruders using the discrete element method. *Powder Technology*, **153**, 95–107 (2005).  
DOI: [10.1016/j.powtec.2005.03.001](https://doi.org/10.1016/j.powtec.2005.03.001)
- [24] Moysey P. A., Thompson M. R.: Determining the collision properties of semi-crystalline and amorphous thermoplastics for DEM simulations of solids transport in an extruder. *Chemical Engineering Science*, **62**, 3699–3709 (2007).  
DOI: [10.1016/j.ces.2007.03.033](https://doi.org/10.1016/j.ces.2007.03.033)
- [25] Michelangelli O. P., Yamanoi M., Gaspar-Cunha A., Covas J. A.: Modelling pellet flow in single extrusion with DEM. *Journal of Process Mechanical Engineering*, **225**, 255–268 (2011).  
DOI: [10.1177/0954408911418159](https://doi.org/10.1177/0954408911418159)
- [26] Chung C. I.: Plasticating single-screw extrusion theory. *Polymer Engineering and Science*, **11**, 93–98 (1971).  
DOI: [10.1002/pen.760110204](https://doi.org/10.1002/pen.760110204)
- [27] Qu J., Shi B., Feng Y., He H.: Dependence of solids conveying on screw axial vibration in single screw extruders. *Journal of Applied Polymer Science*, **102**, 2998–3007 (2006).  
DOI: [10.1002/app.24658](https://doi.org/10.1002/app.24658)
- [28] Fang S., Chen L., Zhu F.: Studies on the theory of single screw plasticating extrusion. Part II: Non-plug flow solid conveying. *Polymer Engineering and Science*, **31**, 1117–1122 (1991).  
DOI: [10.1002/pen.760311508](https://doi.org/10.1002/pen.760311508)

# Structure-properties relationships of polyhedral oligomeric silsesquioxane (POSS) filled PS nanocomposites

N. Tz. Dintcheva<sup>1\*</sup>, E. Morici<sup>1</sup>, R. Arrigo<sup>1</sup>, F. P. La Mantia<sup>1</sup>, V. Malatesta<sup>2</sup>, J. J. Schwab<sup>3</sup>

<sup>1</sup>Dipartimento di Ingegneria Chimica, Gestionale, Informatica, Meccanica, Università di Palermo, Viale delle Scienze, ed.6, 90128 Palermo, Italy

<sup>2</sup>Materials Science Department, Università Milano Bicocca, Via R. Cozzi 53, 20125 Milano, Italy

<sup>3</sup>Hybrid Plastics, 55 WL Runnels Industrial Dr., MS 39401 Hattiesburg, USA

Received 23 November 2011; accepted in revised form 20 January 2012

**Abstract.** The polyhedral oligomeric silsesquioxane (POSS) additivated polystyrene (PS) based nanocomposites were prepared by melt processing and the structure-properties relationships of the POSS-PS systems were compared to those of the neat PS. In order to investigate the effect of these structural parameters on the final properties of the polymer nanocomposites, five different kinds of POSS samples were used, in particular, POSS with different inorganic cage and with different organic pendent groups. The rheological investigation suggests clearly that the POSS acts as a plasticizer and that the processability of the PS was positively modified. The affinity between the POSS samples and the PS matrix was estimated by the calculated theoretical solubility parameters, considering the Hoy's method and by morphology analysis. Minor difference between the solubility parameter of POSS and the matrix means better compatibility and no aggregation tendency. Furthermore, the POSS loading leads to a decrease of the rigidity, of the glass transition temperature and of the damping factor of the nanocomposite systems. The loading of different POSS molecules with open cage leads to a more pronounced effect on all the investigated properties than the loading of the POSS molecules with closed cage. Moreover, the melt properties are significantly influenced by the type of inorganic framework, by the type of the pendent organic groups and by the interaction between the POSS organic groups and the host matrix, while, the solid state properties appear to be influenced more by the kind of cage.

**Keywords:** nanocomposites, POSS structure, polystyrene matrix, structure-properties relationships

## 1. Introduction

The formulation of high-performance polymer based nanocomposites, e.g. improved stiffness, dimensional stability, barrier properties, fire retardancy, is a very promising and challenging issue from scientific and industrial point of view. The formation of dispersed nanoparticles in polymeric matrices offers unique opportunities for designing advanced structural and functional materials. A small amount of the 1–5 wt% of nanoparticles in polymer resin gives a significant improvement in properties of the unfilled resin and these improvements are compara-

ble to those obtained using 25–40 wt% microscopic size particles in traditional composite formulations [1–5].

Polyhedral oligosilsesquioxane, so-called POSS, is a class of organosilicic three-dimensional compounds with cage frameworks with different degrees of symmetry and their general formula is  $(\text{RSiO}_{1.5})_n$ , where  $n$  is an integer number and R is an organic group. The organic pendent groups can be designed to achieve the desired affinity with the host polymeric matrix [1, 2]. Using POSS in polymer based nanocomposites is a promising issue for the design

\*Corresponding author, e-mail: [nadka.dintcheva@unipa.it](mailto:nadka.dintcheva@unipa.it)

of materials with high-performance in several applications [6–20] such as low-dielectric applications [6], biomaterials for cardiovascular [14] and dental implants [16], organic solar cells [17], flame resistant nanocomposites [18, 19], optical limiting [20], etc.

An important feature of the POSS formulation is their one-pot preparation, i.e. the cage formation and apex group functionalization occur simultaneously. The formation and functionalization at the same time allows preparation of POSS molecules with controlled and constant structure in contrast to the clay and silica nanoparticles, where the modification is made post-synthesis by ion-exchange reaction in a second step. The easier functionalization of the POSS molecules allows a controlled chemical reaction between the f-POSS and the different functional groups present in the polymer matrix [11, 12]. A recent review addressing the physical properties of POSS polymer based materials and their biomedical applications evidences the needed and desirable characteristics of POSS molecules, i.e. non-toxicity and bio-stability. Bio-stability is indeed, one of the most important consideration for the selection of polymer based composites for medical applications [14].

The POSS loading leads to the improvement of the thermal and mechanical properties comparing to the neat polymer resin [13, 15]. Furthermore, a few scientific papers report interesting results on the rheology modification of the POSS-additivated polymer-based systems, i.e. the POSS loading decreases the matrix shear viscosity [21, 22]. Moreover, a prolonged thermal treatment of the POSS polymer-based systems, results in migration of POSS molecules to the polymer matrix surface and to the formation of a thin protective POSS rich charred layer [19].

The fundamental understanding of the structure-properties relationships is of utmost importance when developing further applications of the POSS molecules as nanofillers in conventional polymer matrices.

In this paper, the structure-property relationships in POSS filled PS nanocomposites were investigated, the different behaviour of POSS samples with open and closed cage and also with different organic pendent groups were considered. The rheological, mechanical, dynamic-mechanical, thermal and mor-

phological analysis of the POSS-PS nanocomposites were evaluated and their properties were compared with those of the neat polystyrene resin. The theoretical calculated solubility parameters of the POSS were compared to the solubility parameter of the PS sample, in order to better understand the nanocomposite properties in molten and solid states. All of the obtained results suggest that the POSS acts as plasticizer. The efficiency of the plasticizing action, investigated in this work, has been found to significantly depend on the kind of the inorganic framework and on the chemical nature and length of the pendent organic groups.

## 2. Experimental

### 2.1. Materials

The materials used in this work are:

- Polystyrene (PS) produced by IneosNova (USA) under the name of ‘Empera 251N’; volume melt flow rate 2.4 cm<sup>3</sup>/10 min at 200°C and 5 kg load;
- five different polyhedral oligomeric silsesquioxane (POSS) samples, which the structure, molecular weight and chemical formulas are reported in Table 1 (POSS<sup>®</sup> structures are reported as in Hybrid Plastic Ltd catalogue).

In Table 1, the composition of all the PS based nanocomposites are reported.

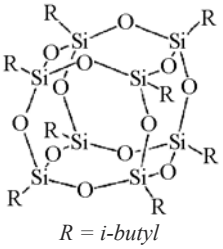
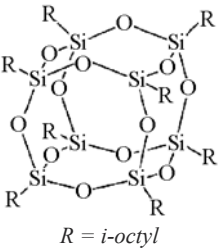
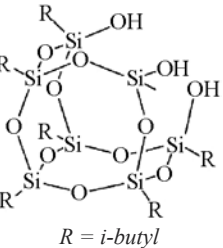
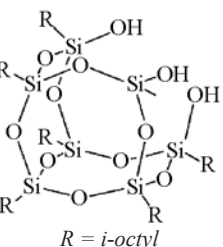
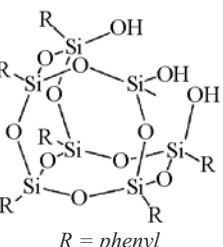
### 2.2. Preparation and characterization

The preparation of POSS-PS systems was carried out using a Brabender mixer at  $T = 170^{\circ}\text{C}$  and mixing speed 50 rpm for 5 minutes. Neat polystyrene was subjected to the same processing.

The rheological characterization, including measurements of the complex viscosity parameters,  $G'$  and  $G''$ , was performed by using a Rheometric Scientific (USA) RDA II plate-plate rotational rheometer, operating at  $T = 170^{\circ}\text{C}$  and a 5% strain deformation. The storage modulus  $G'$  as a function of the temperature was evaluated in the temperature-sweep modules using strain at 1% and frequency at 1 Hz. Mechanical tests of rectangular samples cut from compression moulded sheet (sheet thickness about 100  $\mu\text{m}$ ) were carried out using a universal Instron machine mod 1122, according to ASTM D882 (crosshead speed of 100 mm/min). The average values of the elastic modulus ( $E$ ), tensile strength ( $TS$ ) and elongation at break ( $EB$ ) were calculated. The reproducibility of the results was about  $\pm 5\%$ .



**Table 1.** Structure, molecular weight and chemical formula of POSS samples (as reported in the Hybrid Plastics catalogue), sample code and composition of PS based nanocomposites

Structure, molecular weight and chemical formula of POSS <sup>®</sup> , (as reported in the Hybrid Plastic catalogue)	Sample code	Composition
<p><i>IB-POSS</i></p>  <p><math>C_{32}H_{72}O_{12}Si_8</math> 873.60 g/mol</p> <p><b>IB-PS</b></p> <p><b>PS + 5 wt% IB-POSS</b></p>		
<p><i>IO-POSS</i></p>  <p><math>(C_8H_{17})_n (SiO_{1.5})_n</math> (cage mixture) 1322.46 g/mol</p> <p><b>IO-PS</b></p> <p><b>PS + 5 wt% IO-POSS</b></p>		
<p><i>TSIB-POSS</i></p>  <p><math>C_{28}H_{66}O_{12}Si_7</math> 791.42 g/mol</p> <p><b>TSIB-PS</b></p> <p><b>PS + 5 wt% TSIB-POSS</b></p>		
<p><i>TSIO-POSS</i></p>  <p><math>C_{56}H_{122}O_{12}Si_7</math> 1184.16 g/mol</p> <p><b>TSIO-PS</b></p> <p><b>PS + 5 wt% TSIO-POSS</b></p>		
<p><i>TSPH-POSS</i></p>  <p><math>C_{42}H_{38}O_{12}Si_7</math> 931.34 g/mol</p> <p><b>TSPH-PS</b></p> <p><b>PS + 5 wt% TSPH-POSS</b></p>		

Dynamic Mechanical Thermal Analysis (DMTA) was performed using a Rheometrics DMTA V instrument, single cantilever bending method. The test has been carried out in the temperature swift mode, between 25 and 150°C at a heating rate of

2 °C/min. The frequency was set to 1 Hz and the maximum strain amplitude was 0.5%. The storage modulus ( $E'$ ) and loss factor ( $\tan \delta$ ) as a function of the temperature were recorded.

The calorimetric data were evaluated by differential scanning calorimetry (DSC), using a Perkin-Elmer DSC7 calorimeter, at scanning rate of 10°C/min. Scanning Electron Microscopy, SEM, analysis was performed on nitrogen-fractured radial surfaces of all the investigated samples by a Philips (Netherlands) ESEM XL30 equipment.

### 3. Results and discussion

#### 3.1. Theoretical solubility parameter ( $\delta_{\text{tot}}$ )

The theoretical solubility parameter of the pristine PS and different POSS molecules were calculated considering the Hoy's method [23], as follows:

<b>Expressions for <math>\delta</math> and <math>\delta</math>-components</b>	$\delta_{\text{tot}} = \frac{\mathbf{F}_i + \frac{B}{\bar{n}}}{V}$ $B = 277$ $\delta_p = \delta_{\text{tot}} \left[ \frac{1}{\alpha^{(P)}} \cdot \frac{\mathbf{F}_p}{\mathbf{F}_i + \frac{B}{\bar{n}}} \right]^{1/2}$ $\delta_h = \delta_{\text{tot}} \left[ \frac{\alpha^{(P)} - 1}{\alpha^{(P)}} \right]^{1/2}$ $\delta_d = (\delta_{\text{tot}}^2 - \delta_p^2 - \delta_h^2)^{1/2}$
<b>Additive molar functions</b>	$\mathbf{F}_i = \sum N_i \mathbf{F}_{i,i}$ $\mathbf{F}_p = \sum N_i \mathbf{F}_{p,i}$ $V = \sum N_i V_i$ $\Delta_{T_i}^{(P)} = \sum N_i \Delta_{T_i}^{(P)}$
<b>Auxiliary equations</b>	$\alpha^{(P)} = \frac{777 \Delta_{T_i}^{(P)}}{V}$ $n = \frac{0.5}{\Delta_{T_i}^{(P)}}$

where:

$\mathbf{F}_i$  is the molar attraction function and  $\mathbf{F}_p$  its polar contribution;

$V$  is the molar volume of the solvent molecule or the structural unit of the polymer;

$\Delta_T$  is the Lyndersen correction for non-ideality,  $\alpha$  is the molecular aggregation number;

$n$  is the number of repeating units per effective chain segment of the polymer;

$\delta_{\text{tot}}$  is the solubility parameter;

$\delta_p$  is the contribution of the polar forces;

$\delta_h$  is the contribution of the hydrogen bonding;

$\delta_d$  is the contribution of the dispersion forces.

In Table 2, the calculated theoretical solubility parameter values are reported. In general a smaller difference between the solubility parameters of POSS sample and that of the matrix means better compatibility. The theoretical calculated value of the solubility parameter of PS is closer to the values of TSIB-POSS (Table 1), while, the closed cage, IB and IO-POSS have higher calculated solubility parameters. Moreover, the solubility parameter component ( $\delta_p$ ) that is related to the contribution of the polar forces and its differences compared to the PS are also reported in the Table 2. In order to ensure better solubility of POSS into the matrix it is necessary to match the polarity of the POSS vertex groups to that of the matrix polymer. Interestingly no solubility parameter component ( $\delta_p$ ) related to the contribution of the polar forces for IB and IO-POSS systems was found. Therefore, the type and polarity of the organic pendent group (R) facilitate and control the POSS dispersion into the polymeric matrix. Additionally the organic groups are able to exert a shielding effect of the POSS inorganic framework, i.e. the interaction between the matrix macromolecules and the POSS inorganic core is much less pronounced the longer organic groups. The calculated values of  $|\Delta\delta|_{\text{tot}}$  and  $|\Delta\delta|_p$  for TSIB-POSS are minor and considering the length and chemical nature of its pendent organic groups, this POSS samples shows, from a theoretical point of view, the best solubility into the polar polystyrene

**Table 2.** Values of theoretical calculated solubility parameters of PS and POSS

Sample	$\delta_{\text{tot}}$ [J/cm <sup>3</sup> ] <sup>1/2</sup> (a)	$ \Delta\delta _{\text{tot}} =  \delta_{\text{tot PS}} - \delta_{\text{tot POSS}} $ [J/cm <sup>3</sup> ] <sup>1/2</sup>	$\delta_p$ [J/cm <sup>3</sup> ] <sup>1/2</sup>	$ \Delta\delta _p =  \delta_p \text{ PS}  -  \delta_p \text{ POSS} $ [J/cm <sup>3</sup> ] <sup>1/2</sup>
PS	19.35	—	8.25	—
IB-POSS	16.05	3.30	0	8.25
IO-POSS	16.05	3.30	0	8.25
TSIB-POSS	18.01	1.34	7.17	1.08
TSIO-POSS	17.12	2.23	4.80	3.45
TSPH-POSS	21.23	1.88	12.53	4.28

(a) Calculated by Hoy's equation

matrix and tendency to aggregate less than other POSS samples.

### 3.2. Rheological analysis

In Figures 1a–d, the flow curves and the moduli  $G'$  and  $G''$  of pristine PS and POSS additivated PS are reported. The viscosity values in the whole investigated frequency region of all the POSS additivated samples are lower than the those of the pristine polystyrene. In Figures 1b–c the flow curve of closed and open cage POSS additivated PS are shown separately. Similar trends were observed also for the moduli  $G'$  and  $G''$ , as seen in Figure 1d. It is interesting to highlight that the open cage POSS additivated samples show a slightly pronounced decreases of the viscosity and of the moduli in the whole investigated frequency region, compared to the values of the sample additivated with closed cage POSS. Moreover, the slope of  $G'$  curve at low frequencies increases by POSS addition and this increase is noticeably higher, for TSIB-PS system. In Table 3, the measured viscosity

values at low and high frequencies and the values of the cross over frequency are reported. By adding POSS, the interaction between the components (viscosity reduction at low frequency) and easier processability (viscosity reduction at high frequencies) were observed. Moreover, the POSS presence shifts the crossover frequency points between  $G'$  and  $G''$  to higher frequencies, as seen in the last column of Table 3. The shift is less pronounced for the systems containing closed-cage POSS. It is interesting to highlight a marked shift of the cross-over point for the TSIB-PS system.

**Table 3.** Viscosity values at low and high frequencies and cross over between  $G'$  and  $G''$  moduli of all the investigated samples

Sample	$\eta^*$ [Pa·s] at $\omega = 0.1$ rad/s	$\eta^*$ [Pa·s] at $\omega = 100$ rad/s	$\omega_{\text{cross-over}}$ [rad/s]
PS	$1.72 \cdot 10^5$	$1.39 \cdot 10^3$	0.25
IB-PS	$0.98 \cdot 10^5$	$0.89 \cdot 10^3$	0.39
IO-PS	$1.10 \cdot 10^5$	$0.95 \cdot 10^3$	0.39
TSIB-PS	$0.49 \cdot 10^5$	$0.69 \cdot 10^3$	1.58
TSIO-PS	$0.77 \cdot 10^5$	$0.73 \cdot 10^3$	0.63
TSPH-PS	$1.01 \cdot 10^5$	$0.93 \cdot 10^3$	0.63

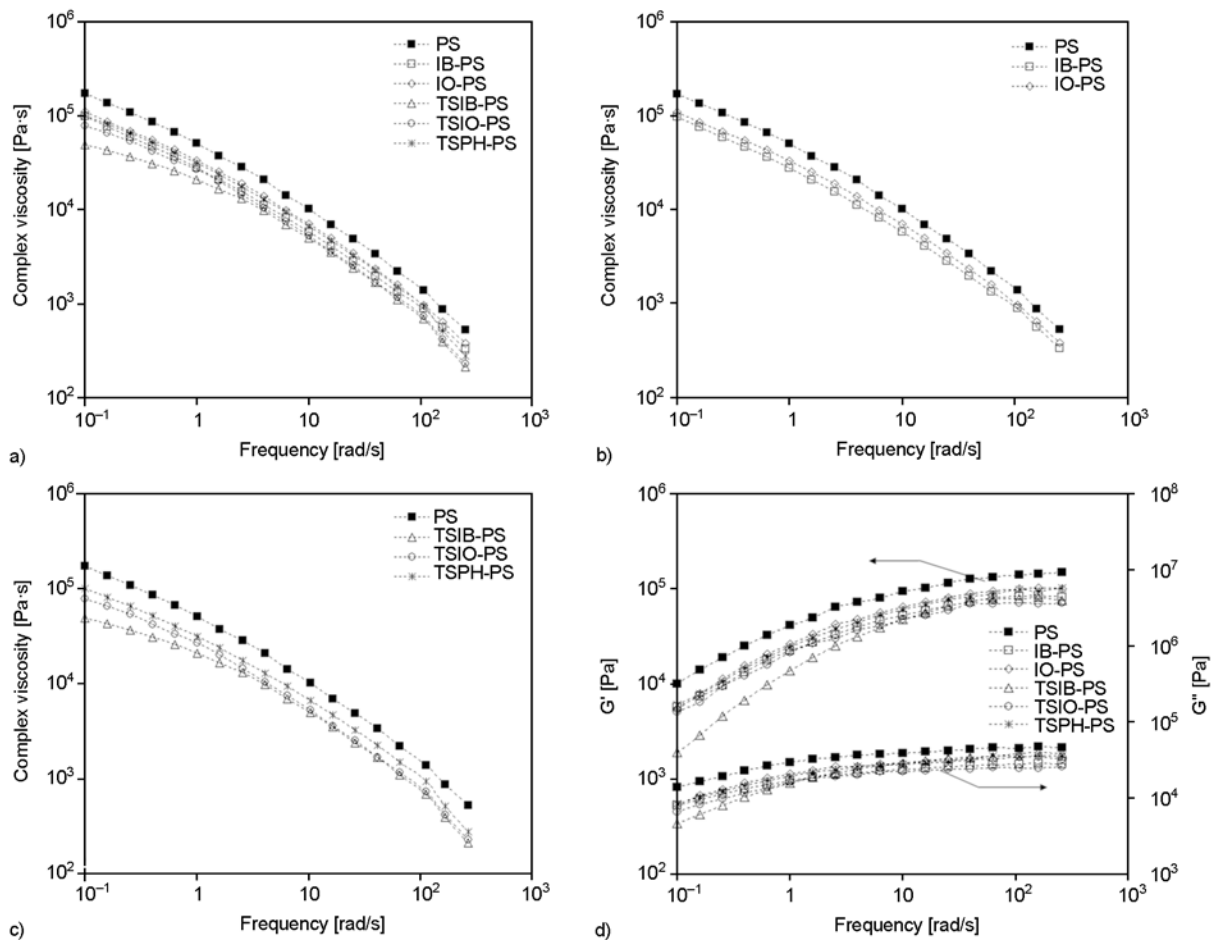


**Figure 1.** PS and POSS-PS nanocomposites: (a) flow curves of all materials; (b) flow curves of PS additivated with closed cage POSS; (c) flow curves of PS additivated with open cage POSS; (d)  $G'$  and  $G''$  moduli of all materials

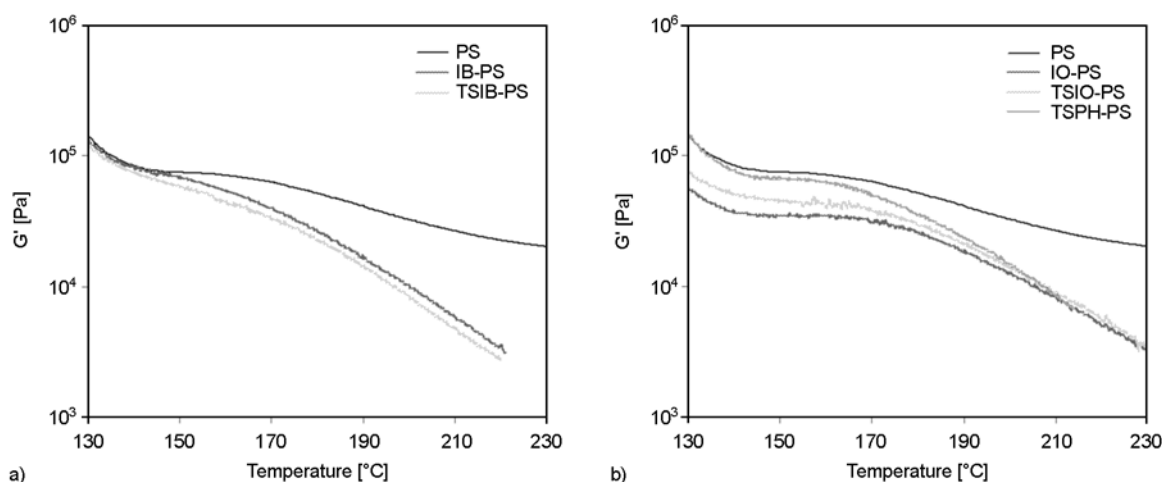


**Figure 2.** Storage modulus ( $G'$ ) as a function of the temperature of PS and POSS-PS nanocomposites

Finally, the  $G'$  modulus was measured as a function of the temperature as seen in Figure 2. The pristine PS shows a clearly pronounced plateau in the  $G'-T(^{\circ}\text{C})$  curve in the range between 130–170 $^{\circ}\text{C}$ . The plateau is less extended for all the POSS additivated systems and disappears in the TSIB-PS system. Additionally the slope of the curves at higher temperature values increases significantly in POSS containing PS samples and is highest for TSIB-PS system.

Moreover, all the rheological investigations suggest that the melt properties of the POSS-PS samples are significantly influenced by the POSS presence. In fact, the POSS loading leads to a significant viscosity and moduli decrease and to a less extended plateau (in some case to its disappearance) in the  $G'$  trend vs temperature curves due to evident a plasticizer and/or lubricant effect, in keeping with what is reported in the literature [22]. The global effect of the POSS loading can be explained considering three synergic actions, i.e. the free volume increase, the reduction of the friction between the macromolecules and the entanglement density decrease due to the penetration and good dispersion of the POSS molecules into matrix. Furthermore, considering the synergic action of these actions, it is possible to suggest that the rheological behaviour of POSS-PS systems is significantly influenced by both inorganic framework and pendent organic groups. The open inorganic cage is more flexible than the close cage and this fact probably favours the reduction of the frictional effect between the matrix macromolecules. The length of the organic pendent groups determines the free volume variations, i.e. the long

pendent organic groups favour the increase of the free volume but the short pendent groups make a POSS molecule more mobile and favours the decrease of the entanglement density of the polystyrene macromolecules.

### 3.3. Mechanical and dynamic mechanical thermal analysis

The main mechanical properties, i.e. elastic modulus,  $E$ , tensile strength,  $TS$ , and elongation at break,  $EB$ , were measured and the obtained results are reported in Table 4. The POSS loading leads to a slight decrease of the elastic modulus and of the tensile strength. In particular, the reduction of both the elastic modulus and tensile strength of the TSIB-PS with respect to the pristine PS is about 8%, while the drop of the TSPH-PS is much less i.e. only about 1.5%. PS is brittle (its elongation at break is about 3%) and the POSS loading does not change this value, see Table 4.

In keeping with the tensile test results obtained at room temperature, the POSS loading leads to a decrease of the modulus  $E'$  at  $T = 30^{\circ}\text{C}$ , obtained by

**Table 4.** Mechanical properties: elastic modulus,  $E$ , tensile strength,  $TS$  and elongation at break,  $EB$  (measured by tensile test) and modulus  $E'_{30^{\circ}\text{C}}$  (measured by DMTA) of the pristine PS and POSS-PS systems

Samples	$E$ [MPa]	$TS$ [MPa]	$EB$ [%]	$E'_{30^{\circ}\text{C}}$ [MPa]
PS	1480±74.0	34.5±1.7	3.0±0.15	1476
IB-PS	1370±68.5	32.1±1.6	3.0±0.15	1356
IO-PS	1392±69.6	31.8±1.6	3.1±0.15	1397
TSIB-PS	1358±67.9	31.5±1.5	3.2±0.16	1329
TSIO-PS	1362±68.1	31.5±1.5	3.0±0.15	1308
TSPH-PS	1458±72.9	34.0±1.7	3.0±0.15	1417



DMTA, with respect to the PS, as shown in the last column of Table 4. More information about the trend of the  $E'$  and the damping factor ( $\tan\delta$ ) as a function of the temperature can be found in Figure 3. The peak of  $\tan\delta$  (values are reported in Table 5, see first column) shifts to a lower temperature by POSS addition and also a slight decrease of the peak intensities was observed. This shift is more pronounced for all the open cage POSS additivated systems and, in particular, for TSIB-PS system. The decrease of the rigidity of POSS additivated systems may be explained considering the low molecular weight of the pristine POSS systems, see Table 1. Generally, the addition of low molecular weight plasticizers leads to a decrease of the rigidity and in some case, to a rise of the elasticity [24]. The mechanical behaviour of POSS-PS systems seems to be influenced much more by the chemical nature of the pendent groups than the type of the inorganic cage. The elastic modulus values of the POSS-PS systems prepared with open cage POSS are lower than the values of those prepared with

closed cage POSS but at the same time, the solid state properties of TSPH-PS sample are very similar to those of the pristine PS, probably due to the  $\pi$ - $\pi$  interaction between the phenyl rings. Furthermore, the change of the macroscopical properties of the POSS based nanocomposites, correlated to a good POSS molecules dispersion, can be obtained considering some chemical interaction between the pendent organic groups and the macromolecules of the host matrix. So, the  $\pi$ - $\pi$  interaction may be stronger in PS matrix, taking into account the side position of the benzene ring in polystyrene in comparison with matrices as PKFE [25] or PC [25, 26], in agreement with the literature.

### 3.4. Differential scanning calorimetry

The glass transition temperature, estimated as the mid-point in the heating curves between the onset and end transition points, of neat PS is about 102.0°C, as reported in Table 5. In Figure 4 is shown the sec-

**Table 5.** Damping factor (measured by DMTA) and glass transition temperatures (measured by DSC) of pristine PS and POSS-PS systems

Samples	$T_{\tan\delta}$ [°C]	$T_g$ [°C]		
		$T_{\text{onset}}$	$T_{\text{mid-point}}$	$T_{\text{end}}$
PS	118.5	98.5	102.0	105.5
IB-PS	116.8	98.0	101.3	104.0
IO-PS	116.1	95.5	100.2	105.0
TSIB-PS	113.5	94.2	98.0	102.5
TSIO-PS	115.3	94.0	99.2	104.5
TSPH-PS	115.0	95.8	99.0	104.5

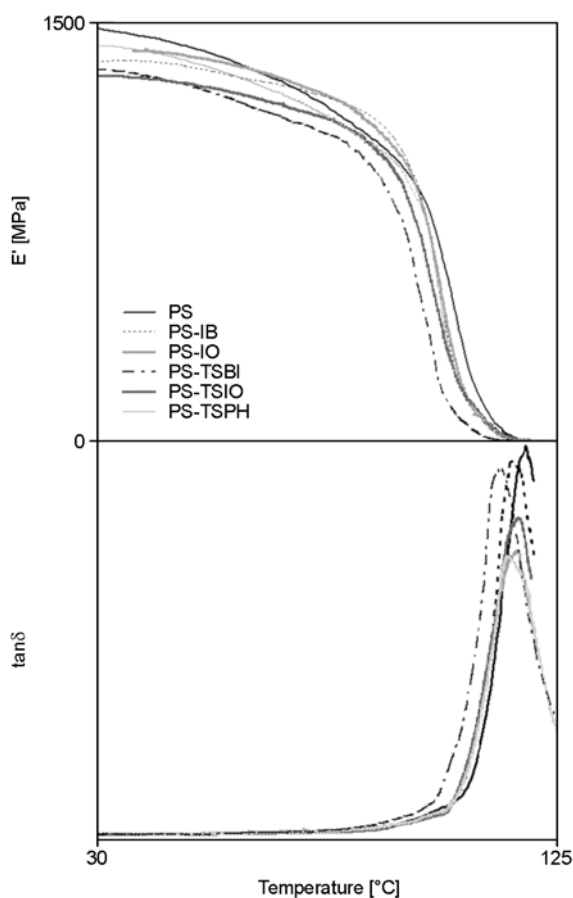


**Figure 3.** Modulus ( $E'$ ) and damping factor ( $\tan\delta$ ) as a function of the temperature of PS and POSS-PS nanocomposites

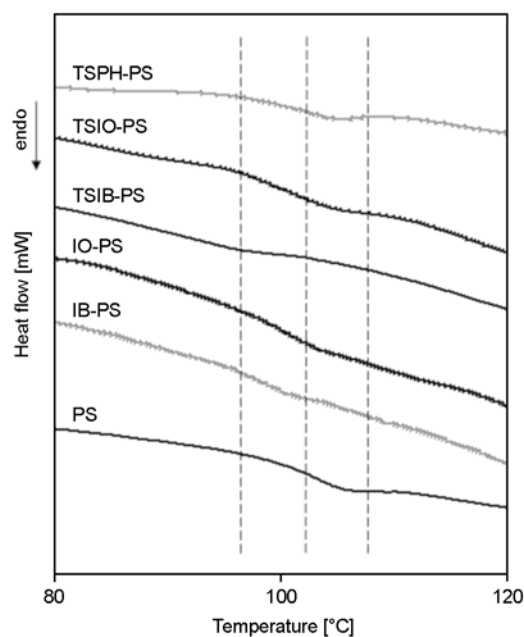


**Figure 4.** DSC traces of second heating of PS and POSS-PS nanocomposites

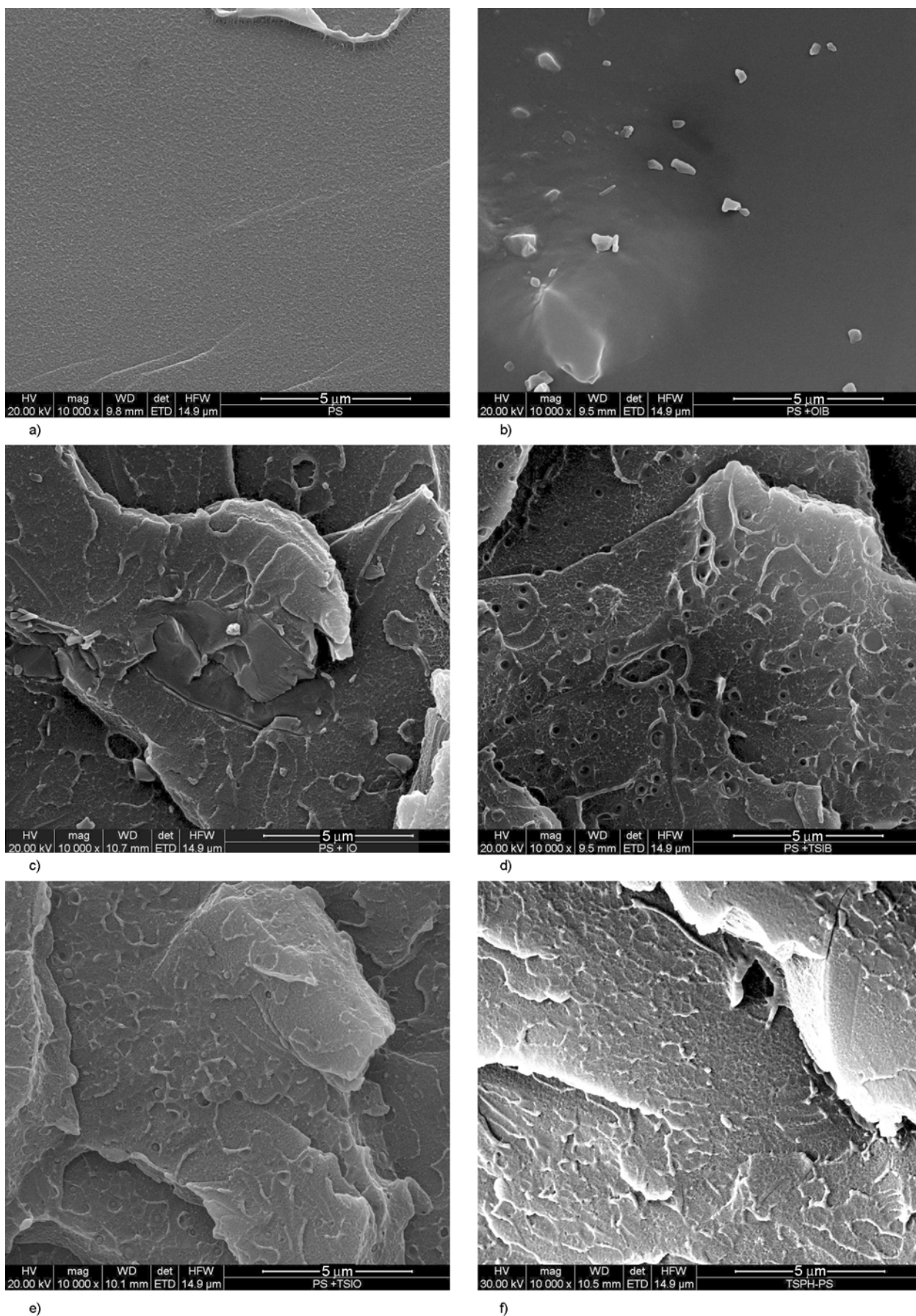


**Figure 5.** SEM images of all the investigated samples: (a) neat PS; (b) IB-PS; (c) IO-PS; (d) TSIB-PS; (e) TSIO-PS; (f) TSPH-PS

ond scan of heating scan. The POSS presence leads to a lower glass transition temperature. A similar decrease of the onset, mid-point and end temperatures was noticed. The onset and end temperatures are, respectively, the temperatures at which the transition process starts and finishes for low and high molecular weight PS fractions. A same shifting of the three temperatures to lower temperatures suggests that the nature of the transition of the PS macromolecules is not modified; and only the temperature at which the glass transition occurs is modified due to the POSS presence. In fact, the POSS-PS samples exhibit a similar behaviour to that imparted by low molecular weight PS. It is evident that the POSS molecules show a plasticizer effect and this effect is more pronounced for POSS samples with open cage. Moreover, the TSIB-PS sample shows the lowest glass transition, also in keeping with the lowest value of  $\tan\delta$ . The glass transition temperature seems not to be influenced significantly by the chemical nature of the pendent organic groups, but rather depends on the type of the inorganic framework. In particular, the POSS with open cage induces a more pronounced decrease of the glass transition temperature than the POSS with closed cage.

### 3.5. Scanning electron microscopy

In Figure 5 the SEM image of PS and POSS-PS nanocomposites are shown. The formation of POSS aggregates at micrometric level on the fractured surface of IB-PS sample is clearly noticed (see Figure 5b), while, the POSS-PS nanocomposites show different matrix morphology and also no aggregates can be observed (see Figure 5c–f). The empty holes are visible on the images and they are probably due to the POSS particles attached on the other fractured surfaces. The open cage POSS-PS systems show better dispersion than the closed cage POSS-PS nanocomposites. The SEM observations are in total agreement with the calculated theoretical solubility parameters. In particular, the solubility parameter of the IB-POSS is larger than that of the PS and some aggregation between the molecules occurs.

## 4. Conclusions

In this work the structure-properties relationships of the POSS-PS systems were accurately investigated

and their variation with respect to that of the neat PS were highlighted. The affinity between the PS matrix and POSS samples was estimated from the theoretical calculated solubility parameters and by morphology analysis. Furthermore, the rheological analysis suggests that the POSS molecule acts as plasticizers in the melt and it is can be explained considering three synergic effects: the increase of the free volume, the reduction of the friction between the PS macromolecules and the decrease of the entanglement density due to the penetration and good dispersion of the POSS molecules into matrix. Additionally the efficiency as plasticizers of the POSS molecules may be related to the structure of their inorganic framework and the chemical nature and length of the pendent organic groups. The open cage POSS system shows a more pronounced plasticizer effect onto PS matrix than the closed cage POSS systems due to the major flexibility of the inorganic framework. The POSS system with closed cage and short organic pendent groups shows a tendency to re-aggregates formation (i.e. IB-POSS), while, the POSS with open cage and same organic groups is the best plasticizer (i.e. TSIB-POSS). The POSS systems with long pendent organic groups favour the increase of the free volume in the nanocomposites but at the same time, do not favour the decrease of the entanglement density (i.e. IO-POSS and TSIO-POSS). It is interesting to highlight that the POSS loading leads to a decrease of the rigidity, glass transition temperature and damping factor. The last effect is less pronounced where the chemical nature of the organic groups is similar to that of the polymeric matrix. In fact, the TSPH-POSS presence does change only slightly the properties of the PS in the solid state, also due to the  $\pi$ - $\pi$  interaction between the phenyl rings.

Really, the POSS molecules are expensive additives but considering their performance improvement and non-toxicity could be believe as excellent plasticizers for polymer based nanocomposites in medical and aero-space applications.

## Acknowledgements

This work has been financially supported by University of Palermo, Progetti innovativi ordinari Palermo 2007 – ‘Nuovi materiali compositi nanostrutturati: preparazione e caratterizzazione’ (codice OIPA07P92W).



## References

- [1] Harrison P. G.: Silicate cages: Precursors to new materials. *Journal of Organometallic Chemistry*, **542**, 141–183 (1997).  
DOI: [10.1016/S0022-328X\(96\)06821-0](https://doi.org/10.1016/S0022-328X(96)06821-0)
- [2] Provatas A., Matison J. G.: Silsesquioxanes: Synthesis and applications. *Trends in Polymer Science*, **5**, 327–332 (1997).
- [3] Zheng L., Waddon A. J., Farris R. J., Coughlin E. B.: X-ray characterizations of polyethylene polyhedral oligomeric silsesquioxane copolymers. *Macromolecules*, **35**, 2375–2379 (2002).  
DOI: [10.1021/ma011855e](https://doi.org/10.1021/ma011855e)
- [4] Liu L., Tian M., Zhang W., Zhang L., Mark J. E.: Crystallization and morphology study of polyhedral oligomeric silsesquioxane (POSS)/polysiloxane elastomer composites prepared by melt blending. *Polymer*, **48**, 3201–3212 (2007).  
DOI: [10.1016/j.polymer.2007.03.067](https://doi.org/10.1016/j.polymer.2007.03.067)
- [5] Iyer P., Mapkar J. A., Coleman M. R.: A hybrid functional nanomaterial: POSS functionalized carbon nanofiber. *Nanotechnology*, **20**, 325603–325609 (2009).  
DOI: [10.1088/0957-4484/20/32/325603](https://doi.org/10.1088/0957-4484/20/32/325603)
- [6] Lee Y.-J., Huang J.-M., Kuo S.-W., Lu J.-S., Chang F.-C.: Polyimide and polyhedral oligomeric silsesquioxane nanocomposites for low-dielectric applications. *Polymer*, **4**, 173–181 (2005).  
DOI: [10.1016/j.polymer.2004.10.003](https://doi.org/10.1016/j.polymer.2004.10.003)
- [7] Zhang Y., Lee S., Yoonessi M., Liang K., Pittman C. U.: Phenolic resin–trisilanolphenyl polyhedral oligomeric silsesquioxane (POSS) hybrid nanocomposites: Structure and properties. *Polymer*, **47**, 2984–2996 (2006).  
DOI: [10.1016/j.polymer.2006.03.005](https://doi.org/10.1016/j.polymer.2006.03.005)
- [8] Hosaka N., Torikai N., Otsuka H., Takahara A.: Structure and dewetting behavior of polyhedral oligomeric silsesquioxane-filled polystyrene thin films. *Langmuir*, **23**, 902–907 (2007).  
DOI: [10.1021/la062255h](https://doi.org/10.1021/la062255h)
- [9] Fina A., Bocchini S., Camino G.: Catalytic fire retardant nanocomposites. *Polymer Degradation and Stability*, **93**, 1647–1655 (2008).  
DOI: [10.1016/j.polymdegradstab.2008.05.027](https://doi.org/10.1016/j.polymdegradstab.2008.05.027)
- [10] Misra R., Alidedeoglu A. H., Jarrett W. L., Morgan S. E.: Molecular miscibility and chain dynamics in POSS/polystyrene blends: Control of POSS preferential dispersion states. *Polymer*, **50**, 2906–2918 (2009).  
DOI: [10.1016/j.polymer.2009.03.057](https://doi.org/10.1016/j.polymer.2009.03.057)
- [11] Zhang W., Fang B., Walther A., Müller A. H. E.: Synthesis via RAFT polymerization of tadpole-shaped organic/inorganic hybrid poly(acrylic acid) containing polyhedral oligomeric silsesquioxane (POSS) and their self-assembly in water. *Macromolecules*, **42**, 2563–2569 (2009).  
DOI: [10.1021/ma802803d](https://doi.org/10.1021/ma802803d)
- [12] Jeon J.-H., Lim J.-H., Kim K.-M.: Hybrid nanocomposites of palladium nanoparticles having POSS and MWNTs via ionic interactions. *Macromolecular Research*, **17**, 987–994 (2009).  
DOI: [10.1007/BF03218646](https://doi.org/10.1007/BF03218646)
- [13] Tanaka K., Adachi S., Chujo Y.: Structure–property relationship of octa-substituted POSS in thermal and mechanical reinforcements of conventional polymers. *Journal of Polymer Science Part A: Polymer Chemistry*, **47**, 5690–5697 (2009).  
DOI: [10.1002/pola.23612](https://doi.org/10.1002/pola.23612)
- [14] Wu J., Mather P. T.: POSS polymers: Physical properties and biomaterials applications. *Journal of Macromolecular Science Part C: Polymer Reviews*, **49**, 25–63 (2009).  
DOI: [10.1080/15583720802656237](https://doi.org/10.1080/15583720802656237)
- [15] Lim S.-K., Hong E.-P., Choi H. J., Chin I.-J.: Polyhedral oligomeric silsesquioxane and polyethylene nanocomposites and their physical characteristics. *Journal of Industrial and Engineering Chemistry*, **16**, 189–192 (2010).  
DOI: [10.1016/j.jiec.2010.01.049](https://doi.org/10.1016/j.jiec.2010.01.049)
- [16] Mohammad S. A., Wee A. G., Rumsey D. J., Schrickler S. R.: Maxillofacial materials reinforced with various concentrations of polyhedral silsesquioxanes. *Journal of Dental Biomechanics*, 701845/1–701845/6 (2010).  
DOI: [10.4061/2010/701845](https://doi.org/10.4061/2010/701845)
- [17] Brandhorst H., Isaacs-Smith T., Wells B., Lichtenhan J. D., Fu B. X.: POSS coating as replacements for solar cell cover glasses. in ‘Conference Record of the 2006 IEEE 4<sup>th</sup> World Conference on Photovoltaic Energy Conversion, Waikoloa, USA’ 1887–1890 (2007).  
DOI: [10.1109/WCPEC.2006.279864](https://doi.org/10.1109/WCPEC.2006.279864)
- [18] Zhang Z., Gu A., Liang G., Ren P., Xie J., Wang X.: Thermo-oxygen degradation mechanisms of POSS/epoxy nanocomposites. *Polymer Degradation and Stability*, **92**, 1986–1993 (2007).  
DOI: [10.1016/j.polymdegradstab.2007.08.004](https://doi.org/10.1016/j.polymdegradstab.2007.08.004)
- [19] Tang Y., Lewin M.: Migration and surface modification in polypropylene (PP)/polyhedral oligomeric silsesquioxane (POSS) nanocomposites. *Polymers for Advanced Technologies*, **20**, 1–15 (2009).  
DOI: [10.1002/pat.1229](https://doi.org/10.1002/pat.1229)
- [20] Zhang B., Chen Y., Wang J., Blau W. J., Zhuang X., He N.: Multi-walled carbon nanotubes covalently functionalized with polyhedral oligomeric silsesquioxanes for optical limiting. *Carbon*, **48**, 1738–1742 (2010).  
DOI: [10.1016/j.carbon.2010.01.015](https://doi.org/10.1016/j.carbon.2010.01.015)
- [21] Wu J., Haddad T. S., Kim G.-M., Mather P. T.: Rheological behavior of entangled polystyrene–polyhedral oligosilsesquioxane (POSS) copolymers. *Macromolecules*, **40**, 544–554 (2007).  
DOI: [10.1021/ma061886f](https://doi.org/10.1021/ma061886f)



- [22] Romero-Guzmán M. E., Romo-Urbe A., Zárate-Hernández B. M., Cruz-Silva R.: Viscoelastic properties of POSS–styrene nanocomposite blended with polystyrene. *Rheologica Acta*, **48**, 641–652 (2009). DOI: [10.1007/s00397-009-0358-8](https://doi.org/10.1007/s00397-009-0358-8)
- [23] van Krevelen D. W., Nijenhuis K. te: Cohesive properties and solubility. in ‘Properties of polymers’ (eds.: van Krevelen D. W., Nijenhuis K. te.) Elsevier, Oxford, 189–228 (2009).
- [24] Wypych G.: Handbook of plasticizers. ChemTec Publishing, Toronto (2004).
- [25] Iyer S., Schiraldi D. A.: Role of specific interactions and solubility in the reinforcement of bisphenol A polymers with polyhedral oligomeric silsesquioxanes. *Macromolecules*, **40**, 4942–4952 (2007). DOI: [10.1021/ma061180l](https://doi.org/10.1021/ma061180l)
- [26] Sánchez-Soto M., Schiraldi D. A., Illescas S.: Study of the morphology and properties of melt-mixed polycarbonate–POSS nanocomposites. *European Polymer Journal*, **45**, 341–352 (2009). DOI: [10.1016/j.eurpolymj.2008.10.026](https://doi.org/10.1016/j.eurpolymj.2008.10.026)

# Interlaminar fatigue crack growth behavior of MWCNT/carbon fiber reinforced hybrid composites monitored via newly developed acoustic emission method

G. Romhány\*, G. Szabó

Department of Polymer Engineering, Faculty of Mechanical Engineering, Budapest University of Technology and Economics. Műegyetem rkp 3., H-1111, Budapest, Hungary

Received 8 November 2011; accepted in revised form 29 January 2012

**Abstract.** The aim of this research was the investigation of the effect of carbon nanotube addition on the mode I interlaminar fatigue properties of carbon fiber reinforced composites. The authors developed a localization methodology to track the interlaminar fatigue crack front using the acoustic emission (AE) technique. According to the test evaluation the carbon nanotube reinforcement decreased the crack propagation rate by 69% compared to the composite containing no nanotubes. Besides that, the fatigue life also increased significantly, the nanotube reinforced composite could withstand 3.8-times more cycles to failure than the unfilled matrix composite.

**Keywords:** fracture and fatigue, delamination, carbon nanotube, acoustic emission, hybrid nanocomposite

## 1. Introduction

High performance polymer composites are subjected to fatigue loading in most of their applications (vehicles, wind turbines, etc.). One of the common damage modes caused by such loadings is delamination, the separation of the adjacent layers. To describe the susceptibility to delamination various parameters can be used, one of these is interlaminar fracture toughness. From the three crack opening modes (opening mode (mode I), sliding mode (mode II), tearing mode (mode III)), the opening mode (mode I) is the most common, and therefore (besides mode II) the most intensively investigated in the literature. The knowledge of this material property can be useful for material selection and mechanical design in case of product development, and for the comparison of material types, qualification in case of material development. Because of these aspects it is important to investi-

gate the interlaminar toughness of composites at both static and cyclic loading.

A part of the numerous publications in the field of quasistatic interlaminar crack propagation tests dealt with the effect of test parameters (for example: test speed [1]), laminate layup structure [2–6], others have characterized the effect of fillers/reinforcing materials on the fracture toughness (for example: carbon nanofiber/carbon fiber in epoxy [7, 8], glass fiber in unsaturated polyester [9], carbon nanotube/carbon fiber in epoxy [10], fluoride functionalized carbon nanotubes/carbon fibers in epoxy [11], amine functionalized carbon nanotubes/glass fibers in epoxy [12], carbon nanotubes grown radially from vapor on the surface of carbon fiber in epoxy [13], vapor grown carbon fibers/carbon fibers in epoxy [14], clay nanoparticles/carbon fibers in epoxy [15–17], halloysite nanotubes/carbon fibers in epoxy [18]). All of the papers utilizing nanoparti-

\*Corresponding author, e-mail: [romhany@pt.bme.hu](mailto:romhany@pt.bme.hu)  
© BME-PT

cle filling report increases from some to 300% in interlaminar fracture properties (for example:  $G_{IC}$  or  $G_{IIC}$ ). This increase has been explained with new failure modes (like the pullout of nanotubes), the formation of covalent bonds between the fiber and the matrix provided by functionalized nanotubes, the deflection of the crack front, and thereby the increase of the energy dissipation (indicated by the rougher, tougher fracture surface) caused by the nanoparticles.

Almost no results are available from interlaminar fatigue tests, because of the complexity and time consumption of these tests. Argüelles *et al.* [19] demonstrated that fatigue crack initiation is strongly influenced by the production technology (film thickness, resin content etc.), so a large number of tests have to be performed because of the high standard deviation. Hojo *et al.* [20] showed, that the thickness of the middle layer does not significantly affect the interlaminar properties in mode I crack propagation in contrast with mode II, where a thicker layer caused significant improvement. Hojo *et al.* [21] successfully increased the cyclic interlaminar fracture toughness both by the polyamide filled and by ionomeric middle layer.

After their discovery in 1991 carbon nanotubes came into focus of interest not only in the field of material science, but also almost all research areas. Researchers are trying to exploit the unique properties of carbon nanotubes in numerous applications, like in electronic components [22], fuel cells [23] and last but not least in the field of material science as new structural materials [24, 25]. In our previous work we [26] investigated the effect of carbon nanotube reinforcement on the static mode I interlaminar fracture toughness of carbon fiber/epoxy laminates. Some papers indicate that carbon nanotubes could provide good results also in case of cyclic loading [27, 28], hinder the fatigue crack growth [29], improve the fatigue resistance of conventional fiber reinforced composites [30]. The aim of our present research is to investigate the effect of carbon nanotube reinforcement on the cyclic mode I interlaminar fracture toughness of the same material and to develop an acoustic emission localization based crack tracking method capable of crack propagation tracking during fatigue testing.

## 2. Materials and methods

### 2.1. Materials

Eporezit FM20 (P+M Polimerkémia Kft., Budapest, Hungary, Hungary) epoxy resin with Eporezit T16 curing agent was used as the matrix of the composite laminates, the mixing weight ratio was 100:20 according to the producer specifications.

As fiber reinforcement Zoltek (Nyergesújfalu, Hungary) PX35FBUD0300 unidirectional carbon fabric, consisting of Panex35 50k (surface weight 309 g/m<sup>2</sup>) tows was used.

Bayer Baytubes® BT150 HP (Leverkusen, Germany) multiwalled carbon nanotubes (MWCNTs) were used as filler in one portion of the matrix. The nanotubes were produced in a CVD based catalytic process resulting in an average outer diameter between 13–16 nm, length above 1 μm and carbon purity above 99% according to the manufacturer.

### 2.2. Composite preparation

Because our previous static double cantilever beam (DCB) measurements [26] showed that significant interlaminar mechanical property increase could be achieved only up to 0.3 weight% nanotube content, 0.3 weight% nanotube reinforced and unreinforced specimens have been studied. The nanotube content used in this research has been selected based only on static results, so in our further work we are planning to obtain the optimal nanotube content for cyclic properties. The nanotubes were dispersed in the epoxy resin by three roll milling on an Enrico Molteni CIEM (Senago, Italy) three roll mill in 4 pass troughs. In their raw form the nanotubes form aggregates with a diameter of some millimeters, so not only their proper dispersion, but also the milling of these aggregates was of key importance. To characterize the effectiveness of the milling, fineness of grind measurements, common in case of dispersion of pigments, were carried out after the second, third, and fourth pass through. The maximum particle sizes were 15, 10 and below 10 μm respectively, which is the lowest measurable particle size of the equipment. There was no significant difference between result of the third and the fourth pass through, so probably it was the lowest achievable particle size by the given equipment.

Because well dispersed nanotubes cause an order of magnitude increase in resin viscosity [31], hand

lamination was selected combined with pressing to achieve reproducible quality and uniform laminate thickness.

The 4 mm thick laminates were produced by hand lamination of 10 plies of unidirectional carbon fabric impregnated with the resin. A 50  $\mu\text{m}$  thick PET film was used as a delamination initiator insert in the center plane (between the 5<sup>th</sup> and 6<sup>th</sup> lamina) of the laminates. Both sides of the film were coated with mould release agent to minimize adhesion between the film and the matrix of the composite. To avoid voids, the laminate was rolled after every two plies.

To achieve uniform thickness and fiber content, to remove the excess resin, the laminates were pressed with two 4 mm thick steel plates placed as spreaders next to the laminates in the press. The laminates were cured for 4 hours at 60°C after the pressing in a Heraeus UT20 (Thermo Fisher Scientific, Waltham, MA, USA) drying oven.

### 2.3. Specimen preparation

210 mm long, 25 mm wide and 4 mm thick specimens according to ASTM D 5528 – 01 were cut from the laminates, the length of the delamination initiator was 65 mm. The edges of each specimen were coated just ahead of the insert with a thin layer of water-based typewriter correction fluid to aid the visual detection of delamination propagation. 100 mm length of the specimens was marked with thin vertical lines every 2 mm from the insert to help the recording of the crack front position. Steel load hinges were mounted on the top and the bottom of each specimen using Sikadur 330 (Sika, Germany) adhesive.

### 2.4. Fatigue mode I interlaminar crack propagation test

Interlaminar fatigue tests were performed on DCB specimens using an Instron 8872 (Norwood, USA) servo-hydraulic universal, computer controlled loading frame with Instron Fasttrack 8800 control and data acquisition unit and an Instron Dynacell 1 kN load cell. The applied load was sinusoidal with a frequency of 2 Hz, a maximal load of ( $P_{\text{max}}$ ) 70 N and a stress factor of ( $R$ ) 0.2. 10–10 specimens were tested from the composite and the carbon nanotube reinforced hybrid composite.

### 2.5. Acoustic emission

The acoustic emission signals originating from the crack propagation were recorded by Micro30S (Physical Acoustic Corporation, USA) sensors in the frequency range from 100 to 600 kHz, and stored by a Sensophone AED-40 (Gereb and Co., Ltd., Budapest, Hungary) device. Logarithmic amplification was applied. The threshold was set to 30 dB to filter out ambient noises, and the reference voltage of the test device was 1  $\mu\text{V}$ . Two AE sensors were fixed on the surface of the specimens at given positions, 120 mm-s from each other, the distance between the first sensor and the artificial initial delamination was 20 mm. Before the tests, the sound velocity in the specimen, necessary for the localization, was measured. The sensors were fixed to the specimen surface with bee wax, which functioned as a coupling material and as an adhesive. Using one of the sensors as an emitter the device recorded the detection time of the signal. With the sensor distance known, the device calculated the AE signal propagation speed (9000 m/s). The test setup can be seen in Figure 1.

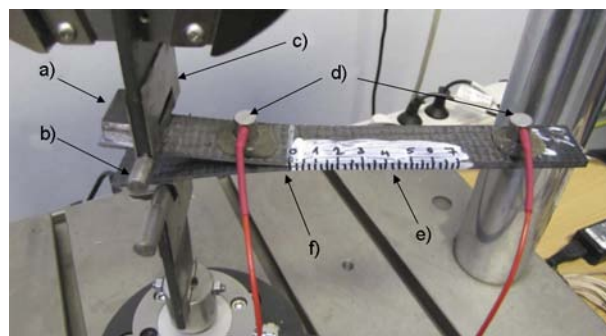


**Figure 1.** The DCB test setup a) load block, b) fixing pin, c) adapter hinge, d) AE sensors, e) scale, f) test specimen

### 2.6. Transmission electron microscopy (TEM)

80 nm thick slices of the prepared specimens were investigated by TEM. The slices had been cut by a Leica Ultramicrotome EMUC6 (Wetzlar, Germany) microtome. The micrographs were taken using a FEI Morgani 268D (Hillsboro, USA) TEM.

## 3. Result and discussion

To characterize the dispersion of the carbon nanotubes in the matrix, TEM micrographs were taken of the thin slices of the matrix of the hybrid composite specimens (Figure 2). In the micrographs

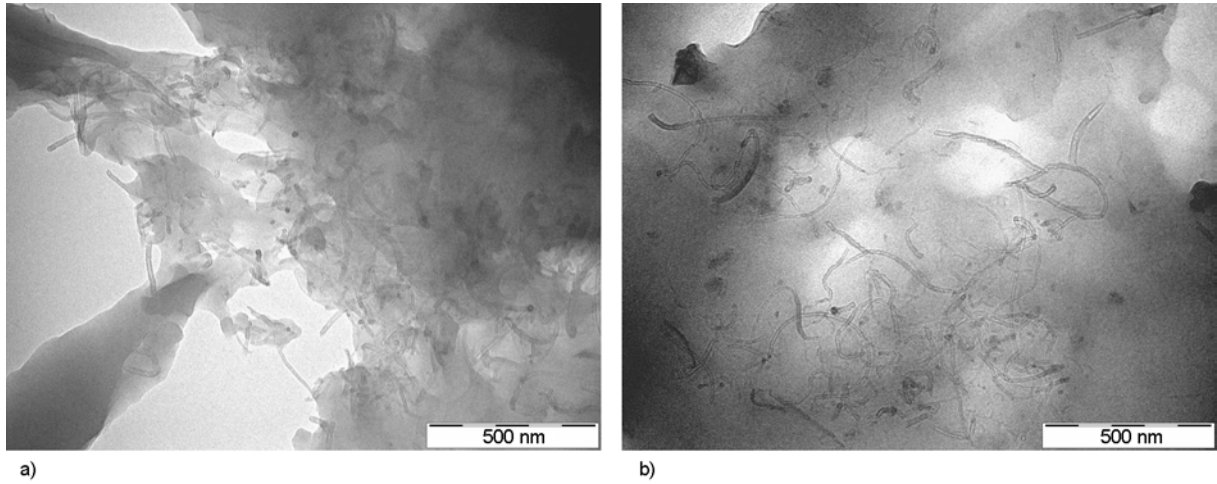


**Figure 2.** TEM micrographs of the matrix of a hybrid composite specimen (two positions of the same specimen, a and b)

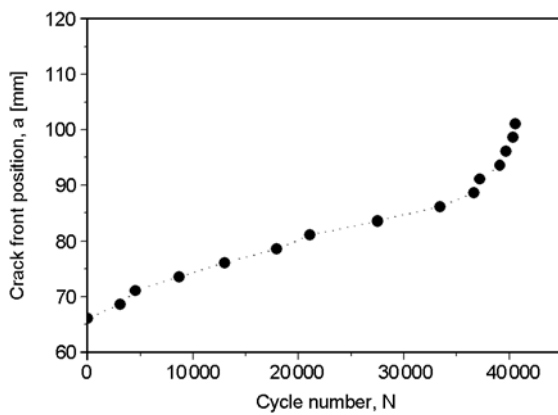


**Figure 3.** Crack front position – cycle number diagram of a 0.3 weight% nanotube filled hybrid composite specimen (obtained from visual observation)

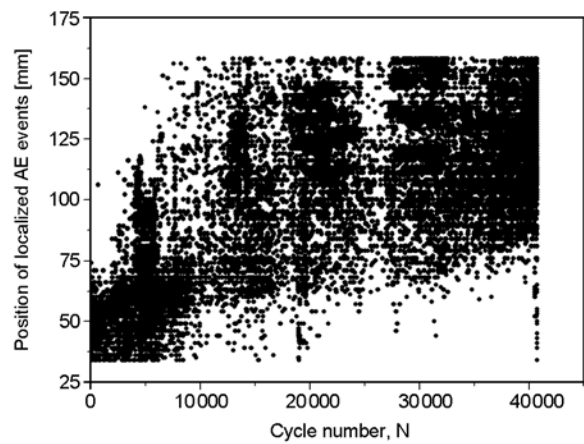


**Figure 4.** Localized AE signals from the fatigue test of a 0.3 weight% nanotube reinforced hybrid composite (the origin of the coordinate system is the line of loading; same specimen as in Figure 3)

well dispersed carbon nanotubes can be observed, so the mixing was effective.

The crack front position values were recorded as a function of cycle number by visual observation. A typical crack front position vs. cycle number curve can be seen in Figure 3.

The positions of the AE signal sources were also localized. The localized signal source positions from the fatigue test of a 0.3 weight% nanotube reinforced hybrid composite are presented in Figure 4. The localized AE signals almost completely cover the range between the two microphones. This can be explained by two factors. Firstly, the vibration of the fatigue tester provided signals originating from external sources. Secondly, the AE signal wave reflected several times from the walls of the narrow specimen, generating signals from invalid sources.

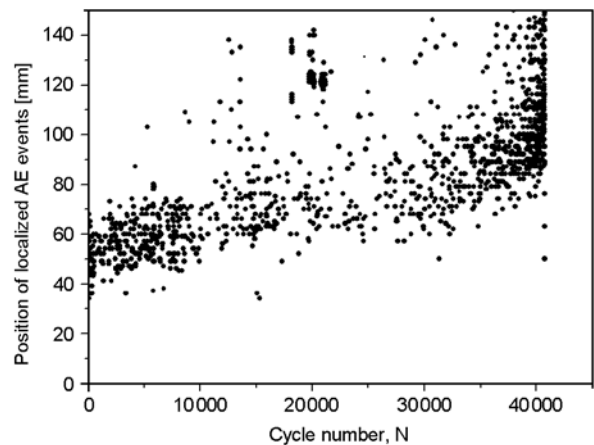


**Figure 5.** Localized AE signals from the fatigue test of a 0.3 weight% nanotube reinforced hybrid composite after the 60 dB amplitude filtering (the origin of the coordinate system is the line of loading; same specimen as in Figure 3 and 4)



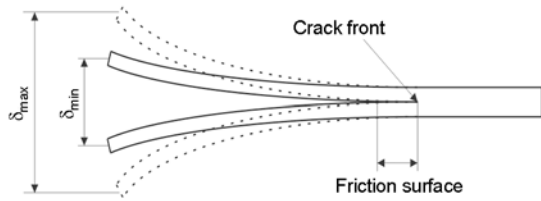


Figure 6. Friction surface of a DCB fatigue test specimen

To be able to track the crack front propagation, we have developed the following two step method. Supposing that the larger the amplitude of an AE signal is, the higher is the probability, that it originates from the actual crack propagation, in the first step we have performed an amplitude filtering to filter invalid AE signals (Figure 5). It can be observed that the strip of events representing the crack propagation narrowed down significantly, and the trend of crack propagation is somewhat clearer.

The large number of signals deviating from the trend even after filtering suggests, that some disturbing effects are still present. One such effect can be that the two separated parts of the specimen contact in each cycle, generating false AE signals through friction behind the crack front (Figure 6).

In the second step we averaged the localized signals by the following method. The initial position of the crack front is known. We kept the signals in a  $-\Delta L - +\Delta U$  window from this point.  $-\Delta L$  corresponds to the signals behind and  $+\Delta U$  in front of the crack front. If a given  $X$  number of AE signals was collected in this window, their crack position and cycle number average has been calculated and used as the actual crack position (Figure 7). To define the next crack front position signals in the  $-\Delta L - +\Delta U$

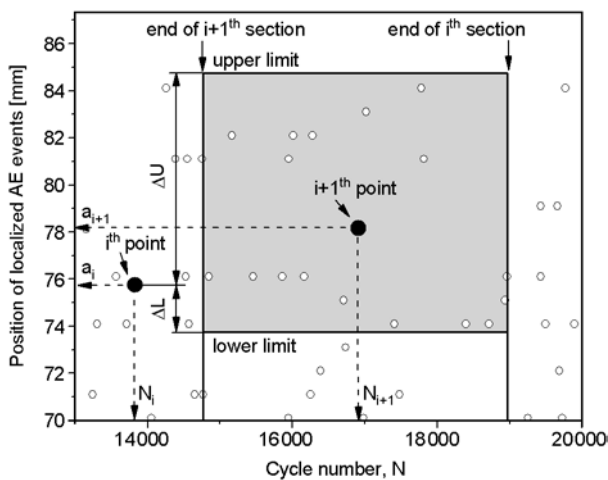


Figure 7. Method for calculating the averaged crack position in a given point (for same specimen as in Figure 3–5)

window from this point had been collected until the number of collected signals reached  $X$ . Because of the dimension of the AE sensors the localization of signals from sources also forms a patch around the crack front, because of this, signals behind the crack front also have to be collected. The window size behind the crack front can be set by the  $-\Delta L$  parameter. If  $-\Delta L$  is set to a lower value than  $+\Delta U$ , the false signals generated by the friction between the two delaminated specimen halves can be filtered.  $-\Delta L$  was set to 2 mm,  $+\Delta U$  was set to 9 mm according to the comparison with the visual crack tracking results. The number of signals used for the averaging has to be high enough to get a statistically correct average value, but more points of the crack propagation can be acquired if we set the number lower. The selection of the right  $\Delta L$ ,  $\Delta U$  and  $X$  can be therefore handled as an optimum finding task. In our case  $X$  (the number of collected AE signals to be averaged for one crack position) was set to 17.

The comparison of the crack front positions obtained from the AE measurement followed by the averaging method and recorded visually is presented in Figure 8. It can be observed that the crack propagation obtained by the two methods is similar in the stable crack propagation stage, larger differences only occur after the crack propagation becomes unstable, but the highest difference remains below 5 mm. This difference can be explained by the troublesome visual tracking of the fast moving crack in the unstable stage. According to the results visual crack tracking can be superseded by the developed AE method.

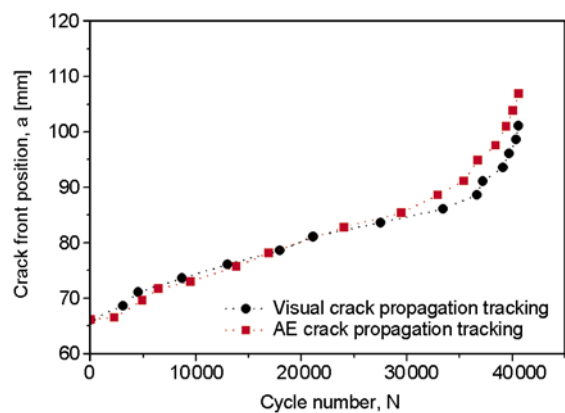
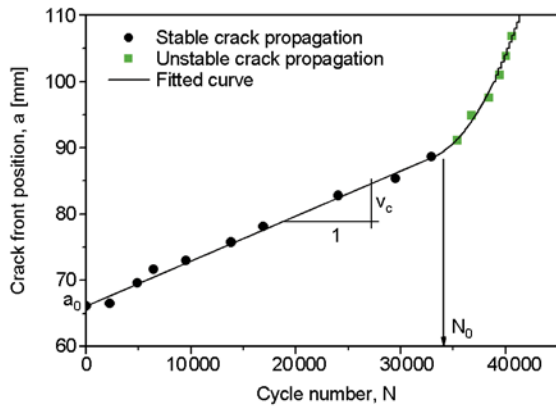


Figure 8. Comparison of the crack tracking results obtained by AE and visual crack tracking of the fatigue test of a 0.3 weight% nanotube filled hybrid composite specimen



**Figure 9.** The fitted function for obtaining the stable crack propagation rate of a 0.3 weight% nanotube filled hybrid composite specimen

In case of fatigue testing one way of comparison of failure processes is the comparison of the crack propagation rates in the stable stage. To define the stable-unstable transition and obtain the crack propagation rate a five parameter curve Equation (1) was fitted to the measured points (Figure 9):

$$a(N) = a_0 + v_c \cdot N + a_{nl}(N)$$

$$a_{nl}(N) = \begin{cases} k \cdot (N - N_0)^n & \text{if } N > N_0 \\ 0, & \text{otherwise} \end{cases} \quad (1)$$

In the diagram it can be observed, that after a specific cycle number the crack propagation becomes unstable, followed by the catastrophic failure of the specimen. The stable-unstable transition was pinpointed by the  $N_0$  parameter. The slope of the first, linear section, ( $v_c$ ) defines the crack propagation rate in the stable stage. Because the maximum load and the specimen geometry were the same in all

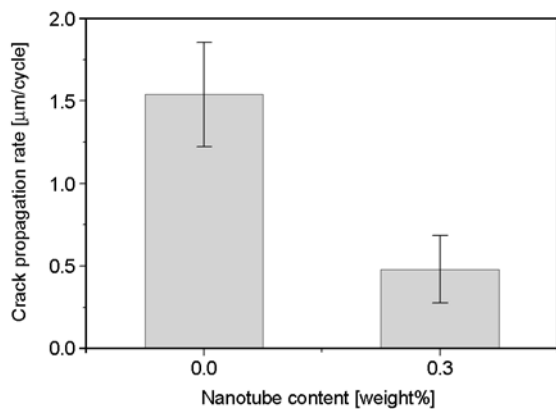


**Figure 10.** Comparison of the stable crack propagation rates of the 0 and 0.3 weight% nanotube content composites (data obtained from the test of 10–10 specimens)

cases during fatigue testing, the crack propagation rates can be compared. The comparison of the crack propagation rates of the composite and hybrid composite can be seen in Figure 10. (deviations in the figure correspond to double standard deviation).

According to the test results, the carbon nanotube reinforcement has decreased the crack propagation rate in the stable section by 69% compared to the composite not containing nanotubes.

With the crack propagation data the maximum cyclic strain energy release rate can be calculated by Equation (2) described in the ASTM 5528 standard:

$$G_{I_{max}} = \frac{3}{2} \frac{P_{max} \delta_{max}}{ab} \quad (2)$$

where  $P_{max}$  is the maximum load,  $\delta_{max}$  is the crack opening displacement at maximum load,  $a$  is the crack front position from measured from the point of loading,  $b$  is the specimen thickness.

The obtained  $G_{I_{max}}$  values at 6 different crack front positions in 5 mm steps in the whole failure process can be seen in Figure 11 (deviations in the figure correspond to double standard deviation).

According to the results the  $G_{I_{max}}$  values were in average 17% higher than in case of the composite without nanotubes. This can be explained by the lower crack opening displacement at a given load in case of the carbon nanotube reinforced composites. The crack opening displacement of a DCB specimen can be divided into two components. One of the components is the curved deformation of the delaminated specimen halves, the other is the deformation of the middle resin layer (Figure 12).

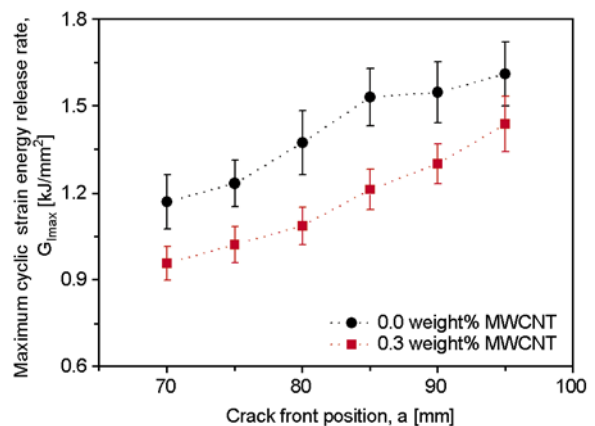


**Figure 11.** The maximum cyclic strain energy release rate values of the 0 and 0.3 weight% nanotube content composites at different crack front positions (data obtained from the test of 10–10 specimens)

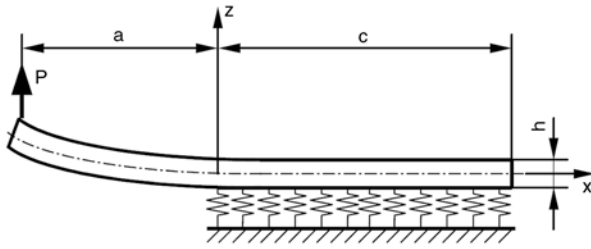


**Figure 12.** Mechanical half-model of a DCB specimen [32]

Previous tests showed no significant difference in the bending modulus of elasticity between the composites and the 0.3 weight% carbon nanotube reinforced composites [33], so the difference in the crack opening displacement of the DCB specimens during fatigue test can be mainly caused by the smaller deformation of the resin film. The stress peak emerging at the crack front at lower displacement will be lower in case of the carbon nanotube reinforced hybrid composites. This mechanism significantly decreases the rate of interlaminar crack propagation during fatigue testing. The individual  $G_{I\max}$  values give no information about the advancement of the failure process (which is the most important in fatigue testing), they can be only interpreted together with the crack propagation rate and cycles to failure values. The cycle to failure results (cycles elapsed to the complete split of the specimens) are presented in Figure 13 (deviations in the figure correspond to double standard deviation).

According to our results, although with high deviation (which is acceptable in case of interlaminar fatigue tests), 0.3 weight% carbon nanotube reinforcement has increased the cycles to failure of the composites significantly, to 3.8 times the cycles withstood by the composites without nanotubes.

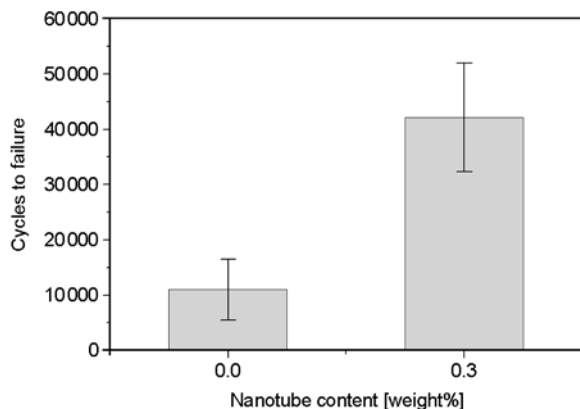


**Figure 13.** Cycles to failure of the 0 and 0.3 weight% nanotube content composites (data obtained from the test of 10–10 specimens)

#### 4. Conclusions

The aim of this study was to investigate the effect of carbon nanotube filling on the interlaminar fatigue properties of composite laminates. In our previous work it was demonstrated, that in static DCB tests the best interlaminar mechanical properties can be obtained at 0.3 weight% carbon nanotube filling, so this content has been selected for the fatigue tests. According to the fatigue test results it can be declared that with 0.3 weight% carbon nanotube filling of the matrix of a carbon fiber reinforced composite:

- the cycles to failure increased to 3.8 times the original value,
- the crack propagation rate decreased by 69%,
- the carbon nanotubes reinforced the interlaminar resin layer, which resulted in lower crack opening displacement at a given load, resulting in lower maximum cyclic strain energy release rate.

The test results showed, that even with the addition of 0.3 weight% proportion of carbon nanotubes a more fatigue resistant, reliable material can be produced.

Besides these results, we have developed a new acoustic emission localization based crack tracking algorithm, capable of the replacement of visual crack propagation tracking.

#### Acknowledgements

The authors are thankful for József Hári, Dr. Károly Renner, the BME Laboratory of Plastics and Rubber Technology and the Chemical Research Center of the Hungarian Academy of Sciences for the preparation of the TEM micrographs. This work was supported by Hungarian Scientific Research Fund (OTKA F67897). This work is connected to the scientific program of the ‘Development of quality-oriented and harmonized R+D+I strategy and functional model at BME’ project. This project is supported by the New Széchenyi Plan (Project ID: TÁMOP-4.2.1/B-09/1/KMR-2010-0002).

#### References

- [1] Kusaka T., Hojo M., Mai Y-W., Kurokawa T., Nojima T., Ochiai S.: Rate dependence of mode I fracture behaviour in carbon-fibre/epoxy composite laminates. *Composites Science and Technology*, **58**, 591–602 (1998). DOI: [10.1016/S0266-3538\(97\)00176-0](https://doi.org/10.1016/S0266-3538(97)00176-0)
- [2] Solaimurugan S., Velmurugan R.: Influence of in-plane fibre orientation on mode I interlaminar fracture toughness of stitched glass/polyester composites. *Composites Science and Technology*, **68**, 1742–1752 (2008). DOI: [10.1016/j.compscitech.2008.02.008](https://doi.org/10.1016/j.compscitech.2008.02.008)

- [3] Velmurugan R., Solaimurugan S.: Improvements in mode I interlaminar fracture toughness and in-plane mechanical properties of stitched glass/polyester composites. *Composites Science and Technology*, **67**, 61–69 (2007).  
DOI: [10.1016/j.compscitech.2006.03.032](https://doi.org/10.1016/j.compscitech.2006.03.032)
- [4] Pereira A. B., de Morais A. B., de Moura M. F. S. F., Magalhães A. G.: Mode I interlaminar fracture of woven glass/epoxy multidirectional laminates. *Composites Part A: Applied Science and Manufacturing*, **36**, 1119–1127 (2005).  
DOI: [10.1016/j.compositesa.2005.01.006](https://doi.org/10.1016/j.compositesa.2005.01.006)
- [5] Pereira A. B., de Morais A. B.: Mode I interlaminar fracture of carbon/epoxy multidirectional laminates. *Composites Science and Technology*, **64**, 2261–2270 (2004).  
DOI: [10.1016/j.compscitech.2004.03.001](https://doi.org/10.1016/j.compscitech.2004.03.001)
- [6] de Morais A. B., de Moura M. F., Marques A. T., de Castro P. T.: Mode-I interlaminar fracture of carbon/epoxy cross-ply composites. *Composites Science and Technology*, **62**, 679–686 (2002).  
DOI: [10.1016/S0266-3538\(01\)00223-8](https://doi.org/10.1016/S0266-3538(01)00223-8)
- [7] Arai M., Noro Y., Sugimoto K-I., Endo M.: Mode I and mode II interlaminar fracture toughness of CFRP laminates toughened by carbon nanofiber interlayer. *Composites Science and Technology*, **68**, 516–525 (2008).  
DOI: [10.1016/j.compscitech.2007.06.007](https://doi.org/10.1016/j.compscitech.2007.06.007)
- [8] Kostopoulos V., Tsotra P., Karapappas P., Tsantalis S., Vavouliotis A., Loutas T. H., Paipetis A., Friedrich K., Tanimoto T.: Mode I interlaminar fracture of CNF or/and PZT doped CFRPs via acoustic emission monitoring. *Composites Science and Technology*, **67**, 822–828 (2007).  
DOI: [10.1016/j.compscitech.2006.02.038](https://doi.org/10.1016/j.compscitech.2006.02.038)
- [9] Sadeghian R., Gangireddy S., Minaie B., Hsiao K-T.: Manufacturing carbon nanofibers toughened polyester/glass fiber composites using vacuum assisted resin transfer molding for enhancing the mode-I delamination resistance. *Composites Part A: Applied Science and Manufacturing*, **37**, 1787–1795 (2006).  
DOI: [10.1016/j.compositesa.2005.09.010](https://doi.org/10.1016/j.compositesa.2005.09.010)
- [10] Yokozeki T., Iwahori Y., Ishibashi M., Yanagisawa T., Imai K., Arai M., Takahashi T., Enomoto K.: Fracture toughness improvement of CFRP laminates by dispersion of cup-stacked carbon nanotubes. *Composites Science and Technology*, **69**, 2268–2273 (2009).  
DOI: [10.1016/j.compscitech.2008.12.017](https://doi.org/10.1016/j.compscitech.2008.12.017)
- [11] Davis D. C., Whelan B. D.: An experimental study of interlaminar shear fracture toughness of a nanotube reinforced composite. *Composites Part B: Engineering*, **42**, 105–116 (2011).  
DOI: [10.1016/j.compositesb.2010.06.001](https://doi.org/10.1016/j.compositesb.2010.06.001)
- [12] Seyhan A. T., Tanoglu M., Schulte K.: Mode I and mode II fracture toughness of E-glass non-crimp fabric/carbon nanotube (CNT) modified polymer based composites. *Engineering Fracture Mechanics*, **75**, 5151–5162 (2008).  
DOI: [10.1016/j.engfracmech.2008.08.003](https://doi.org/10.1016/j.engfracmech.2008.08.003)
- [13] Wicks S. S., de Villoria R. G., Wardle B. L.: Interlaminar and intralaminar reinforcement of composite laminates with aligned carbon nanotubes. *Composites Science and Technology*, **70**, 20–28 (2010).  
DOI: [10.1016/j.compscitech.2009.09.001](https://doi.org/10.1016/j.compscitech.2009.09.001)
- [14] Li Y., Hori N., Arai M., Hu N., Liu Y., Fukunaga H.: Improvement of interlaminar mechanical properties of CFRP laminates using VGCF. *Composites Part A: Applied Science and Manufacturing*, **40**, 2004–2012 (2009).  
DOI: [10.1016/j.compositesa.2009.09.002](https://doi.org/10.1016/j.compositesa.2009.09.002)
- [15] Siddiqui N. A., Woo R. S. C., Kim J-K., Leung C. C. K., Munir A.: Mode I interlaminar fracture behavior and mechanical properties of CFRPs with nanoclay-filled epoxy matrix. *Composites Part A: Applied Science and Manufacturing*, **38**, 449–460 (2007).  
DOI: [10.1016/j.compositesa.2006.03.001](https://doi.org/10.1016/j.compositesa.2006.03.001)
- [16] Phonthammachai N., Li X., Wong S., Chia H., Tjiu W. W., He C.: Fabrication of CFRP from high performance clay/epoxy nanocomposite: Preparation conditions, thermal–mechanical properties and interlaminar fracture characteristics. *Composites Part A: Applied Science and Manufacturing*, **42**, 881–887 (2011).  
DOI: [10.1016/j.compositesa.2011.02.014](https://doi.org/10.1016/j.compositesa.2011.02.014)
- [17] Xu Y., Hoa S. V.: Mechanical properties of carbon fiber reinforced epoxy/clay nanocomposites. *Composites Science and Technology*, **68**, 854–861 (2008).  
DOI: [10.1016/j.compscitech.2007.08.013](https://doi.org/10.1016/j.compscitech.2007.08.013)
- [18] Ye Y., Chen H., Wu J., Chan C. M.: Interlaminar properties of carbon fiber composites with halloysite nanotube-toughened epoxy matrix. *Composites Science and Technology*, **71**, 717–723 (2011).  
DOI: [10.1016/j.compscitech.2011.01.018](https://doi.org/10.1016/j.compscitech.2011.01.018)
- [19] Argüelles A., Viña J., Canteli A. F., Castrillo M. A., Bonhomme J.: Interlaminar crack initiation and growth rate in a carbon-fibre epoxy composite under mode-I fatigue loading. *Composites Science and Technology*, **68**, 2325–2331 (2008).  
DOI: [10.1016/j.compscitech.2007.09.012](https://doi.org/10.1016/j.compscitech.2007.09.012)
- [20] Hojo M., Ando T., Tanaka M., Adachi T., Ochiai S., Endo Y.: Modes I and II interlaminar fracture toughness and fatigue delamination of CF/epoxy laminates with self-same epoxy interleaf. *International Journal of Fatigue*, **28**, 1154–1165 (2006).  
DOI: [10.1016/j.ijfatigue.2006.02.004](https://doi.org/10.1016/j.ijfatigue.2006.02.004)
- [21] Hojo M., Matsuda S., Tanaka M., Ochiai S., Murakami A.: Mode I delamination fatigue properties of interlayer-toughened CF/epoxy laminates. *Composites Science and Technology*, **66**, 665–675 (2006).  
DOI: [10.1016/j.compscitech.2005.07.038](https://doi.org/10.1016/j.compscitech.2005.07.038)



- [22] Boudenot J-C.: New concepts for nanophotonics and nano-electronics: From transistor to nanotube. *Comptes Rendus Physique*, **9**, 41–52 (2008).  
DOI: [10.1016/j.crhy.2007.12.002](https://doi.org/10.1016/j.crhy.2007.12.002)
- [23] Kannan A. M., Kanagala P., Veedu V.: Development of carbon nanotubes based gas diffusion layers by *in situ* chemical vapor deposition process for proton exchange membrane fuel cells. *Journal of Power Sources*, **192**, 297–303 (2009).  
DOI: [10.1016/j.jpowsour.2009.03.022](https://doi.org/10.1016/j.jpowsour.2009.03.022)
- [24] Avilés F., Cauch-Rodríguez J. V., Rodríguez-González J. A., May-Pat A.: Oxidation and silanization of MWCNTs for MWCNT/vinyl ester composites. *Express Polymer Letters*, **5**, 766–776 (2011).  
DOI: [10.3144/expresspolymlett.2011.75](https://doi.org/10.3144/expresspolymlett.2011.75)
- [25] Zhang Z., Peng K., Chen Y.: Mechanical performance of ozone functionalized MWCNTs/PC nanocomposites. *Express Polymer Letters*, **5**, 516–525 (2011).  
DOI: [10.3144/expresspolymlett.2011.50](https://doi.org/10.3144/expresspolymlett.2011.50)
- [26] Romhány G., Szabényi G.: Interlaminar crack propagation in MWCNT/fiber reinforced hybrid composites. *Express Polymer Letters*, **3**, 145–151 (2009).  
DOI: [10.3144/expresspolymlett.2009.19](https://doi.org/10.3144/expresspolymlett.2009.19)
- [27] Ren Y., Li F., Cheng H-M., Liao K.: Tension–tension fatigue behavior of unidirectional single-walled carbon nanotube reinforced epoxy composite. *Carbon*, **41**, 2177–2179 (2003).  
DOI: [10.1016/S0008-6223\(03\)00248-3](https://doi.org/10.1016/S0008-6223(03)00248-3)
- [28] Ren Y., Fu Y. Q., Liao K., Li F., Cheng H. M.: Fatigue failure mechanisms of single-walled carbon nanotube ropes embedded in epoxy. *Applied Physics Letters*, **84**, 2811–2813 (2004).  
DOI: [10.1063/1.1703837](https://doi.org/10.1063/1.1703837)
- [29] Zhang W., Picu R. C., Koratkar N.: Suppression of fatigue crack growth in carbon nanotube composites. *Applied Physics Letters*, **91**, 193109/1–193109/3 (2007).  
DOI: [10.1063/1.2809457](https://doi.org/10.1063/1.2809457)
- [30] Grimmer C. S., Dharan C. K. H.: High-cycle fatigue of hybrid carbon nanotube/glass fiber/polymer composites. *Journal of Materials Science*, **43**, 4487–4492 (2008).  
DOI: [10.1007/s10853-008-2651-9](https://doi.org/10.1007/s10853-008-2651-9)
- [31] Romhány G., Szabényi G.: Preparation of MWCNT reinforced epoxy nanocomposite and examination of its mechanical properties. *Plastics, Rubber and Composites*, **37**, 214–218 (2008).  
DOI: [10.1179/174328908X309376](https://doi.org/10.1179/174328908X309376)
- [32] Szekrényes A.: Delamination of composite specimens. PhD thesis, BME, Faculty of Mechanical Engineering, Department of Applied Mechanics (2005).
- [33] Romhány G., Szabényi G.: Preparation of MWCNT/carbon fabric reinforced hybrid nanocomposite and examination of its mechanical properties. *Materials Science Forum*, **589**, 269–274 (2008).  
DOI: [10.4028/www.scientific.net/MSF.589.269](https://doi.org/10.4028/www.scientific.net/MSF.589.269)

# Fracture resistance of rubbers with MWCNT, organoclay, silica and carbon black fillers as assessed by the J-integral: Effects of rubber type and filler concentration

S. Agnelli<sup>1\*</sup>, G. Ramorino<sup>1</sup>, S. Passera<sup>1</sup>, J. Karger-Kocsis<sup>2</sup>, T. Riccò<sup>1</sup>

<sup>1</sup>Dipartimento di Ingegneria Meccanica e Industriale, Facoltà di Ingegneria, Università degli Studi di Brescia, via Branze 38, I-25123 Brescia, Italy

<sup>2</sup>Department of Polymer Engineering, Faculty of Mechanical Engineering, Budapest University of Technology and Economics, H-1111 Budapest, Hungary

Received 3 November 2011; accepted in revised form 30 January 2012

**Abstract.** The fracture resistance of different rubbers containing various nanofillers, such as multiwall carbon nanotube (MWCNT), organoclay, silica and carbon black (CB), was determined by the J-integral making use of the single edge notched tensile loaded (SEN-T) single specimen approach. The elastomeric matrices were natural (NR), ethylene propylene diene (EPDM) and hydrogenated nitrile rubbers (HNBR). Moreover, the strain softening (Payne effect) of selected rubbers with 30 part per hundred rubber (phr) filler content was also investigated by dynamic mechanical thermal analysis (DMTA) in shear mode. DMTA results indicated that the Payne effect follows the ranking: MWCNT(fibrous) > organoclay(plate) > silica(spherical). J-resistance ( $J_R$ ) curves were constructed by plotting the  $J$  value as a function of the crack tip opening displacement (CTOD\*), monitored during loading. CTOD\* = 0.1 mm was considered as crack initiation threshold and thus assigned to the critical value  $J_{Ic}$ .  $J_{Ic}$  increased with increasing filler loading, whereby MWCNT outperformed both silica and CB. On the other hand,  $J_{Ic}$  did not change with filler loading for the NR/organoclay systems that was traced to strain-induced crystallization effect in NR. The tearing modulus ( $T_J$ ) also increased with increasing filler loading. The related increase strongly depended on both rubber and filler types. Nonetheless, the most prominent improvement in  $T_J$  among the fillers studied was noticed for the fibrous MWCNT.

**Keywords:** rubber, nanocomposite, fracture mechanics, J-resistance curve

## 1. Introduction

The use of novel nanoparticles in rubber compounding is one of the latest trends in the development of elastomeric materials. Nanofillers such as carbon nanotubes (CNT), organophilic modified clays are very attractive because they can improve mechanical, thermal and physical properties even in small amounts, once provided that a good dispersion in the matrix is obtained and a good matrix-filler interaction is achieved [1–3]. In fact if the filler is dispersed on a nanometer scale, its surface area is increased so much that its efficiency exceeds

that of conventional non-active fillers. On the other hand, the effect of the novel nanofillers is somewhat similar to those of the traditional active fillers, i.e. silica and carbon black (CB).

Among nanofillers, CNTs are very promising for their outstanding mechanical properties and for their high thermal and electrical conductivity. On the other side, when used as fillers in a polymeric matrix, difficulties rise in obtaining a good CNT dispersion with common processing technologies. Multiwall carbon nanotube (MWCNT) reinforced composites are widely investigated in literature,

\*Corresponding author, e-mail: [silvia.agnelli@ing.unibs.it](mailto:silvia.agnelli@ing.unibs.it)

and although a large body of work has already been done on mechanical properties of MWCNT filled elastomers [1, 2], their fracture behaviour is still unexplored.

This work is aimed at investigating the reinforcing effect promoted by MWCNT, organoclay, silica and CB nanoparticles on fracture resistance of various rubbers. The elastomeric matrices selected were: natural rubber (NR), ethylene propylene diene (EPDM), and hydrogenated nitrile butadiene rubber (HNBR). NR was filled with organoclay, EPDM with CB and HNBR both with MWCNT and silica. In all systems the amount of filler has been varied. The fracture resistance of the various materials was studied by using the J-integral which is a fracture mechanical approach. The single specimen J-testing methodology was recently adapted for rubbers [4, 5]. Fracture mechanics parameters describe quantitatively the material resistance to fracture in the presence of flaws or defects, and  $J$  parameter can be defined as the energy required per unit area to create new fracture surfaces. The peculiar feature of the J-testing is that one can get information on both the resistance to crack initiation and to propagation in the materials.

## 2. Experimental

### 2.1. Materials

The sulphur-cured NR (SMR-GP) was filled with different amounts of an organoclay consisting in montmorillonite modified with dimethyl dihydrogenated tallow ammonium salt and with an organic content of 40 wt% (Dellite 67G, produced by Laviosa Chimica Mineraria SpA (Livorno, Italy)). The following amounts of organoclay were added in the NR matrix: 0, 6.5, 14 and 30 parts per hundred rubber (phr). The preparation and the recipe of NR-based nanocomposites, kindly prepared and supplied by Pirelli SpA (Milan, Italy), were published in ref. [5–7]. The sulphur-cured EPDM rubber was filled with different amounts of CB N550 type. CB was added in 0, 30, 45 and 60 phr in the related recipes the preparation of which was disclosed earlier [8]. The peroxide cured HNBR contained two different amounts (viz. 10 and 30 phr) of silica nanoparticles or MWCNTs, respectively. Silica under the trade name Ultrasil VN2 was procured from Evonik-Degussa (Essen, Germany), whereas the MWCNT (Baytubes C 150 P) was supplied by

**Table 1.** Summary of matrices and filler types and contents of the materials studied

Matrix	Filler type	Filler contents [phr]
HNBR	Silica	0; 10; 30
HNBR	MWCNTs	0; 10; 30
EPDM	CB	0; 30; 45; 60
NR	Organoclay	0; 6.5; 14; 30

Bayer MaterialScience (Leverkusen, Germany). The composition and preparation of the HNBR-based systems were already published [9, 10]. The materials for testing were available form of ca. 2 mm thick vulcanized plates. A summary of matrices and fillers of all the materials shown is reported in Table 1.

### 2.2. Tests

Preliminarily, some basic mechanical properties were measured at low strains, in order to provide additional information about of the different mechanical behavior of the various materials. Tensile tests were performed on CB filled EPDM rubbers, to evaluate the stress-strain curves of the material and measure the initial modulus. Such tests were carried out by an Instron dynamometer (Model 3366, INSTRON, Norwood, Massachusetts, USA), at the crosshead speed of 5 mm/min on 10 mm large and 2 mm thick strips, with a gauge length of 60 mm. Due to the small amount of material available, the HNBR based composites were not characterized by tensile tests, but by dynamic mechanical tests, performed in shear mode, at room temperature, at the frequency of 1 Hz in a shear strain amplitude range between 0.001 and 0.1. These tests were performed by a dynamic-mechanical thermal analyser (DMTA) by Polymer-Lab Ltd. (Loughborough, UK). The aim behind dynamic mechanical tests was merely a basic characterization of the mechanical behavior of such materials (stiffness at low strains, non-linearity effects, dissipative properties), completely unrelated to the results of fracture tests shown in this work. Fracture tests are performed on single edge notched in tension loaded (SENT) specimens (see Figure 1a).

The width ( $W$ ) is 25 mm, the thickness ( $B$ ) is 2 mm, the gauge length ( $L$ ) is 50 mm and the initial crack length ( $a_0$ ) to width ratio was 0.4. Such dimensions were chosen on the basis of a previous work aimed at optimizing the geometry factor [5]. The notch is introduced by an industrial blade and then sharp-

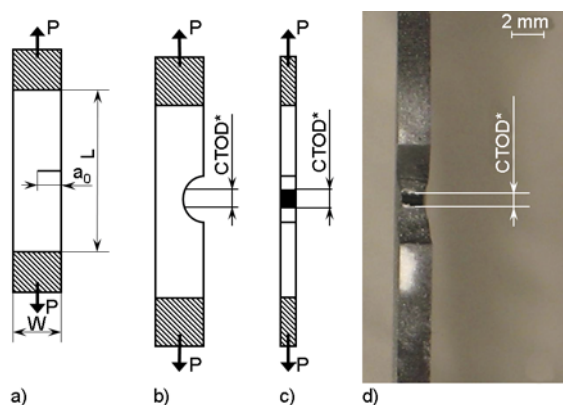


**Figure 1.** a) geometry of SENT specimen used for fracture tests; b), c) schematic representation of the loaded specimen in a lateral and a frontal view, respectively; d) photo of the crack tip of a specimen of HNBR filled with 10 phr MWCNTs in a frontal view; CTOD\* is indicated

ened by sliding a razor blade at the notch tip. Tests were carried out by an Instron dynamometer (the same used for tensile tests), at the crosshead speed of 2 mm/min at room temperature. The fracture testing methodology employed was introduced in details in ref. [5]. Recall that this J-testing methodology allows us to detect the fracture initiation point from which the material resistance to crack initiation ( $J_{Ic}$ ) can be deduced, and also to assess the stable crack propagation by constructing the J-resistance curve, and all this by testing only one specimen. Practically, while the load-displacement data are recorded, a photo camera takes a sequence of photos of the crack tip, one every 5 seconds. The camera is positioned in front of the crack in order to focus on the internal surfaces of the crack. A schematic representation of a specimen during the fracture process is shown in fig. 1, both from a lateral view (Figure 1b) and from the corresponding frontal view (Figure 1c), while Figure 1d shows a real picture taken to the specimen in a frontal view. The crack surfaces are coated by a contrast powder (e.g.: talc for black materials) before the test and therefore the new fracture surfaces can be easily recognised because of the contrast between the colour of rubber and the colour of the powder. By analysing such photos the point where fracture begins to propagate can be detected, and the  $J$  value corresponding to the onset of fracture ( $J_{Ic}$ ) can be evaluated by Equation (1):

$$J = \frac{\eta \cdot U}{B \cdot (W - a_0)} \quad (1)$$

where  $U$  is energy, evaluated as the area under the load-displacement curve up to the point considered, and  $\eta$  is a geometry factor, equal to 0.9 [5]. The resistance of the specimen to fracture propagation is characterized by the J-resistance curve, which relates  $J$ , evaluated by the loading curve following Equation (1), to the crack advancement ( $\Delta a$ ) during the phase of stable crack advancement. However, high deformability of rubbers makes impossible to monitor the actual crack advancement during the test. The methodology followed in this work relates  $J$  values to the crack tip opening displacement, CTOD\*, at different times during the fracture process. CTOD\* is related to the crack advancement, and can be therefore considered as an indirect measurement of  $\Delta a$ . CTOD\* is measured on the pictures taken to the crack tip in a frontal view, where the extension of the opening at the crack tip (CTOD\*) due to the creation of the new fracture surfaces is evidenced by the contrast of the different colors of rubber and coating powder. An example of CTOD\* measurement is shown in Figure 1c and 1d. In the present work the correlation between CTOD\* and  $\Delta a$  was not analyzed. A CTOD\*- $\Delta a$  calibration curve was however obtained by the authors for a CB filled HNBR by a multi-specimen procedure. The result, shown in ref. [11], evidenced that CTOD\* was linearly dependent on  $\Delta a$  in the first stage of the fracture process of the elastomeric system investigated. It should be pointed out that often it was not possible to identify unequivocally the onset of crack advancement, but rather a gradual transition was observed from the phase of deformation to the phase of fracture at the crack tip. For this reason the initiation point was rendered to CTOD\* = 0.1 mm (through the whole thickness). Each fracture test was repeated three times.

### 3. Results and discussion

The storage shear ( $G'$ ) and the loss shear modulus ( $G''$ ) resulting from the DMTA tests are plotted in Figure 2 and 3, respectively, as a function of the shear strain amplitude for the NR and HNBR with and without 30 phr additives.

$G'$  and  $G''$  of neat HNBR are indicated by full squares, while full circles and full triangles indicate HNBR filled with 30 phr of silica and 30 phr of MWCNTs, respectively. From Figure 2 it can be pointed out that at low strains the filled systems dis-



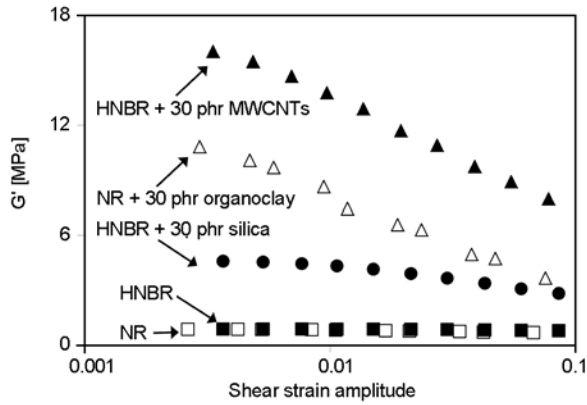


**Figure 2.** Dynamic storage modulus in shear mode at 1 Hz plotted against strain amplitude for HNBR- and NR- nanocomposites at 0 and 30 phr of filler content

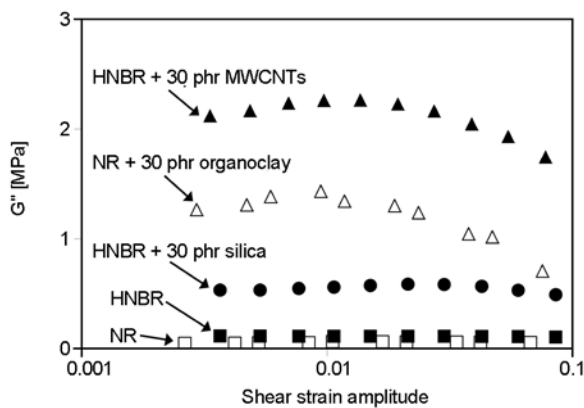


**Figure 3.** Dynamic loss modulus in shear mode at 1 Hz plotted against strain amplitude for HNBR- and NR-nanocomposites at 0 and 30 phr of filler content

play the typical non-linear behaviour (Payne effect) that consists in a decrease of the storage modulus with increasing strain amplitude. MWCNTs-filled system exhibits a stronger stiffening effect and a larger non-linearity effect compared to silica-filled HNBR. The storage and loss moduli obtained for NR and NR with 30 phr organoclay are taken from ref. [6]. It is interesting to notice that, although the matrices have similar storage moduli, MWCNT improves the stiffness of HNBR far more than organoclay at the same filler loading (30 phr). For example, by considering the storage moduli at 0.003 of shear strain amplitude, it turns out that 30 phr of silica improves 5 times the stiffness of its matrix, organoclay 13 times and MWCNTs 18 times. This efficiency of MWCNT is most probably linked with its dispersion and high aspect ratio. Further, MWCNTs are found to induce in the matrix the highest increase of energy dissipation, with respect to the

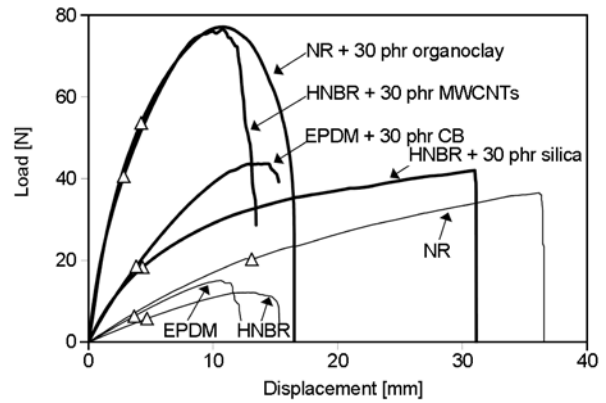


**Figure 4.** Load-displacement curves obtained from fracture tests on composites filled with 30 phr of fillers (thick lines) and of the corresponding neat matrixes (HNBR, NR and EPDM rubber, thin lines). Open triangles indicate the point at  $CTOD^* = 0.1$  mm

other fillers investigated: this effect can be observed by the behaviour of the loss modulus vs strain amplitude plotted in Figure 3.

Tensile tests carried out on EPDM based rubbers provided the following elastic moduli, evaluated as the slope of the stress-strain curve at very small tensile strains:  $1.7 \pm 0.05$ ,  $4.7 \pm 0.20$ ,  $7.1 \pm 0.09$  and  $8.4 \pm 0.20$  MPa for EPDM filled with 0, 30, 45 and 60 phr of CB, respectively.

The raw results obtained from fracture mechanics tests are the load-displacement curves. Figure 4 shows characteristic load vs displacement traces obtained from fracture tests on SENT specimens of different materials: the neat matrices (EPDM and HNBR) and the samples filled with 30 phr of nanofiller, EPDM with CB, HNBR with silica and MWCNTs. The curves of NR and NR filled with 30 phr organoclay, obtained under the same experimental conditions [5], were inserted in Figure 4 for sake of comparison. The points of fracture initiation, assigned to  $CTOD^* = 0.1$  mm, are displayed on the curves by open triangles.

By considering the curves of the neat matrices, it can be observed that at small displacement values all the three materials have a similar behaviour, but NR shows a maximum displacement that exceeds more than twice those of the other matrices. Also the onset of fracture of NR occurs at a higher displacement than for the unfilled HNBR and EPDM rubbers. By the comparison of the curves of MWCNT and nano-silica filled HNBR, it can be seen from the initial slope of these curves that MWCNTs enhance the stiffness of HNBR speci-

men more than silica nanoparticles. This result is in agreement with the trend of  $G'$  values at small strains obtained by DMTA experiments. Further, although MWCNT filling increases the maximum load reached during the test, the maximum displacement is reduced with respect to the matrix. This is characteristic for discontinuous fibrous reinforcements in all polymer composites. By contrast, the silica nanoparticles cause an increase of the maximum displacement. By observing the load-displacement curve related to the EPDM rubber filled with CB, it appears that 30 phr of CB within EPDM produces the same fracture behaviour as silica within HNBR, until the point of fracture initiation. With reference to NR filled with organoclay, surprisingly its loading curve follows faithfully that of HNBR reinforced by MWCNTs, though the onset of fracture of the NR system occurs at a larger displacement.

$J_{Ic}$  values, evaluated by Equation (1) at  $CTOD^* = 0.1$  mm and averaged over the results of three tests, are reported in Figure 5. The results of HNBR filled with silica nanoparticles (open circles) and MWCNTs (black circles), CB filled EPDM rubber (full triangles) and organoclay filled NR (full squares) [5] are plotted in Figure 5 as a function of the filler content.

Figure 5 provides an interesting comparison of  $J_{Ic}$  values obtained for various rubbers containing different fillers. It can be seen that neat HNBR and EPDM rubber (see values at 0 phr filler content) have a comparable fracture resistance. At 10 phr filler, MWCNTs increase fracture resistance of HNBR slightly more than silica nanoparticles do. However, the fracture resistance of HNBR filled with 30 phr MWCNTs outperforms both that of

HNBR with 30 phr silica and that of EPDM with 30 phr CB. Moreover, by comparing the HNBR/MWCNTs and EPDM/CB systems, the results clearly indicate that a substantially higher amount of CB than MWCNT is required to achieve a comparable level of fracture resistance. It also turns out that the fracture resistance of MWCNTs filled HNBR is comparable to that of NR filled with 30 phr organoclay. It is worthwhile to note that the fracture resistance of NR-based systems can be strongly influenced by strain-induced crystallization, and thus it cannot be only attributed to reinforcing effect of the filler. In fact  $J_{Ic}$  of NR is practically not affected by the incorporation of organoclay up to a content of 30 phr, which could be linked to a dominant effect of strain-induced crystallization. This hypothesis is supported by literature works, that analyze the significant fracture resistance enhancement of NR-based systems promoted by strain induced crystallization (see for example ref. [12]).

Further, the fracture resistance of HNBR and EPDM based systems was analysed during the process of fracture propagation. As described in the experimental section,  $J$  values are calculated for several points on the load-displacement curve after the onset of fracture and the corresponding  $CTOD^*$  values are measured on the photos of the crack tip taken during the fracture test. Some examples of  $J$  vs  $CTOD^*$  curves ( $J_R$  curves) are shown in Figure 6, where  $J_R$  curves of the neat matrices, HNBR and EPDM, and of the corresponding composites added with 30 phr filler are compared. It can be observed that  $J_R$  curves of the matrices are almost overlapping, and the curve referred to the 30 phr CB filled EPDM is very close to that of the 30 phr silica filled HNBR sample. By contrast, it appears that at 30 phr

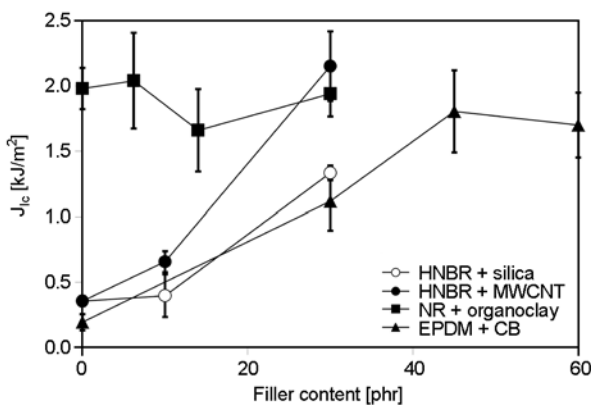


Figure 5.  $J_{Ic}$  vs filler content for the various elastomeric composites investigated

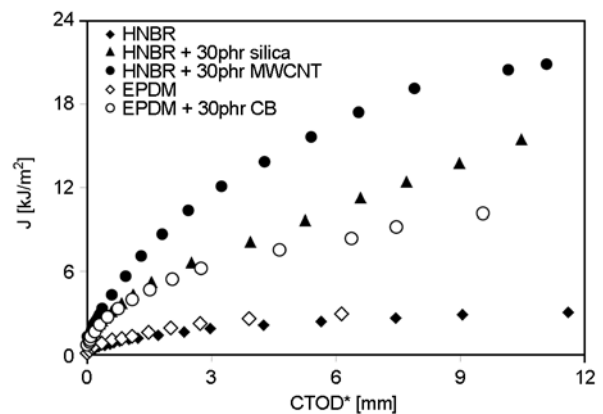


Figure 6.  $J$ -resistance curves of HNBR- and EPDM- based nanocomposites

filler content HNBR with MWCNTs achieves higher levels of  $J$  with respect to the other systems filled with CB or silica. This underlines the higher efficiency of MWCNTs, with respect to the other fillers, in enhancing the resistance to both fracture initiation and propagation.

It must be pointed out that a reliable comparison of  $J$  values of the different materials during fracture propagation should be performed at the same crack advancement, whereas  $CTOD^*$  parameter, used to plot  $J_R$  curves in this work, though related to  $\Delta a$ , is also dependent on the elastic properties of the material. However, it is still possible to compare the resistance to fracture propagation of materials with different deformability by the slope of the  $J_R(CTOD^*)$  curve at  $CTOD^* = 0$  mm. Then a  $T_J$  parameter, termed tearing modulus, as proposed in [5] is defined as Equation (2):

$$T_J = \left. \frac{dJ}{d(CTOD^*)} \right|_{CTOD^*=0} \quad (2)$$

By this parameter the resistance to fracture propagation of different materials is evaluated at the same stage of the fracture process, i.e. at the very beginning of the process.

Figure 7 shows the values of the tearing modulus plotted as a function of the filler content, for the various rubber based composites.  $T_J$  values of NR filled with organoclay systems published in ref. [5] are also shown for comparison.

Concerning HNBR based systems, MWCNTs show a higher efficiency in improving the resistance to fracture propagation with respect to silica nanoparticles, since they increase the tearing modulus, as previously defined, even at low filler contents. Note that MWCNTs increase three times the tearing

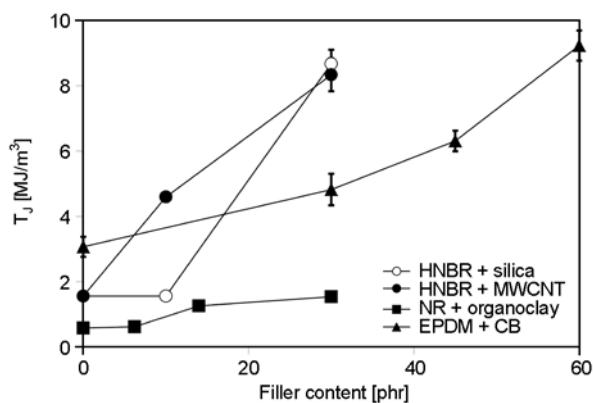


Figure 7. Tearing modulus,  $T_J$ , vs filler content for the various elastomeric composites investigated

modulus of HNBR at 10 phr loading, while the effect of silica at the same filler content is negligible. Figure 7 indicates that  $T_J$  value of NR, which is lower than that of the other neat rubbers analysed, is only slightly increased by the addition of the organoclay. This is a further, however, still indirect confirmation on the large effect of strain-induced crystallization which does not take place at this stage. One can see that CB increases remarkably the  $T_J$  values of EPDM rubber only at high filler contents. A least 30 phr of CB is required to increase the resistance to crack propagation of the EPDM rubber in order to reach the same level produced by 10 phr of MWCNT in HNBR. Thus, the results of Figure 7 evidence as a whole the high efficiency of MWCNTs to enhance the resistance of elastomeric systems to crack propagation.

#### 4. Conclusions

This work was devoted to characterize the strain softening and the fracture resistance of elastomer based nanocomposites making use of the J-integral approach. The rubber matrices, viz. NR, EPDM and HNBR, were filled with various amounts of MWCNT, organoclay, silica and CB.

While the matrices showed similar shear modulus-shear strain traces, the storage modulus of the composite containing MWCNT exhibited larger non-linearity and stronger reinforcing effect in the whole range of strain amplitude explored than organoclay and silica.

Results from the single-specimen J-testing methodology highlighted that MWCNT is the most efficient filler with respect to both crack initiation and propagation. Accordingly, similar fracture resistance data, i.e.  $J_{Ic}$  and  $T_J$  values, can be obtained with smaller amounts of MWCNT than with other fillers.

Although this investigation was not extensively developed by systematically varying material composition and morphology, the results bring to light that the J-testing methodology used is a straightforward tool to check recipe related changes with respect to crack initiation and propagation resistance.

#### References

- [1] Thomas S., Stephen R.: Rubber nanocomposites: Preparation, properties and applications. Wiley, Singapore (2010).

- [2] Mittal V., Kim J. K., Pal K.: Recent advances in elastomeric nanocomposites. Springer, Berlin (2011).
- [3] Galimberti M.: Rubber-clay nanocomposites. Wiley-VCH, Weinheim (2011).
- [4] Reincke K., Grellmann W., Heinrich G.: Investigation of mechanical and fracture mechanical properties of elastomers filled with precipitated silica and nanofillers based upon layered silicates. Rubber Chemistry and Technology, **77**, 662–677 (2004). DOI: [10.5254/1.3547843](https://doi.org/10.5254/1.3547843)
- [5] Ramorino G., Agnelli S., De Santis R., Riccò T.: Investigation of fracture resistance of natural rubber/clay nanocomposites by *J*-testing. Engineering Fracture Mechanics, **77**, 1527–1536 (2010). DOI: [10.1016/j.engfracmech.2010.04.021](https://doi.org/10.1016/j.engfracmech.2010.04.021)
- [6] Ramorino G., Bignotti F., Conzatti L., Ricco T.: Dynamic and viscoelastic behavior of natural rubber/layered silicate nanocomposites obtained by melt blending. Polymer Engineering and Science, **47**, 1650–1657 (2007). DOI: [10.1002/pen.20849](https://doi.org/10.1002/pen.20849)
- [7] Ramorino G., Bignotti F., Pandini S., Riccò T.: Mechanical reinforcement in natural rubber/organoclay nanocomposites. Composites Science and Technology, **69**, 1206–1211 (2009). DOI: [10.1016/j.compscitech.2009.02.023](https://doi.org/10.1016/j.compscitech.2009.02.023)
- [8] Xu D., Karger-Kocsis J., Schlarb A. K.: Rolling wear of EPDM and SBR rubbers as a function of carbon black contents: Correlation with microhardness. Journal of Materials Science, **43**, 4330–4339 (2008). DOI: [10.1007/s10853-008-2637-7](https://doi.org/10.1007/s10853-008-2637-7)
- [9] Felhős D., Karger-Kocsis J., Xu D.: Tribological testing of peroxide cured HNBR with different MWCNT and silica contents under dry sliding and rolling conditions against steel. Journal of Applied Polymer Science, **108**, 2840–2851 (2008). DOI: [10.1002/app.27624](https://doi.org/10.1002/app.27624)
- [10] Xu D., Karger-Kocsis J., Schlarb A. K.: Friction and wear of HNBR with different fillers under dry rolling and sliding conditions. Express Polymer Letters, **3**, 126–136 (2009). DOI: [10.3144/expresspolymlett.2009.16](https://doi.org/10.3144/expresspolymlett.2009.16)
- [11] Agnelli S., Baldi F., Riccò T.: A tentative application of the energy separation principle to the determination of the fracture resistance ( $J_{Ic}$ ) of rubbers. Engineering Fracture Mechanics, in press (2012).
- [12] Lee D. J., Donovan J. A.: Microstructural changes in the crack tip region of carbon-black-filled natural rubber. Rubber Chemistry and Technology, **60**, 910–923 (1987). DOI: [10.5254/1.3536164](https://doi.org/10.5254/1.3536164)



# Novel blends of acrylonitrile butadiene rubber and polyurethane-silica hybrid networks

J. H. Tan<sup>1</sup>, X. P. Wang<sup>1,2\*</sup>, J. J. Tai<sup>1</sup>, Y. F. Luo<sup>1</sup>, D. M. Jia<sup>1</sup>

<sup>1</sup>School of Materials Science and Engineering, South China University of Technology, 510640 Guangzhou, China

<sup>2</sup>State Key Laboratory of Subtropical Building Science, South China University of Technology, 510640 Guangzhou, China

Received 23 November 2011; accepted in revised form 31 January 2012

**Abstract.** Novel blends of acrylonitrile butadiene rubber (NBR) and polyurethane-silica (PU-SiO<sub>2</sub>) hybrid networks have been prepared by melt blending. The PU-SiO<sub>2</sub> hybrid networks were formed via the reaction of NCO groups of NCO-terminated PU prepolymer and OH groups of SiO<sub>2</sub> in the absence of an external crosslinking agent (i.e. alcohols and amines) during the curing process of NBR. Both in the neat PU-SiO<sub>2</sub> system and the NBR/(PU-SiO<sub>2</sub>) system, the NCO-terminated PU prepolymer could be crosslinked by SiO<sub>2</sub> to form PU-SiO<sub>2</sub> hybrid networks. The effects of PU-SiO<sub>2</sub> introduction into the NBR, on the properties of the resulting blends were studied. It was found that the vulcanization was activated by the incorporation of PU-SiO<sub>2</sub>. Transmission electronic microscopy (TEM) studies indicated that the interpenetration and entanglement structures between NBR and PU-SiO<sub>2</sub> increased with increasing PU-SiO<sub>2</sub> content and the quasi-interpenetrating polymer networks (quasi-IPN) structures were formed when the PU-SiO<sub>2</sub> was 50 wt% in the NBR/(PU-SiO<sub>2</sub>) systems. The microstructures formed in the blends led to good compatibility between NBR and PU-SiO<sub>2</sub> and significantly improved the mechanical properties, abrasion resistance and flex-fatigue life of the blends.

**Keywords:** polymer blends and alloys, acrylonitrile butadiene rubber, polyurethane, silica, hybrid materials

## 1. Introduction

Polymer blends have been of great interest particularly in the last two decades or so. The factors that have fueled this interest are cost and time associated with the development of new polymers and the ability to tailor properties by blending, which may result in new, desirable and, in some cases, unexpected synergistic effects on the properties [1, 2].

Acrylonitrile butadiene rubber (NBR) possesses attractive properties, such as good oil resistance, abrasion resistance, elastic properties and low gas permeability, and is widely applied in a wide range of industrial equipment. However, the mechanical properties, ozone resistance and processibility of NBR are poor [3]. Fillers such as silica, carbon and clay are usually added to improve its mechanical

strength [4–7]. However, the addition of fillers has some limitations and desired properties cannot be achieved. The blending of NBR with another polymer can overcome these limitations.

Polyurethane (PU) is applied in many different fields because of its excellent properties, including its high tensile modulus, abrasion resistance, tear resistance, chemical resistance, low-temperature elasticity as well as ease of processing [8, 9]. The favorable properties of PU have raised interest in preparing NBR/PU blends, which can bring to NBR the valuable properties of PU, especially the high strength and excellent abrasion resistance. The applications of different forms of PU in NBR have been reported. Direct blending hydrothermal decomposed crosslinked PU (HD-PUR) or thermoplastic

\*Corresponding author, e-mail: [wangxp@scut.edu.cn](mailto:wangxp@scut.edu.cn)

PU (TPU) with NBR can obtain NBR/PU blends [10–12]. However, these blends generally exhibit poor mechanical properties because of incompatibility and phase separation of the initial components. In order to minimize phase separation and increase interfacial adhesion, compatilizers usually are used for these systems, but this would lead to the increased cost and entail the use of complicated procedures. Dynamically cured TPU and NBR blends were prepared by Tang *et al.* [13]. They reported that the mechanical properties for these NBR/TPU dynamically cured blends were much better than those for NBR/TPU simple blend systems. However, in the NBR/TPU blends, the TPU phase is linear structure, not a crosslinked network, which restricts further properties improvement of the blends. The blends of NBR and PU ionomers were prepared by Dimitrievski *et al.* [14]. They studied the influence of the PU ionomers on the blend properties, blend miscibility and on the course and kinetics of vulcanization. In addition, blends of NBR and in-situ produced PU have been studied. Karger-Kocsis *et al.* [15, 16] prepared rubber blends of hydrogenated nitrile rubber (HNBR) and PU, in which the crosslinked PU was formed from solid PU precursors, viz. polyol and blocked polyisocyanate, during curing of the HNBR rubber. The mechanical and tribological properties of the blends were researched. PU/NBR blends were prepared by Desai *et al.* [17] through a combination of solution blending and mastication process. However, the use of large quantity of organic solvents and complicated procedures limited the application of the method. In this work, novel blends of NBR and in-situ produced PU-silica (PU-SiO<sub>2</sub>) hybrid networks are prepared. The NCO-terminated PU prepolymer is firstly prepared, the silica (SiO<sub>2</sub>) bearing numerous silanol groups is subsequently introduced, then the mixture of PU prepolymer and SiO<sub>2</sub> is dispersed in NBR matrix during the mixing process. The PU-SiO<sub>2</sub> hybrid networks are formed via the reaction of NCO groups of NCO-terminated PU prepolymer and OH groups of SiO<sub>2</sub> during the curing process of NBR. This process has not yet been reported in the literature. In this approach, the mixture of PU prepolymer and SiO<sub>2</sub> is in a gel-like form, which is strongly favored in solid phase raw rubber compounding. It could be pointed out that the SiO<sub>2</sub> in the mixture acts as not only as a reinforcing agent but

also a crosslinking agent of the PU prepolymer. Compared with the traditional crosslinking agent [18, 19], such as trimethylpropane (TMP) and 4,4'-methylenebis-(2-chloroaniline) (MOCA), the crosslinking agent used in this work is economic and environmentally friendly.

The aim of this work was to prepare blends of NBR and in-situ produced PU-SiO<sub>2</sub> hybrid networks. The structures of the PU-SiO<sub>2</sub> hybrid materials and NBR/(PU-SiO<sub>2</sub>) blends were characterized by Fourier-transform infrared (FTIR) spectroscopy, X-ray photoelectron spectroscopy (XPS), differential scanning calorimetry (DSC) and transmission electronic microscopy (TEM). The effects of PU-SiO<sub>2</sub> content on the vulcanization, compatibility, mechanical properties, abrasion resistance and flex-fatigue life of the blends were studied.

## 2. Experimental

### 2.1. Materials

Isophorone diisocyanate (IPDI) from Bayer (Germany) was purified by vacuum distillation. Poly(tetramethylene glycol) (PTMG,  $M_n = 1000$  g/mol) from Mitsui (Japan) and dibutyltin dilaurate (DBTDL, as catalyst) from Shanghai Reagent Co., (Shanghai, China) were dried at 80°C under vacuum (10mmHg) for 8 h before use. The NBR with acrylonitrile content 26% was kindly provided by Japan Synthetic Rubber Company. Tetramethyl thiuram disulfide (TMTD), 2,2'-dibenzothiazole disulfide (DM), zinc oxide (ZnO), stearic acid (SA) and sulfur (S) were obtained from Kemai Chemical Technical Co. Ltd. (Tianjin, China). Precipitated silica bearing surface silanol groups was purchased from Huiming Chemical Technical Co. Ltd. (Jiangxi, China). The surface area and primary particle size are 210 m<sup>2</sup>/g and 20 nm respectively.

### 2.2. Preparation of the mixture of PU prepolymer and SiO<sub>2</sub>

Weighed amounts of PTMG and DBTDL (0.05 wt% based on PUs) were charged into a round-bottomed flask, heated until 85°C, and thoroughly mixed with a predetermined amount of IPDI, which corresponded to a fixed NCO/OH ratio of 2:1. The reaction system was stirred vigorously with mechanical stirring, under a dry nitrogen atmosphere. The completion of the reaction was determined by the di-n-butylamine titration method when the theoretical

NCO percentage was reached. Then, the NCO-terminated PU prepolymer was obtained. After the PU prepolymer had cooled to room temperature, calculated amounts of SiO<sub>2</sub> (30 wt% based on PU prepolymer) was added, and the mixture was stirred at room temperature until it turn into gel-like form (for about 10 min), then the mixture of PU prepolymer and SiO<sub>2</sub> was obtained.

### 2.3. Preparation of blends of NBR and PU-SiO<sub>2</sub> hybrid networks

A two-roll mill (Kesheng Co. Ltd. Guangzhou, China) was used to prepare the NBR/(PU-SiO<sub>2</sub>) compounds. First, NBR and additives were mixed at room temperature for about 7 min, and then the calculated amounts of mixture of PU prepolymer and SiO<sub>2</sub> was added to the NBR compounds. The NBR compounds and mixture of PU prepolymer and SiO<sub>2</sub> were mixed uniformly at room temperature for about 5 min, then the NBR/(PU-SiO<sub>2</sub>) compounds were vulcanized in a standard mold at 120°C for optimal cure time (*t*<sub>90</sub>), which was determined by the U-CAN UR-2030 vulcameter (Taiwan, China). During the curing of the NBR/(PU-SiO<sub>2</sub>) compounds, the NCO groups of PU prepolymer reacted with OH groups of SiO<sub>2</sub> and the PU-SiO<sub>2</sub> hybrid networks were produced, and the linear molecular chains of NBR were crosslinked into three-dimensional networks under the action of the vulcanization system. Therefore, the blends based on NBR and PU-SiO<sub>2</sub> hybrid networks were generated. Figure 1 shows the schematic reaction of PU prepolymer and SiO<sub>2</sub>. In the present study, the recipe for NBR system was as follows (phr): NBR 100; ZnO 5; stearic acid 1.5, sulfur 1.5; TMTD 0.3; DM 1.5. The weight content of mixture of PU prepolymer and SiO<sub>2</sub> were 10, 20, 30, 40 and 50% in the NBR/(PU-SiO<sub>2</sub>) blends, which were regarded as NBR/(PU-

SiO<sub>2</sub>)-10, NBR/(PU-SiO<sub>2</sub>)-20, NBR/(PU-SiO<sub>2</sub>)-30, NBR/(PU-SiO<sub>2</sub>)-40 and NBR/(PU-SiO<sub>2</sub>)-50, respectively. For comparison purposes, neat NBR and PU-SiO<sub>2</sub> sheets were also produced at 120°C using appropriate respective optimum cure times. Specimens for the investigations were cut from the compression molded sheets of ca. 2 mm thickness.

### 2.4. Characterization

Fourier-transform infrared (FTIR) spectroscopy was conducted on a Nicolet Fourier-transform infrared spectrophotometer (Thermo Nicolet Corporation, Nicoletis10, America) at a resolution of 4 cm<sup>-1</sup>. PU prepolymer and SiO<sub>2</sub> were tested by transmission mode; PU-SiO<sub>2</sub> hybrid materials, NBR vulcanizate and NBR/(PU-SiO<sub>2</sub>)-50 blend were tested by attenuated total reflection mode.

X-ray photoelectron spectroscopy (XPS, Kratos Axis Ultra DLD, England) was performed to reveal the reaction between PU prepolymer and SiO<sub>2</sub>. SiO<sub>2</sub>, PU-SiO<sub>2</sub> hybrid materials and NBR/(PU-SiO<sub>2</sub>)-50 blend were tested with a monochromated Aluminum K $\alpha$  source (1486.6 eV). All XPS spectra were calibrated to its reference C1s component at 285.0 eV [20]. The PU-SiO<sub>2</sub> hybrid materials and NBR/(PU-SiO<sub>2</sub>)-50 blend were treated with butanone extraction and dried at 80°C for XPS test. The unreacted NCO-terminated PU prepolymer and SiO<sub>2</sub> should be removed by butanone extraction; otherwise they would interfere with the XPS results.

The isothermal curing process of the NBR, mixture of PU prepolymer and SiO<sub>2</sub> and NBR/(PU-SiO<sub>2</sub>)-50 compound were assessed by differential scanning calorimetry (DSC). The measurements were performed on a TA Q20 (New Castle, America) under N<sub>2</sub> atmosphere. The aluminum pans containing the samples were inserted onto the DSC sensor at 120°C and left at 120°C for 200 min.

Vulcanization parameters and curing curve for NBR, PU-SiO<sub>2</sub> and NBR/PU-SiO<sub>2</sub> compounds were tested in an oscillating disk rheometer (ODR) according to ASTM D2084 using a U-CAN UR2030 vulcameter. The temperature was set at 120°C, with a rotation amplitude of 1°. The compounds were tested under pressure in the die cavity located in the electrically heated plates. The cavity was formed by a fixed lower die and a movable upper die. The ODR maintained a contact with the specimen until the cure reaction was completed.

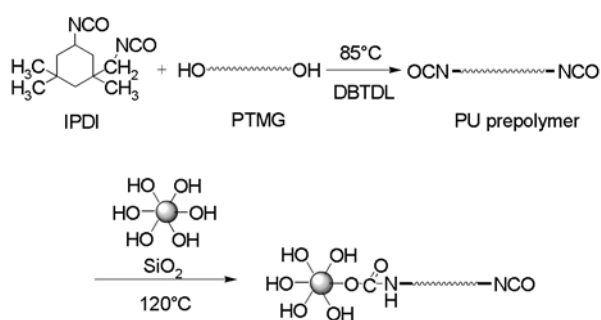


**Figure 1.** The schematic reaction of PU prepolymer and SiO<sub>2</sub>

The specimens were ultramicrotomed into thin pieces of about 120 nm thickness with a Leica EM UC6 (Wetzlar, Germany). Then the TEM observations were carried out using a Philips Tecnai 12 TEM (Amsterdam, Netherlands) at an accelerating voltage of 30 kV.

Dynamic Mechanical Analysis (DMA) spectra of the samples were obtained by using EPLEXOR @ 500 N/1500 N advanced dynamic mechanical spectrometer (GABO Company, Germany). The specimens were analyzed in tensile mode at a constant frequency of 10 Hz and a strain of 0.5%, and scanned from  $-100$  to  $100^{\circ}\text{C}$  at a heating rate of  $3^{\circ}\text{C}/\text{min}$ .

The tensile and tear tests of the vulcanizates were performed according to ASTM D412 and ASTM D624 specifications, respectively. U-CAN UT-2060 (Taipei, Taiwan) instrument was used with the crosshead speed of 500 mm/min. Shore A hardness was performed following ASTM D2240 using Sanling XY-1 sclerometer (Shanghai, China).

Akron abrasion loss was evaluated by a Gotech GT-7012-A testing machine (Taipei, China) according to BS 903/A9. The flex-fatigue life was measured using a De Mattia GT-7011-D flexing machine (Taipei, China) according to ASTM D430. For each sample, three pieces were tested and the average flex-fatigue-life value was reported. The flex-fatigue life was defined by the cycles at which a visible crack, that is, a grade-one crack, appeared.

### 3. Results and discussion

#### 3.1. Structure characterization of PU-SiO<sub>2</sub>

##### hybrid materials and NBR/(PU-SiO<sub>2</sub>) blend

##### 3.1.1. Fourier-transform infrared spectroscopy analysis

The FTIR spectra of the NCO-terminated PU prepolymer, SiO<sub>2</sub>, PU-SiO<sub>2</sub> hybrid materials, NBR vulcanizate and NBR/(PU-SiO<sub>2</sub>)-50 blend are shown in Figure 2. The spectrum of the NCO-terminated PU prepolymer shows absorption peak at  $2266\text{ cm}^{-1}$  corresponding to the NCO group. The characteristic peaks of urethane group are observed at  $3326$  and  $1714\text{ cm}^{-1}$ , corresponding to stretching vibrations of N-H and C=O groups, respectively. For the SiO<sub>2</sub>, the absorption peaks at  $1094$  and  $800\text{ cm}^{-1}$  are associated with Si-O-Si asymmetrical and symmetrical stretching vibrations respectively, and the absorption peaks at  $3446$  and  $960\text{ cm}^{-1}$  represent the

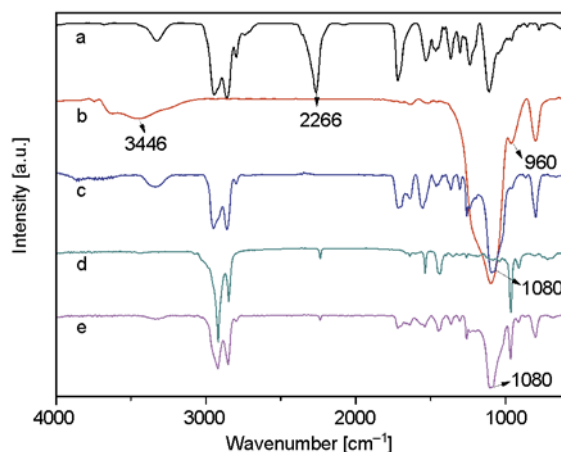


**Figure 2.** FTIR spectra of (a) NCO-terminated PU prepolymer, (b) SiO<sub>2</sub>, (c) PU-SiO<sub>2</sub> hybrid materials, (d) NBR vulcanizate and (e) NBR/(PU-SiO<sub>2</sub>)-50 blend

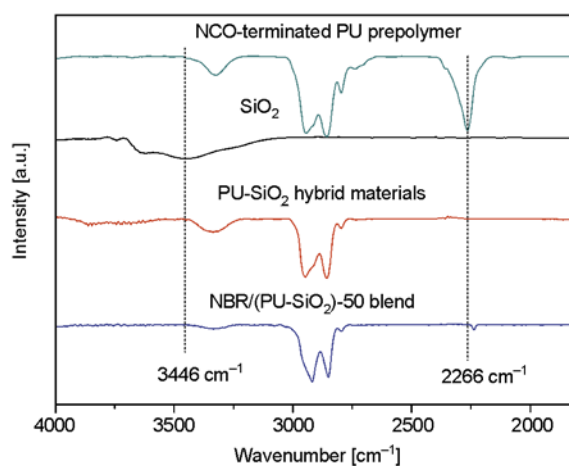


**Figure 3.** FTIR spectra of the NCO-terminated PU prepolymer, SiO<sub>2</sub>, PU-SiO<sub>2</sub> hybrid materials and NBR/(PU-SiO<sub>2</sub>)-50 blend in the region of  $1800$ – $4000\text{ cm}^{-1}$

Si-OH stretching vibrations. The spectrum of NBR vulcanizate shows absorption peak at  $2236\text{ cm}^{-1}$  corresponding to the  $-\text{CN}$  group. The  $-\text{CH}_2$  ( $2917$  and  $2847\text{ cm}^{-1}$ ), the *trans*  $>\text{C}=\text{CH}-$  ( $962\text{ cm}^{-1}$ ) and the vinylidene ( $>\text{C}=\text{CH}_2$ ;  $910\text{ cm}^{-1}$ ) are assigned to the NBR backbone. FTIR spectra of NCO-terminated PU prepolymer, SiO<sub>2</sub>, PU-SiO<sub>2</sub> hybrid materials and NBR/(PU-SiO<sub>2</sub>)-50 blend in the region of  $1800$ – $4000\text{ cm}^{-1}$  are reported in Figure 3. As shown in Figure 3, the absorption peaks of NCO at  $2266\text{ cm}^{-1}$  and Si-OH at  $3446\text{ cm}^{-1}$  in PU-SiO<sub>2</sub> hybrid materials and NBR/(PU-SiO<sub>2</sub>)-50 blend disappear. FTIR spectra of the SiO<sub>2</sub>, PU-SiO<sub>2</sub> hybrid materials and NBR/(PU-SiO<sub>2</sub>)-50 blend in the region of  $600$ – $1200\text{ cm}^{-1}$  are shown in Figure 4 and the integration results of Si-OH ( $960\text{ cm}^{-1}$ ) and Si-O-Si



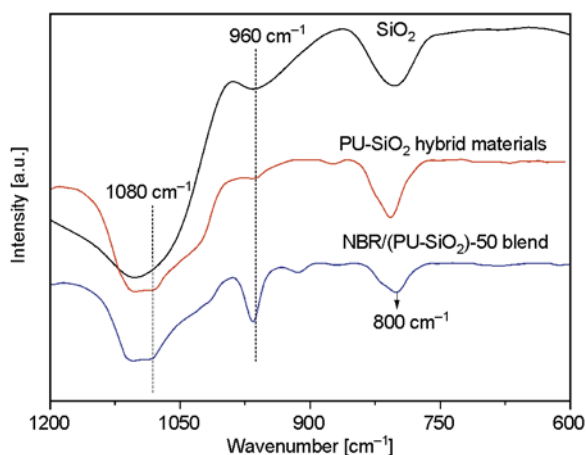


**Figure 4.** FTIR spectra of the SiO<sub>2</sub>, PU-SiO<sub>2</sub> hybrid materials and NBR/(PU-SiO<sub>2</sub>)-50 blend in the region of 600–1200 cm<sup>-1</sup>

**Table 1.** Integration results of Si–OH and Si–O–Si in SiO<sub>2</sub> and PU-SiO<sub>2</sub> hybrid materials

	Si–OH (960 cm <sup>-1</sup> )	Si–O–Si (800 cm <sup>-1</sup> )	I <sub>(Si–OH)</sub> /I <sub>(Si–O–Si)</sub>
SiO <sub>2</sub>	-3.24	-9.40	0.35
PU-SiO <sub>2</sub>	-0.48	-7.47	0.06

(800 cm<sup>-1</sup>) in SiO<sub>2</sub> and PU-SiO<sub>2</sub> hybrid materials are reported in Table 1. For PU-SiO<sub>2</sub> hybrid materials, the intensity ratio of I<sub>(960, Si–OH)</sub> to I<sub>(800, Si–O–Si)</sub> is obviously decreased from 35% for SiO<sub>2</sub> to 6% with a decrement about 29%. The adsorption peak of Si–OH bonds (960 cm<sup>-1</sup>) overlaps with the *trans* >C=CH– bonds (962 cm<sup>-1</sup>) in NBR/(PU-SiO<sub>2</sub>)-50 blend, while a weak absorption peak at 1080 cm<sup>-1</sup>

appears, corresponding to the Si–O–C bonds, and overlaps with C–O–C and Si–O–Si absorption peaks, which also appears in the PU-SiO<sub>2</sub> hybrid materials. All these changes indicate that the NCO groups of PU prepolymer have reacted with the OH groups of SiO<sub>2</sub> in the neat PU-SiO<sub>2</sub> system and NBR/(PU-SiO<sub>2</sub>)-50 system.

**3.1.2. X-ray photoelectron spectroscopy analysis**

The low-resolution XPS spectra of the SiO<sub>2</sub> and PU-SiO<sub>2</sub> hybrid materials are shown in Figure 5. As illustrated in Figure 5a, XPS survey spectrum of SiO<sub>2</sub> shows the carbon peak at 285.1 eV, oxygen peak at 532.1 eV and silicon peak at 103.3 eV [21]. While in the Figure 5b, besides these peaks in SiO<sub>2</sub>, a new peak at 400.0 eV appears, which is attributed to the nitrogen atom. Table 2 summarizes the characteristic XPS data. It can be seen that the ratios of C/Si and O/Si in PU-SiO<sub>2</sub> hybrid materials increase compared with those in SiO<sub>2</sub>. All the results can be explained by the fact that the PU prepolymer reacting with SiO<sub>2</sub> introduces abundance carbon atoms, oxygen atoms and nitrogen atoms onto the surface of SiO<sub>2</sub>. The results demonstrate that the NCO groups of PU prepolymer have reacted with the OH groups of SiO<sub>2</sub>. The high-resolution XPS spectra of Si 2p in SiO<sub>2</sub>, PU-SiO<sub>2</sub> hybrid materials and NBR/(PU-SiO<sub>2</sub>)-50 blend are reported in Figure 6. It can be seen that the binding energy (BE) of Si 2p in SiO<sub>2</sub> is located at 103.3 eV, while the BE shifts to a lower value in PU-SiO<sub>2</sub> hybrid materials and NBR/(PU-

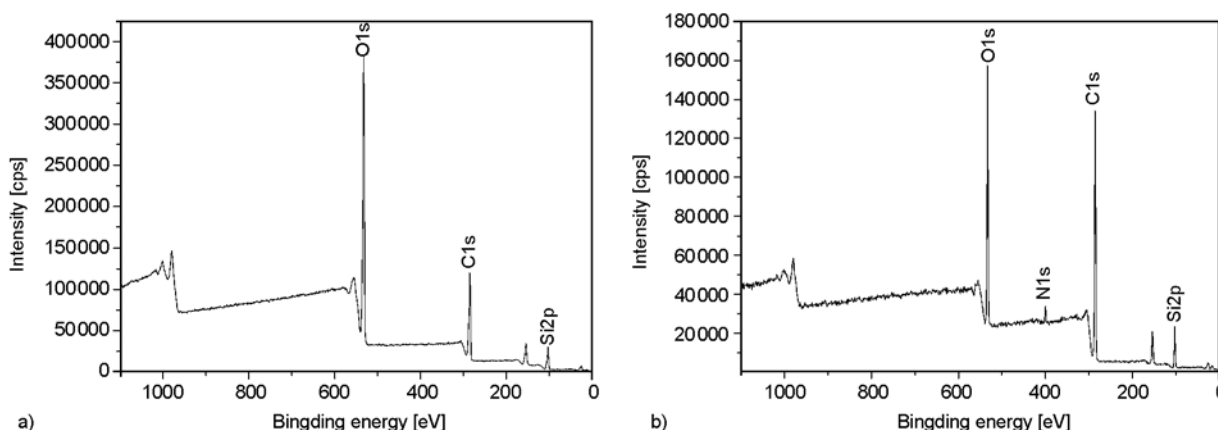


**Figure 5.** XPS spectra of (a) SiO<sub>2</sub> and (b) PU-SiO<sub>2</sub> hybrid materials

**Table 2.** XPS atomic content for the SiO<sub>2</sub> and PU-SiO<sub>2</sub> hybrid materials

Samples	Atom	C [%]	O [%]	Si [%]	N [%]	C/Si	O/Si
SiO <sub>2</sub>		47.44	38.29	14.27	0	3.32	2.68
PU-SiO <sub>2</sub> hybrid materials		64.99	25.70	7.01	2.30	9.27	3.67

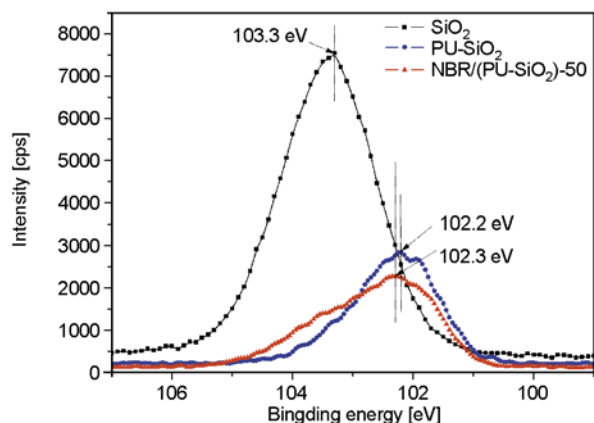


**Figure 6.** XPS spectra of Si 2p in SiO<sub>2</sub>, PU-SiO<sub>2</sub> hybrid materials and NBR/(PU-SiO<sub>2</sub>)-50 blend

SiO<sub>2</sub>)-50 blend. This means that the chemical environments of Si atoms in PU-SiO<sub>2</sub> hybrid materials and NBR/(PU-SiO<sub>2</sub>)-50 blend have changed, which is mostly caused by the reaction of NCO groups of PU prepolymer and OH groups of SiO<sub>2</sub>.

### 3.1.3. Differential scanning calorimetry analysis

Figure 7 shows plots of the reaction heat as a function of time for NBR, mixture of PU prepolymer and SiO<sub>2</sub> and NBR/(PU-SiO<sub>2</sub>)-50 compound during isothermal curing at 120°C. As can be seen, DSC diagram of neat NBR exhibits an exothermic peak, which achieves a maximum at 76.1 min. This exothermic peak is attributed to the crosslinking reaction of NBR molecular chains in the presence of curing agent. DSC trace of mixture of PU prepolymer and SiO<sub>2</sub> shows an exothermic peak with a maximum at 6.5 min. This exothermic peak is due to the reaction of NCO groups of PU prepolymer

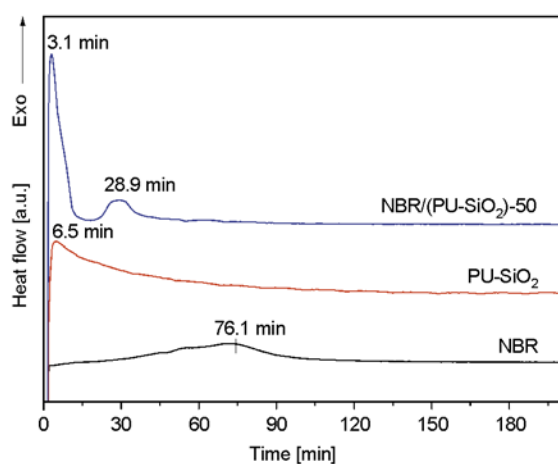


**Figure 7.** Curing time dependence of the heat flow during isothermal curing for NBR, mixture of PU prepolymer and SiO<sub>2</sub> and NBR/(PU-SiO<sub>2</sub>)-50 compound at curing temperatures of 120°C

and OH groups of SiO<sub>2</sub>. As for the NBR/(PU-SiO<sub>2</sub>)-50 compound, two exothermic peaks are observed: the exothermic peak with a maximum at 3.1 min and the one with a maximum at 28.9 min. The former is attributed to the reaction of NCO groups and OH groups and the latter to the crosslinking reaction of NBR. This indicates that in the NBR/(PU-SiO<sub>2</sub>)-50 compound, both the NBR system and PU-SiO<sub>2</sub> system are cured successfully. From Figure 7, it can be seen that both the reaction peak times of NBR system and PU-SiO<sub>2</sub> system in the NBR/(PU-SiO<sub>2</sub>)-50 compound are reduced compared with those in the initial components. As for the NBR system in the NBR/(PU-SiO<sub>2</sub>)-50 compound, the reaction peak time is 28.9 min, which shows a decrease of 62% compared with that of neat NBR. This is possibly caused by two aspects, on one hand, the organic zinc compounds (produced by ZnO with accelerating agent, i.e. DM and TMTD, during the vulcanization of NBR) and TMTD (containing tertiary amine groups) in the NBR system have catalytic action on the NCO/OH reaction of PU-SiO<sub>2</sub> system [19]; on the other hand, the urethane groups (containing secondary amine functionalities) which are produced by NCO groups with OH groups in the PU-SiO<sub>2</sub> system have an accelerating effect on the vulcanization of NBR. The secondary amine functionalities form complexes with accelerator compounds, which promote the crosslinking reaction of NBR. Similar accelerating effects have been reported by Karger-Kocsis and coworkers [10, 22, 23]. Because of the mutual cure accelerating effects of NBR system and PU-SiO<sub>2</sub> system, the reaction peak times of NBR system and PU-SiO<sub>2</sub> system in the NBR/(PU-SiO<sub>2</sub>)-50 compound are reduced.

### 3.1.4. Morphology

Figure 8a and 8b show the TEM images of NBR/(PU-SiO<sub>2</sub>)-30 blend and NBR/(PU-SiO<sub>2</sub>)-50 blend, respectively. In the images, the gray and white phases represent NBR and PU, respectively, and the black aggregates dispersed within the PU are silica. As shown in Figure 8a, when the PU-SiO<sub>2</sub> weight content is 30% in the blend, a sea-island morphology is formed. The PU appears as the disperse phase and NBR presents as the continuous phase. The average dimension of the PU phase is 0.3~1.0 μm. As the PU-SiO<sub>2</sub> weight content increases to 50%, the NBR and PU show co-continuous morphology. As can be

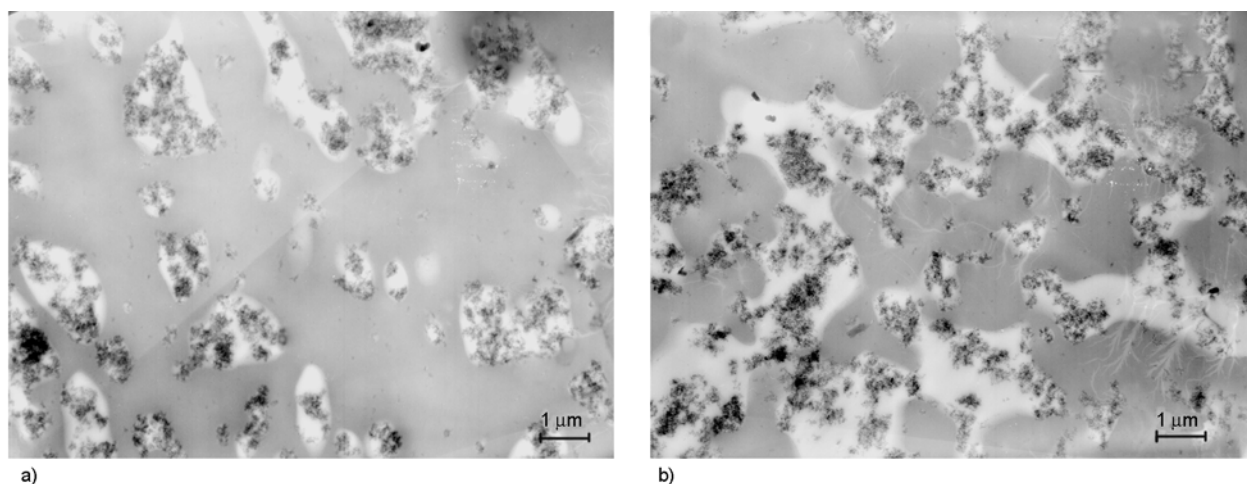


**Figure 8.** TEM images of (a) NBR/(PU-SiO<sub>2</sub>)-30 blend and (b) NBR/(PU-SiO<sub>2</sub>)-50 blend

seen in Figure 8b, the structures formed in this blend are on the micrometer scale instead of the nanoscale (or molecular scale), which are more like quasi-interpenetrating polymer network (quasi-IPN). Similar results have been reported by Šebenik *et al.* [16]. The unique microstructures formed in the systems are beneficial to the improvement of compatibility between the two phases and enhancement of mechanical properties of NBR [16, 24], which will be illustrated below.

One may notice that the phase dimension in the blends is slightly large. This is because that the high molecular weight of the NBR leads to increased viscosity, which restrains the completely interpenetration between NBR and PU networks and the formation of fine structures. According to the method, silica is co-cured with PU and forms an independent network penetrated in the NBR network and there would be no chemical linkages between NBR

and silica, therefore, the silica is restricted in the PU phase and no any discernible silica can be seen in the NBR phase. From the images it can be seen that some silica aggregates in the PU phase, which is mostly because that the high viscosity of PU prepolymer restrains the fine dispersion of silica in the process of blending.

### 3.1.5. The formation of NBR/(PU-SiO<sub>2</sub>) blends

From the above structure analysis, we propose the formation process of NBR/(PU-SiO<sub>2</sub>) blends, as shown in Figure 9. First, the NBR gum and mixture of PU prepolymer and SiO<sub>2</sub> are mixed by melt blending. Under the strong shear force of the blending process, the low molecular weight PU prepolymer and SiO<sub>2</sub> can be easily mixed uniformly with NBR gum. In the process, the PU prepolymer molecular chains will interpenetrate with NBR molecular chains. Then the blends are cured at 120°C. During

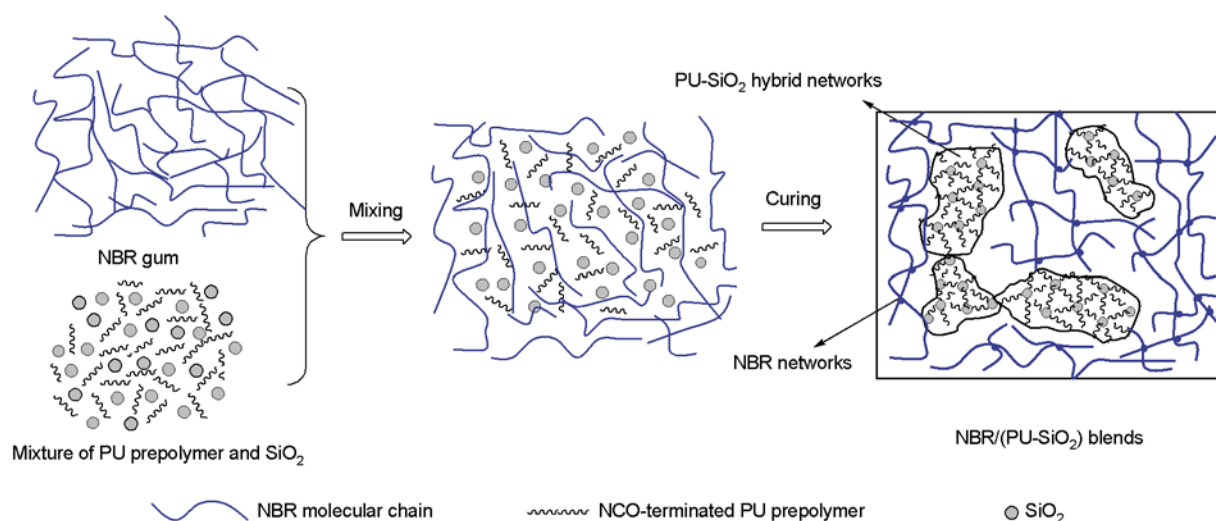


**Figure 9.** Schematic diagram for the formation process of NBR/(PU-SiO<sub>2</sub>) blends

the first 20 min of the curing process, the crosslinking reaction of PU-SiO<sub>2</sub> system plays a leading role. The NCO groups of PU prepolymer react with the OH groups of SiO<sub>2</sub> to form PU-SiO<sub>2</sub> hybrid networks. About 20 min later, the crosslinking reaction of NBR is dominant. The linear NBR molecular chains are crosslinked into three-dimensional networks under the action of vulcanization system. Therefore, the blends based on NBR and PU-SiO<sub>2</sub> hybrid materials are generated. The interpenetrating structures between NBR and PU-SiO<sub>2</sub> in the blends achieved in the blending process are preserved by the curing process, which is important for the excellent properties of the resulting NBR/(PU-SiO<sub>2</sub>) blends.

### 3.2. Properties of PU-SiO<sub>2</sub> hybrid materials and NBR/(PU-SiO<sub>2</sub>) blends

#### 3.2.1. Curing characteristics

The vulcanization curves of NBR, PU-SiO<sub>2</sub> and NBR/(PU-SiO<sub>2</sub>) compounds with different PU-SiO<sub>2</sub> loading are graphically represented in Figure 10. The vulcanization characteristics, expressed in terms of the vulcanization times,  $t_{s2}$  (scorch time) and  $t_{90}$

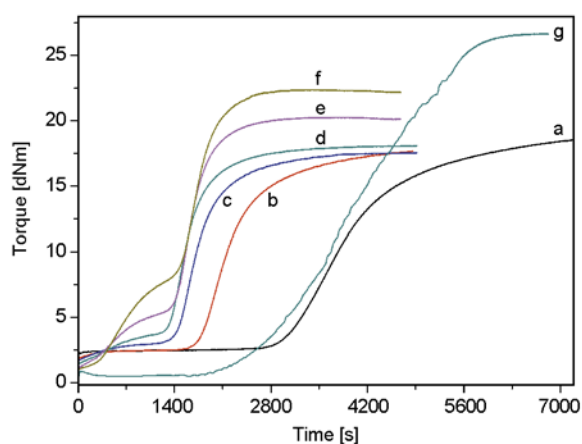


**Figure 10.** Vulcanization curves of (a) neat NBR, (b) NBR/(PU-SiO<sub>2</sub>)-10, (c) NBR/(PU-SiO<sub>2</sub>)-20, (d) NBR/(PU-SiO<sub>2</sub>)-30, (e) NBR/(PU-SiO<sub>2</sub>)-40, (f) NBR/(PU-SiO<sub>2</sub>)-50 and (g) PU-SiO<sub>2</sub>

(optimum cure time), as well as the maximum and minimum values of the torque,  $S_{max}$  and  $S_{min}$ , respectively, and delta torque  $\Delta S$  ( $\Delta S = S_{max} - S_{min}$ ), are deduced from the curves. These parameters, along with the cure rate index,  $CRI$ , expressed as  $CRI = \Delta S / (t_{90} - t_{s2})$ , which indicates the rate of cure of the compounds, are compiled in Table 3. A higher value of  $CRI$  means a higher rate of vulcanization.

It was found that, compared with those of NBR and PU-SiO<sub>2</sub>, the  $t_{s2}$  and  $t_{90}$  of NBR/(PU-SiO<sub>2</sub>) compounds with different PU-SiO<sub>2</sub> loading are sharply reduced with the addition of PU-SiO<sub>2</sub>. The NBR/(PU-SiO<sub>2</sub>) compound with 50 wt% PU-SiO<sub>2</sub> has  $t_{s2}$  and  $t_{90}$  of 8.22 and 34.93 min, respectively, which show decreases of 84.3 and 62.1% compared with those of neat NBR. The cure rate index values of the NBR/(PU-SiO<sub>2</sub>) compounds, show an increase with addition of PU-SiO<sub>2</sub> and exceed those of the NBR and PU-SiO<sub>2</sub>. The decreases in the scorch time and cure time accompanied with the increase in  $CRI$  of NBR/(PU-SiO<sub>2</sub>) compounds indicate that NBR system and PU-SiO<sub>2</sub> system tend to have an accelerating effect on the cure. These results are consistent with the conclusions derived from the reduced reaction peak times for the NBR system and PU-SiO<sub>2</sub> system in the NBR/(PU-SiO<sub>2</sub>)-50 compound. The minimum torque shows a decrease with increasing PU-SiO<sub>2</sub> content for all NBR/(PU-SiO<sub>2</sub>) compounds. This indicates that the processability of the compounds is improved after the incorporation of PU-SiO<sub>2</sub>. The increasing maximum torque indicates higher modulus as a result of the PU-SiO<sub>2</sub> addition. This is further supported by the increase in the difference between the maximum and minimum torque,  $\Delta S$ , upon PU-SiO<sub>2</sub> loading. As a consequence, PU-SiO<sub>2</sub> acts as a processing aid (improving the rheological properties of NBR) besides having an accelerating effect on the NBR vulcanization process. Note that, with increasing PU-SiO<sub>2</sub> content, especially when the PU-SiO<sub>2</sub> content achieves

**Table 3.** Vulcanization characteristics of NBR, PU-SiO<sub>2</sub> and NBR/(PU-SiO<sub>2</sub>) compounds with different PU-SiO<sub>2</sub> loading

PU-SiO <sub>2</sub> content [wt%]	$t_{s2}$ [min]	$t_{90}$ [min]	$S_{min}$ [dNm]	$S_{max}$ [dNm]	$\Delta S$ [dNm]	$CRI$ [dNm/min]
0 (NBR)	52.37	92.23	2.2	18.6	16.4	0.41
10	30.25	53.93	1.9	17.4	15.5	0.65
20	23.63	40.55	1.8	17.7	15.9	0.94
30	15.35	36.48	1.5	18.1	16.6	0.79
40	8.58	34.52	1.2	20.3	19.1	0.74
50	8.22	34.93	1.1	22.4	21.3	0.80
100(PU-SiO <sub>2</sub> )	49.42	110.93	0.3	25.7	25.4	0.41



50 wt% (Figure 10f), the vulcanization curves of NBR/(PU-SiO<sub>2</sub>) compounds appear to indicate two stages of cure acceleration. As can be seen from Figure 10f, one vulcanization accelerating stage begins at about 380 s, and the other begins at about 1490 s for the NBR/(PU-SiO<sub>2</sub>)-50 compound. The former stage is attributed to the crosslinking of PU-SiO<sub>2</sub> and the latter to the crosslinking of NBR, which is consistent with the two exothermic peaks of NBR/(PU-SiO<sub>2</sub>)-50 compound during the isothermal curing at 120°C. However, a possible mechanism for explaining this phenomenon is still under investigation.

### 3.2.2. Dynamic mechanical analysis

The DMA curves and data for the NBR, PU-SiO<sub>2</sub> and NBR/(PU-SiO<sub>2</sub>) blends with different PU-SiO<sub>2</sub> loading are reported in Figure 11 and Table 4, respectively. From Figure 11 and Table 4, it can be seen that the  $\tan\delta$  of the neat NBR exhibits one peak at  $-17.8^\circ\text{C}$ , which corresponds to the  $T_g$ , whereas PU has a  $T_g$  around  $-23.6^\circ\text{C}$  when we consider the position of the related  $\tan\delta$  peaks. As for all the NBR/(PU-SiO<sub>2</sub>) blends, the  $T_g$  around  $-20^\circ\text{C}$  is assigned to NBR, however the glass transition of PU-SiO<sub>2</sub> is not obvious. With the increasing of PU-SiO<sub>2</sub> content in the blends, the  $T_g$  of NBR in the NBR/(PU-SiO<sub>2</sub>) blends shifts to a lower temperature and locates between the  $T_g$ s of neat NBR and PU-SiO<sub>2</sub>. The result indicates that the compatibility

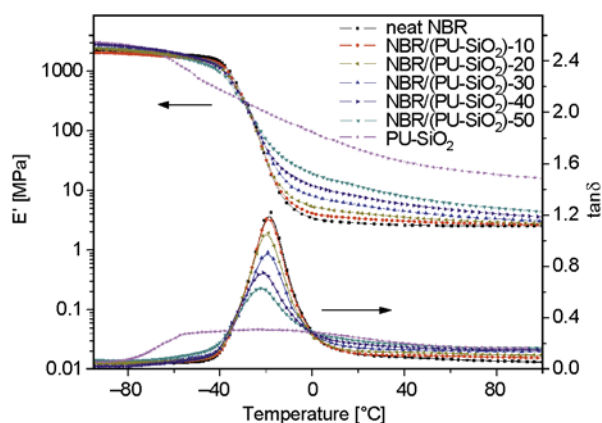


**Figure 11.** Storage modulus and  $\tan\delta$  versus the temperature for NBR, PU-SiO<sub>2</sub> and NBR/(PU-SiO<sub>2</sub>) blends with different PU-SiO<sub>2</sub> loading

**Table 4.** DMA data of NBR, PU-SiO<sub>2</sub> and NBR/(PU-SiO<sub>2</sub>) blends with different PU-SiO<sub>2</sub> loading

PU-SiO <sub>2</sub> content [wt%]	0 (NBR)	10	20	30	40	50	100 (PU-SiO <sub>2</sub> )
$T_g$ [ $^\circ\text{C}$ ]	-17.8	-18.5	-18.9	-19.2	-21.1	-22.3	-23.6
$\tan\delta_{[\text{max}]}$	1.22	1.17	1.06	0.91	0.75	0.63	0.3

between NBR phase and PU-SiO<sub>2</sub> phase is improved in the NBR/(PU-SiO<sub>2</sub>) blends [25, 26]. From the above TEM analysis, we can see that with more PU-SiO<sub>2</sub> incorporated in NBR, the interpenetration and entanglement structures between NBR and PU-SiO<sub>2</sub> increase. The entanglement of the two polymers networks leads to forced ‘compatibility’ [27], which can not be achieved by usual blending method. As a result, the compatibility of NBR and PU-SiO<sub>2</sub> is improved with increasing PU-SiO<sub>2</sub> content. The broadening of the  $\tan\delta$  peaks and decrease of  $T_g$  suggest that the damping properties and low temperature resistance of the blends are improved [28, 29]. With the addition of PU-SiO<sub>2</sub>, a noticeable reduction in  $\tan\delta$  peak height can be observed. The peak height of  $\tan\delta$  curve decreases from 1.223 for NBR to 0.632 for NBR/(PU-SiO<sub>2</sub>)-50 blend. The reduction in the  $\tan\delta$  peak height can be correlated with the morphology of this blend. As discussed in TEM analysis, in NBR/(PU-SiO<sub>2</sub>)-50 blend, the NBR and PU form a co-continuous morphology, which enhances interpenetration and entanglement of the two phases and restricts the motion of the polymers molecular chains. As a result, the  $\tan\delta$  peak height reduces greatly.

From the DMA curves of the storage modulus ( $E'$ ) versus temperature, it is evident that the more PU-SiO<sub>2</sub> is incorporated in the NBR, the higher the modulus in the rubbery plateau of the NBR is, which shows that the addition of PU-SiO<sub>2</sub> into NBR results in a remarkable increase of stiffness. This observation provides further evidence that the strong confinement of interpenetration network on the rubber chains. These results are in accordance with that the  $S_{\text{max}}$  increases with adding PU-SiO<sub>2</sub>.

### 3.2.3. Mechanical properties

The stress-strain behaviors of NBR, PU-SiO<sub>2</sub> and NBR/(PU-SiO<sub>2</sub>) blends with different PU-SiO<sub>2</sub> loading are presented in Figure 12 and Table 5. From the results it can be seen that NBR shows very poor mechanical properties. It is quite obvious because of the fact that NBR is a random copolymer having no regular structure. However, with the incorporation of the PU-SiO<sub>2</sub> in the NBR matrix, significant

**Table 5.** The data of stress-strain behaviors of NBR, PU-SiO<sub>2</sub> and NBR/(PU-SiO<sub>2</sub>) blends with different PU-SiO<sub>2</sub> loading

Properties	PU-SiO <sub>2</sub> content [wt%]						
	0 (NBR)	10	20	30	40	50	100 (PU-SiO <sub>2</sub> )
100% Modulus [MPa]	1.3±0.1	1.5±0.1	1.7±0.1	2.1±0.1	2.8±0.1	3.5±0.1	5.6±0.1
300% Modulus [MPa]	–	3.0±0.1	3.6±0.2	4.6±0.1	6.1±0.1	8.1±0.1	13.1±0.2
Tensile strength [MPa]	1.9±0.4	8.0±0.5	14.0±0.5	20.6±0.6	23.5±0.5	25.2±0.5	26.0±0.5
Elongation at break [%]	281±10	481±13	520±12	535±15	518±12	530±12	406±13
Tear strength [kN/m]	8.2±1.0	20.8±1.2	25.8±1.3	31.7±0.9	40.2±1.1	52.3±0.9	58.4±1.0
Shore A hardness	52	53	55	63	65	72	81

increases in the modulus, tensile strength, elongation at break, hardness and tear strength are achieved (Table 5). When the PU-SiO<sub>2</sub> content increases from 0 to 50 wt%, the tensile strength and tear strength increase from 1.9 MPa and 8.2 kN/m to 25.2 MPa and 52.3 kN/m, which are 1226 and 538% higher than those for NBR respectively. This demonstrates that the PU-SiO<sub>2</sub> hybrid network could significantly enhance the NBR vulcanizate. This is consistent with the above morphology results. The formation of quasi-IPN structures in the blends with

high PU-SiO<sub>2</sub> content are beneficial to the improvement of the mechanical properties [30, 31], as the mechanical properties of the systems reach maximum for the NBR/(PU-SiO<sub>2</sub>) blends. The tensile strength and tear strength as a function of weight fraction of PU-SiO<sub>2</sub> in blends are shown in Figure 13. As can be seen, the tensile strength and tear strength of the NBR/(PU-SiO<sub>2</sub>) blends show a positive deviation from linearity in all cases, which exhibits synergistic behavior. The improved mechanical properties and synergistic behavior are mainly caused by the good compatibility of NBR and PU-SiO<sub>2</sub> [32]. The elongation at break of the NBR/(PU-SiO<sub>2</sub>) blends increases with the addition of PU-SiO<sub>2</sub> and exceeds those of the neat NBR and PU-SiO<sub>2</sub>, which exhibits that the incorporation of PU-SiO<sub>2</sub> hybrid network does not deteriorate the elasticity of the NBR.

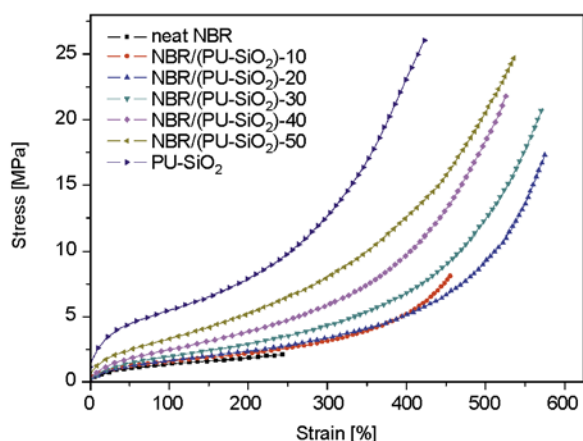


**Figure 12.** The stress–strain behaviors of NBR, PU-SiO<sub>2</sub> and NBR/(PU-SiO<sub>2</sub>) blends with different PU-SiO<sub>2</sub> loading

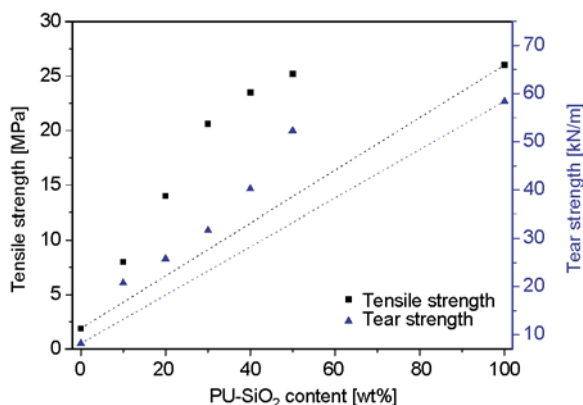


**Figure 13.** Dependence of tensile strength and tear strength of NBR/(PU-SiO<sub>2</sub>) blends on the PU-SiO<sub>2</sub> content

### 3.2.4. Abrasion resistance and flex-fatigue life

The Akron abrasion loss and flex-fatigue life of NBR/(PU-SiO<sub>2</sub>) blends with different amounts of PU-SiO<sub>2</sub> are shown in Figure 14. The results reveal that the Akron abrasion loss of NBR/(PU-SiO<sub>2</sub>) blend is significantly decreased with increasing PU-SiO<sub>2</sub> content. When the PU-SiO<sub>2</sub> increases from 0 to

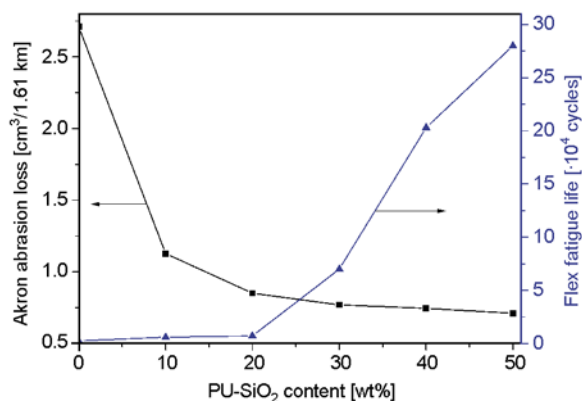


**Figure 14.** Effect of the amount of PU-SiO<sub>2</sub> on the Akron abrasion loss and flex-fatigue life of NBR/(PU-SiO<sub>2</sub>) blends

50 wt%, the value of Akron abrasion loss decreases from 2.71 to 0.71 cm<sup>3</sup>/1.61 km, which is 73.8% lower than that for NBR. It can be seen that the PU-SiO<sub>2</sub> hybrid network can enhance the abrasion resistance of NBR greatly. It is well known that the abrasion resistance of PU is excellent [33]. The PU crosslinked by SiO<sub>2</sub> preserves the outstanding abrasion resistance, the Akron abrasion loss of which is 0.45 cm<sup>3</sup>/1.61 km. The abrasion resistance improvement of NBR after incorporation of PU-SiO<sub>2</sub> is mostly because of the excellent abrasion resistance of the PU-SiO<sub>2</sub>.

From the curves of flex-fatigue life versus PU-SiO<sub>2</sub> content, it can be seen that when the PU-SiO<sub>2</sub> content is less than 20 wt%, the flex-fatigue life improvement is not great, while as the PU-SiO<sub>2</sub> content exceeds 20 wt%, the flex-fatigue life is dramatically improved. Especially when the PU-SiO<sub>2</sub> amount increased from 20 to 30 wt%, increasing the PU-SiO<sub>2</sub> amount by only 10 wt% causes that the flex-fatigue life to increase nearly 10 times, from 7.2 thousand cycles to 70 thousand cycles. It is important to point out that the flex-fatigue life of neat NBR and PU-SiO<sub>2</sub> hybrid materials are 2.5 and 3.5 thousand cycles, respectively. However, the flex-fatigue life of NBR/(PU-SiO<sub>2</sub>)-50 blend is 280 thousand cycles, which is more than 100 times that of neat NBR. It can be seen the flex-fatigue life of the individual components are relatively poor, while the flex-fatigue life of the resulting NBR/(PU-SiO<sub>2</sub>) blends are improved significantly. The great improvement of flex-fatigue life of the NBR/(PU-SiO<sub>2</sub>) blends may be explained in terms of the microstructures suggested in TEM analysis. With the increasing of PU-SiO<sub>2</sub> content, the interpenetration and entanglement structures between NBR and PU-SiO<sub>2</sub> increase, these structures are beneficial to the improvement of flex-fatigue life.

#### 4. Conclusions

Novel blends of NBR and in-situ produced PU-SiO<sub>2</sub> hybrid networks were prepared successfully by melt blending. The PU-SiO<sub>2</sub> hybrid networks were formed via the reaction of NCO groups of PU prepolymer and OH groups of SiO<sub>2</sub> in the absence of an external crosslinking agent (i.e. alcohols and amines) during the curing process of NBR. The incorporation of PU-SiO<sub>2</sub> into NBR matrix led to

higher curing rate, this is due to the mutual cure accelerating effects of NBR system and PU-SiO<sub>2</sub> system. Transmission electronic microscopy (TEM) studies indicated that the interpenetration and entanglement structures between NBR and PU-SiO<sub>2</sub> increased with increasing PU-SiO<sub>2</sub> content and the quasi-interpenetrating polymer networks (quasi-IPN) structures were formed when the weight content of PU-SiO<sub>2</sub> was 50% in the NBR/(PU-SiO<sub>2</sub>) systems. The DMA results showed that the compatibility between NBR and PU-SiO<sub>2</sub> was improved with PU-SiO<sub>2</sub> loading. The PU-SiO<sub>2</sub> hybrid network showed promising reinforceability towards the NBR compounds. The modulus, tensile strength, tear strength and hardness were found to be increased consistently with the content of PU-SiO<sub>2</sub>. When the PU-SiO<sub>2</sub> content was 50 wt%, 1226 and 538% increases of tensile strength and tear strength of the neat NBR vulcanizate were achieved. The abrasion resistance and flex-fatigue life of NBR were improved significantly by the incorporation of PU-SiO<sub>2</sub>. Further work will focus on the studies of reaction kinetics and phase separation kinetics of NBR and PU-SiO<sub>2</sub> components in the NBR/(PU-SiO<sub>2</sub>) blends, and the factors affecting the reaction and phase separation kinetics. The purposes of these studies are to get finer structures in the NBR/(PU-SiO<sub>2</sub>) blends, which is important for the performance improvement of the blends.

#### References

- [1] Paul D. R., Bucknall C. B.: *Polymer blends: Formulation and performance*. Wiley, New York (2000).
- [2] Utracki L. A.: *Polymer alloys and blends: Thermodynamics and rheology*. Hanser, Munich (1989).
- [3] Yasin K. A., Ansarifar A., Hameed S., Wang L.: A new method for crosslinking and reinforcing acrylonitrile-butadiene rubber using a silanized silica nanofiller. *Polymer Advanced Technology*, **22**, 215–224 (2011). DOI: [10.1002/pat.1518](https://doi.org/10.1002/pat.1518)
- [4] Wang X-P., Huang A-M., Jia D-M., Li Y-M.: From exfoliation to intercalation – Changes in morphology of HNBR/organoclay nanocomposites. *European Polymer Journal*, **44**, 2784–2789 (2008). DOI: [10.1016/j.eurpolymj.2008.06.035](https://doi.org/10.1016/j.eurpolymj.2008.06.035)
- [5] Liu L., Jia D., Luo Y., Guo B.: Preparation, structure and properties of nitrile-butadiene rubber-organoclay nanocomposites by reactive mixing intercalation method. *Journal of Applied Polymer Science*, **100**, 1905–1913 (2006). DOI: [10.1002/app.22614](https://doi.org/10.1002/app.22614)

- [6] El-Nashar D. E., Ward A. A., Abd-El-Messieh S. L.: Physico-mechanical and dielectric properties of nitrile rubber filled with silica and mica. *Kautschuk Gummi Kunststoffe*, **62**, 434–440 (2009).
- [7] Samaržija-Jovanović S., Jovanović V., Marković G.: Thermal and vulcanization kinetic behaviour of acrylonitrile butadiene rubber reinforced by carbon black. *Journal of Thermal Analysis and Calorimetry*, **94**, 797–803 (2008).  
DOI: [10.1007/s10973-007-8488-7](https://doi.org/10.1007/s10973-007-8488-7)
- [8] Bakare I. O., Pavithran C., Okieimen F. E., Pillai C. K. S.: Synthesis and characterization of rubber-seed-oil-based polyurethanes. *Journal of Applied Polymer Science*, **109**, 3292–3301 (2008).  
DOI: [10.1002/app.28391](https://doi.org/10.1002/app.28391)
- [9] Deng J., Cao J., Li J., Tan H., Zhang Q., Fu Q.: Mechanical and surface properties of polyurethane/fluorinated multi-walled carbon nanotubes composites. *Journal of Applied Polymer Science*, **108**, 2023–2028 (2008).  
DOI: [10.1002/app.27625](https://doi.org/10.1002/app.27625)
- [10] Kumar C. R., Karger-Kocsis J.: Curing and mechanical behavior of carboxylated NBR containing hygrothermally decomposed polyurethane. *European Polymer Journal*, **38**, 2231–2237 (2002).  
DOI: [10.1016/S0014-3057\(02\)00122-2](https://doi.org/10.1016/S0014-3057(02)00122-2)
- [11] Im H. G., Ka K. R., Kim C. K.: Characteristics of polyurethane elastomer blends with poly(acrylonitrile-co-butadiene) rubber as an encapsulant for underwater sonar devices. *Industrial and Engineering Chemistry Research*, **49**, 7336–7342 (2010).  
DOI: [10.1021/ie100975n](https://doi.org/10.1021/ie100975n)
- [12] Kotal M., Srivastava S. K., Bhowmick A. K.: Thermoplastic polyurethane and nitrile butadiene rubber blends with layered double hydroxide nanocomposites by solution blending. *Polymer International*, **59**, 2–10 (2010).  
DOI: [10.1002/pi.2686](https://doi.org/10.1002/pi.2686)
- [13] Tang T., Zhao H. Y., Chen H., Huang B. T.: The relationship of tensile strength with components for the binary multiphase blends (in Chinese). *Polymer Materials Science and Engineering*, **11**, 1–5 (1995).
- [14] Dimitrievski I., Susteric Z., Marinovic T.: Effect of PU-NBR interactions on blends' dynamic properties. in 'Proceedings 5<sup>th</sup> European Rheology Conference Portoroz, Slovenia' vol V, 73–74 (1998).
- [15] Karger-Kocsis J., Felhős D., Xu D.: Mechanical and tribological properties of rubber blends composed of HNBR and in situ produced polyurethane. *Wear*, **268**, 464–472 (2010).  
DOI: [10.1016/j.wear.2009.08.037](https://doi.org/10.1016/j.wear.2009.08.037)
- [16] Šebenik U., Karger-Kocsis J., Krajnc M., Thomann R.: Dynamic mechanical properties and structure of *in situ* cured polyurethane/hydrogenated nitrile rubber compounds: Effect of carbon black type. *Journal of Applied Polymer Science*, **125**, E41–E48 (2012).  
DOI: [10.1002/app.35626](https://doi.org/10.1002/app.35626)
- [17] Desai S., Thakore I. M., Brennan A., Devi S.: Polyurethane-nitrile rubber blends. *Journal of Macromolecular Science: Pure and Applied Chemistry*, **38**, 711–729 (2001).  
DOI: [10.1081/MA-100103875](https://doi.org/10.1081/MA-100103875)
- [18] Madbouly S. A., Otaigbe J. U.: Recent advances in synthesis, characterization and rheological properties of polyurethanes and POSS/polyurethane nanocomposites dispersions and films. *Progress in Polymer Science*, **34**, 1283–1332 (2009).  
DOI: [10.1016/j.progpolymsci.2009.08.002](https://doi.org/10.1016/j.progpolymsci.2009.08.002)
- [19] Wirpsza Z.: *Polyurethanes: Chemistry, technology and applications*. Ellis Horwood Limited, New York (1993).
- [20] Watts J. F., Wolstenholme J.: *An introduction to surface analysis by XPS and AES*. Wiley, Chichester (2003).  
DOI: [10.1002/0470867930](https://doi.org/10.1002/0470867930)
- [21] Moulder J. F., Stickle W. F., Sobol P. E., Bomben K. D.: *Handbook of X ray photoelectron spectroscopy*. Perkin-Elmer Corporation, Minnesota (1992).
- [22] Mousa A., Karger-Kocsis J.: Application of hygrothermally decomposed polyurethane in rubber recipes Part 2 – Influence of hygrothermally decomposed polyester-urethane on cure characteristics and viscoelastic behaviour of styrene/butadiene rubber. *Plastics, Rubber and Composites*, **30**, 309–313 (2001).  
DOI: [10.1179/146580101322913211](https://doi.org/10.1179/146580101322913211)
- [23] Karger-Kocsis J., Gremmels J., Mousa A., Ishiaku U. S., Ishak Z. A. M.: Application of hygrothermally decomposed polyurethane in rubber recipes Part 1: Natural rubber (NR) and nitrile rubber (NBR) stocks. *Kautschuk Gummi Kunststoffe*, **53**, 528–533 (2000).
- [24] Xu D., Karger-Kocsis J.: Unlubricated rolling and sliding wear against steel of carbon-black-reinforced and *in situ* cured polyurethane containing ethylene/propylene/diene rubber compounds. *Journal of Applied Polymer Science*, **115**, 1651–1662 (2010).  
DOI: [10.1002/app.31156](https://doi.org/10.1002/app.31156)
- [25] Chen S., Wang Q., Pei X., Wang T.: Dynamic mechanical properties of castor oil-based polyurethane/epoxy graft interpenetrating polymer network composites. *Journal of Applied Polymer Science*, **118**, 1144–1151 (2010).  
DOI: [10.1002/app.32518](https://doi.org/10.1002/app.32518)
- [26] Lu Y., Zhang L., Zhang X., Zhou Y.: Effects of secondary structure on miscibility and properties of semi-IPN from polyurethane and benzyl konjac glucomannan. *Polymer*, **44**, 6689–6696 (2003).  
DOI: [10.1016/S0032-3861\(03\)00594-9](https://doi.org/10.1016/S0032-3861(03)00594-9)



- [27] Dean K., Cook W. D.: Effect of curing sequence on the photopolymerization and thermal curing kinetics of dimethacrylate/epoxy interpenetrating polymer networks. *Macromolecules*, **35**, 7942–7954 (2002).  
DOI: [10.1021/ma020628p](https://doi.org/10.1021/ma020628p)
- [28] Trakulsujaritchook T., Hourston D. J.: Damping characteristics and mechanical properties of silica filled PUR/PEMA simultaneous interpenetrating polymer networks. *European Polymer Journal*, **42**, 2968–2976 (2006).  
DOI: [10.1016/j.eurpolymj.2006.07.028](https://doi.org/10.1016/j.eurpolymj.2006.07.028)
- [29] Qin C-L., Cai W-M., Cai J., Tang D-Y., Zhang J-S., Qin M.: Damping properties and morphology of polyurethane/vinyl ester resin interpenetrating polymer network. *Materials Chemistry and Physics*, **85**, 402–409 (2004).  
DOI: [10.1016/j.matchemphys.2004.01.019](https://doi.org/10.1016/j.matchemphys.2004.01.019)
- [30] John J., Suriyakala R., Thomas S., Mendez J. M., Pius A., Thomas S.: Morphology, mechanical and thermal properties of nano-structured full IPNs based on polyisoprene and PMMA. *Journal of Materials Science*, **45**, 2892–2901 (2010).  
DOI: [10.1007/s10853-010-4280-3](https://doi.org/10.1007/s10853-010-4280-3)
- [31] Hsieh K. H., Han J. L., Yu C. T., Fu S. C.: Graft interpenetrating polymer networks of urethane-modified bismaleimide and epoxy (I): Mechanical behavior and morphology. *Polymer*, **42**, 2491–2500 (2001).  
DOI: [10.1016/S0032-3861\(00\)00641-8](https://doi.org/10.1016/S0032-3861(00)00641-8)
- [32] Karabanova L. V., Boiteux G., Seytre G., Stevenson I., Gain O., Hakme C., Lutsyk E. D., Svyatyna A.: Semi-interpenetrating polymer networks based on polyurethane and poly(2-hydroxyethyl methacrylate): Dielectric study of relaxation behavior. *Journal of Non-Crystalline Solids*, **355**, 1453–1460 (2009).  
DOI: [10.1016/j.jnoncrysol.2009.05.002](https://doi.org/10.1016/j.jnoncrysol.2009.05.002)
- [33] Kannan M., Bhagawan S. S., Jose T., Thomas S., Joseph K.: Preparation and characterization of nanoclay-filled polyurethane/polypropylene blends. *Polymer Engineering and Science*, **50**, 1878–1886 (2010).  
DOI: [10.1002/pen.21703](https://doi.org/10.1002/pen.21703)

# Raman spectroscopic characterization of multiwall carbon nanotubes and of composites

L. Bokobza\*, J. Zhang

Université Pierre et Marie Curie- Ecole Supérieure de Physique et Chimie Industrielles – Centre National de la Recherche Scientifique, UMR 7615, 10 rue Vauquelin, 75231 Paris Cedex 05, France

Received 9 December 2011; accepted in revised form 9 February 2012

**Abstract.** In this work Raman spectroscopy was used for extensive characterization of multiwall carbon nanotube (MWNTs) and of MWCNTs/rubber composites. We have measured the Raman spectra of bundled and dispersed multiwall carbon nanotubes. All the Raman bands of the carbon nanotubes are seen to shift to higher wavenumbers upon debundling on account of less intertube interactions. Effects of laser irradiation were also investigated. Strong effects are observed by changing the wavelength of the laser excitation. On the other hand, at a given excitation wavelength, changes on the Raman bands are observed by changing the laser power density due to sample heating during the measurement procedure.

**Keywords:** polymer nanocomposites, carbon nanotubes, Raman spectroscopy

## 1. Introduction

Over the past decade, a huge scientific interest, both theoretically and experimentally, has been focused on carbon nanotubes (CNTs) due to their unprecedented properties arising from their unique one-dimensional character. The combination of superb mechanical, electrical and thermal properties makes CNTs ideal reinforcing fillers for advanced composite materials. But one of the major problem is the fact that nanotubes aggregate in bundles as a result of substantial van der Waals attractions and homogeneous dispersion of CNTs in the host matrix is probably the most fundamental issue for efficient load transfer and good reinforcement [1–6].

Raman spectroscopy has been shown to be a powerful and nondestructive technique for the characterization of carbon-based materials including carbon black (CB) and carbon nanotubes (CNTs) and it has become an invaluable tool for understanding many fundamental aspects of all  $sp^2$  carbons [7, 8]. The diameter of nanotubes [9], the presence of disorder

in  $sp^2$ -hybridized carbon systems [10] as well as the effect of nanotube-nanotube interactions [11] on the vibrational modes have been assessed using Raman spectroscopy. Specific features such as the strong frequency dependence on the excitation laser energy of some Raman bands [12–17] or laser radiation-induced effects [18–21] have been the subject of extensive studies.

Raman spectroscopy of CNT-based composite materials has been used to evaluate the state of dispersion and the polymer-filler interactions reflected, by shifts or width changes of the peaks. On the other hand, the sensitivity of some bands of CNTs to an application of mechanical deformation to the composite has also been used to quantify the load transferred from the matrix to the nanotubes and thus the interfacial adhesion [22–25].

This paper reports some investigations carried out by Raman spectroscopy on multiwall carbon nanotubes (MWCNTs) and on MWCNTs/rubber composites. For both materials, the dependence of Raman

\*Corresponding author, e-mail: [Liliane.Bokobza@espci.fr](mailto:Liliane.Bokobza@espci.fr)  
© BME-PT

spectra on various parameters such as the excitation laser energy or heating effects induced by the laser power, will be discussed.

## 2. Experimental part

### 2.1. Materials

Multiwall carbon nanotubes (MWNTs) were purchased from Nanocyl S.A. (Belgium). In this study, we have used the Nanocyl 7000 series (purity: 90%) produced via the catalytic carbon vapor deposition process without any further purification. Their average diameter and length are around 10 nm and 1.5  $\mu\text{m}$  respectively and their surface area between 250 and 300  $\text{m}^2\cdot\text{g}^{-1}$ .

The matrix that hosts the nanotubes is an elastomer based on a styrene-butadiene rubber (SBR) (Buna VSL 5025-0 from Bayer, Germany) supplied by Formix (Orléans, France). It contains 25 wt% of styrene unit and a butadiene phase with cis (10%), trans (17%) and vinyl (73%) configurations. It was compounded with sulfur (1.1 phr), stearic acid (1.1 phr), cyclohexylbenzothiazole sulfenamide (1.3 phr), diphenylguanidine (1.45 phr) and zinc oxide (1.82 phr), 'phr' means parts per hundred parts of rubber by weight.

### 2.2. Composite processing

An appropriate amount of MWNTs was dispersed into cyclohexane (in an approximate ratio 1:10 by weight) by sonicating the suspension for 30 min using a Vibra-Cell VCX 500 operating at 40% amplitude with on and off cycles respectively equal to 4 and 2 seconds.

The gum containing the SBR rubber and all the ingredients of formulation was mixed separately in cyclohexane under magnetic stirring until complete dissolution then mixed with the MWNTs dispersion. The mixture may be submitted to a further sonication for 30 min if global examination by optical microscopy still reveals nanotube agglomeration on a micrometer scale. The sonication process is followed by agitation under magnetic stirring until evaporation of the solvent. Total removal of any remaining solvent is achieved under vacuum overnight at 50°C before the cross-linking process and film formation. The unfilled and filled samples were then cured into plaques at 170°C during 10 min under a pressure of 150 bar in a standard hot press. The resulting films were around 300  $\mu\text{m}$  thick.

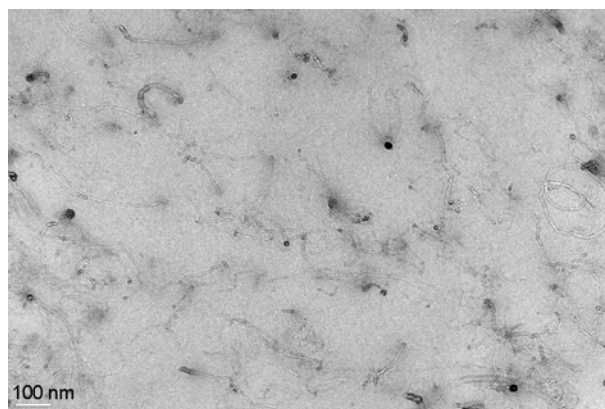


**Figure 1.** TEM image of the SBR-3 phr MWNTs composite

These processing conditions ensure a good dispersion of the carbon nanotubes in the elastomeric matrix as revealed by the image obtained by transmission electron microscopy (TEM) of a SBR composite filled with 3 phr of MWNTs (Figure 1). The image was obtained from a JEOL JEM-2010 Electron Microscope (Japan), operating at 200 kV. Ultrathin sections (50–60 nm) were cut at  $-90^\circ\text{C}$  by using an Ultracut S ultramicrotome from Leica fitted with a diamond knife from Diatome.

### 2.3. Raman spectra

The Raman spectra were recorded in the backscattering geometry on a Labram HR (Jobin-Yvon, Horiba Group, France) microspectrometer in conjunction with a confocal microscope. Most of the experiments were carried out with an excitation wavelength of 514.5 nm from a tunable Argon laser focused on the sample by means of a 100 $\times$  objective of 0.9 numerical aperture. The spot is around 3  $\mu\text{m}$  diameter while the beam intensity is 1 mW. But as shown below other excitation wavelengths or laser powers were used in order to show the sensitivity of the Raman spectra to these parameters.

## 3. Results and discussion

### 3.1. Effect of tube-tube interactions on the Raman modes of MWCNTs

The two main typical graphite bands are present in the Raman spectrum of MWCNTs bundles: the band at 1580  $\text{cm}^{-1}$  (G band) assigned to the in-plane vibration of the C–C bond (G band) with a shoulder around 1604  $\text{cm}^{-1}$ , typical of defective graphite-like materials and the band at 1342  $\text{cm}^{-1}$  (D band) activated by the presence of disorder in carbon systems. The Raman spectrum also exhibits a band at

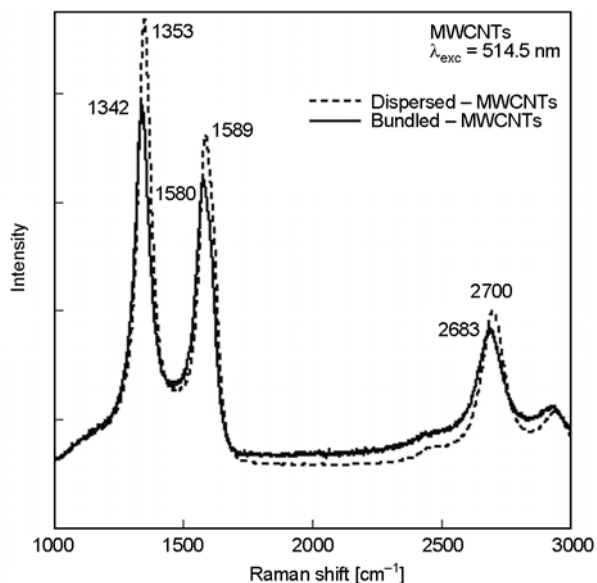


**Figure 2.** Raman spectra of bundled and dispersed multi-wall carbon nanotubes (MWCNTs)

2683  $\text{cm}^{-1}$  called the  $G'$  band and attributed to the overtone of the D band. These bands have been obtained on the as-received powder of bundled MWCNTs. In Figure 2, the Raman spectrum of raw nanotubes is compared to that deposited from solution to evaluate the separation of nanotube bundles. The raw nanotubes were dispersed in cyclohexane by ultrasonication during 30 min and the Raman spectrum is taken after drop casting the solution on a glass slide and evaporating the organic solvent. With regard to the raw nanotubes, all the Raman bands of the dispersed nanotubes are shifted to

higher wavenumbers indicating less intertube interactions.

A debundling also occurs by penetration of polymer chains into nanotube aggregates during composite processing. In Figure 3 are displayed the Raman spectrum of an unfilled elastomeric matrix, it is a styrene-butadiene rubber (SBR) and that of a composite filled with 5 phr of MWCNTs (phr = parts per hundred parts of rubber by weight). With regard to the spectrum of dispersed nanotubes represented in Figure 2, a further upshifting is observed when the tubes are embedded in the host matrix as a consequence of a disentanglement and subsequent dispersion in the polymeric medium. As seen in Figure 3, the Raman spectrum of the composite is almost dominated by the bands of the nanotubes but some bands of the SBR are still present especially those located at 1005, 2856, 2917, 2995 and 3065  $\text{cm}^{-1}$ . These polymer bands are also shifted to higher frequencies with regard to those of the unfilled polymer as consequence of physical constraints introduced to the polymer chains by the presence of the nanotubes.

### 3.2. Effect of the laser excitation energy on the Raman modes of MWCNTs

One of the striking features of the Raman spectra of  $\text{sp}^2$  carbon materials is the linear laser excitation energy dependence of the wavenumber of the D and  $G'$  bands. Their strong dispersive behavior has been largely discussed in the literature [12–17] and inter-

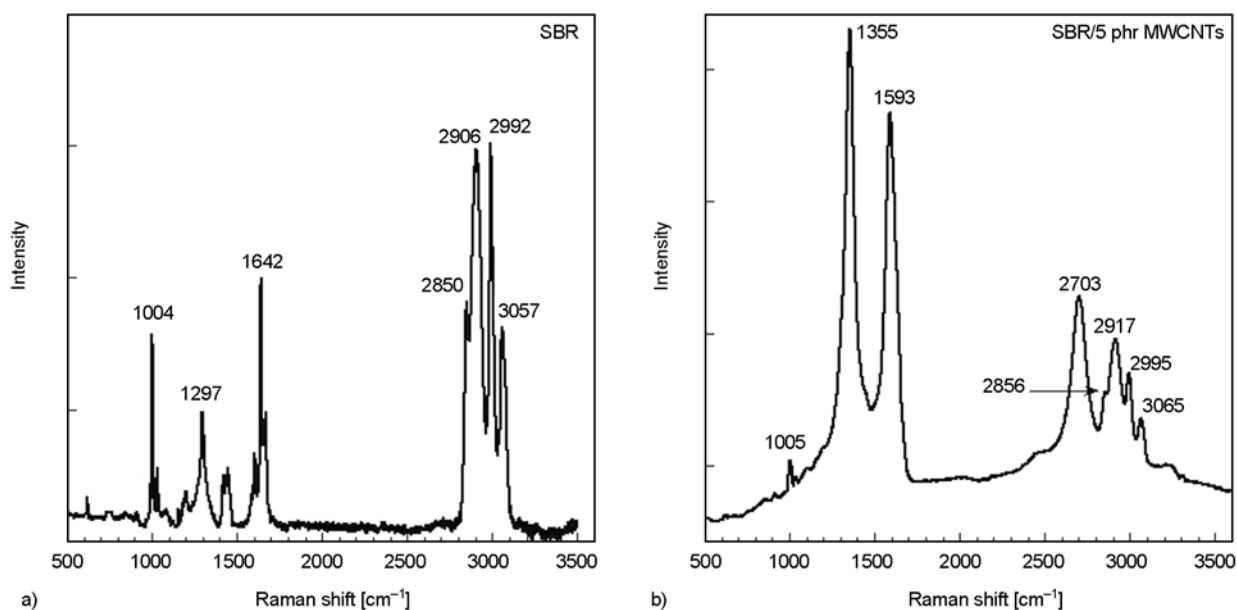


**Figure 3.** Raman spectra of a styrene-butadiene rubber (SBR) (a) and that of a SBR composite filled with 5 phr of MWCNTs (b)



preted as a double resonance process involving a laser-induced resonant transition of an electron

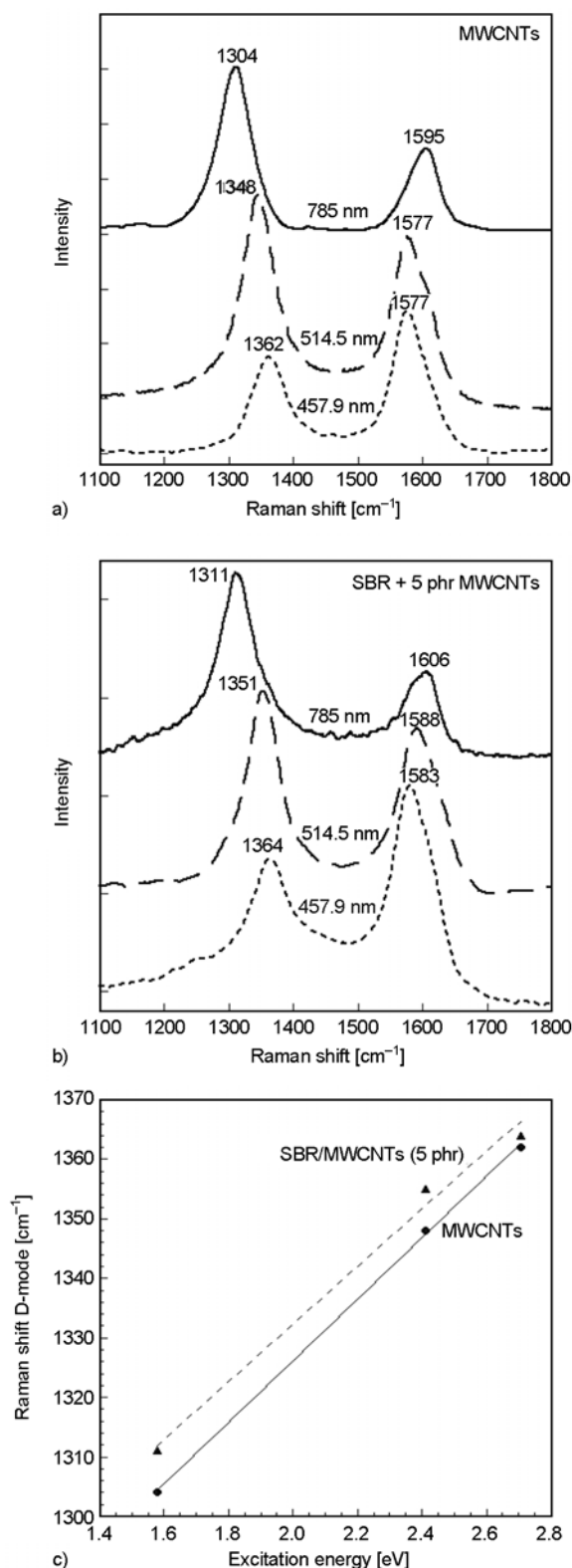


**Figure 4.** Raman spectra of MWCNTs (a) and of SBR-5 phr MWCNTs composite (b) obtained with laser wavelengths 457.9, 514.5 and 785 nm and dependence of the wavenumber of the D band on laser energy (c)

from the valence to the conduction band of carbon materials. A scattered resonance can take place if the electron is scattered by a phonon to a real state and after an elastic scattering process by lattice defects, the electron relaxes to the valence band [26]. Resonant Raman scattering is characterized by a strong enhancement of the detected signal when real transitions are involved. The conceptual difference between non-resonant, single-resonance and double-resonance Raman processes has been well explained by Thomsen *et al.* [27].

Figure 4 shows the Raman spectra of MWCNTs and of the SBR/5 phr MWCNTs composite obtained with three different laser excitation energies. For laser excitation variation, we have used the 457.9 nm (2.71 eV) and 514.5 nm (2.41 eV) lines from an Argon ion laser and the 785 nm (1.58 eV) of a NIR diode laser. As observed in single-walled carbon nanotubes (SWCNTs), the wavenumber of the D band increases while the ratio of the intensities ( $I_D/I_G$ ) decreases with increasing laser energy. The energy dependence of  $\approx 50 \text{ cm}^{-1}/\text{eV}$  (Figure 4) compared well with the reported values of various authors in the literature [13, 15, 17]. Interestingly, a similar dispersive behavior is observed for the D band of the nanotubes in the elastomeric matrix although higher wavenumbers are obtained for each excitation energy.

### 3.3. Thermal effects caused by incident laser irradiation

Heating effects induced by the laser power of the Raman experiment have been shown to cause changes to the Raman spectrum of CNTs. Increases of the incident laser power induce corresponding increases in the temperature of CNTs resulting in the shift to lower frequency for the radial breathing mode and the G band in SWCNTs [18] and for all the bands in MWCNTs [28]. Li *et al.* [18] suggest that the ability to induce the temperature increase in carbonaceous materials originates from the presence of impurities, defects and disorder in the samples. On the other hand, it has also been shown that electrical heating induce downshifts in the Raman frequencies, basically identical to those obtained by laser illumination thus indicating that the change in the Raman spectrum originates from laser-induced heating effect. Zhang *et al.* [19] show that under intense laser irradiation, the G band frequency of

unpurified SWCNTs undergoes reversible variation indicating that the tubes were not damaged in the irradiation process. In addition, the integrated D and G bands intensities ratio ( $I_D/I_G$ ) decreases rapidly in the initial increase in laser power but remains basically unchanged in the subsequent increase in laser power indicating a lowering in the degree of disorder. The authors conclude that intense laser irradiation can lead to the loss of impurities and results in a purified CNT sample. In a study by Raman spectroscopy on the stability of carbon nanotubes to laser irradiation, Olevik *et al.* [29] mention the particular sensitivity of CNT bundle materials to overheating due to inefficient cooling in this system compared to individual CNTs and show that irreversible destruction of CNTs in the bundles can occur at even low laser power density ( $0.15 \text{ kW/cm}^2$ ). From the above reported results, it appears that laser induced effects are very important to consider for the analysis of the Raman spectrum of CNTs. Heating the sample by the incident laser radiation may cause reversible changes but the original spectrum may not be recovered upon a decrease of the laser power owing to a damage of the tubes. The frequency downshifts induced by the local increase of the sample temperature due to laser irradiation have been associated with a lengthening of the C–C bond resulting from the thermal expansion of the material [30]. Nevertheless, changes in resonance conditions, softening of the intra-tubular van der

Waals interactions or thermal expansion of the bundles are other reasons invoked to account for the dependence of Raman spectra on increasing temperatures [20, 31].

We report here a study of the influence of laser irradiation on the Raman spectra of MWCNTs and of MWCNTs/SBR composites. We have used five laser power levels in this study corresponding to 1, 10, 25, 50 and 100% of the highest laser power which is 10 mW. In order to check if laser irradiation causes reversible effects, the spectra were first taken at the lowest laser power (1%) then the laser power was gradually increased to 100% then decreased to 1% again.

The Raman spectra of MWCNTs irradiated with various laser powers at 514.5 nm are shown in Figure 5. The overall Raman signal increases with the laser power but as shown in Figure 6, downshifts of both D and G frequencies are observed with increased laser power. The spectral variations induced by laser heating are reversible, which means that the nanotubes are not damaged by the irradiation process. A difference in the peak position is obtained for the lowest laser power on account of the poor Raman signal and less accuracy in the determination of the wavenumbers.

A thermogravimetric analysis performed on MWCNTs from room temperature to  $800^\circ\text{C}$  leaves a residue that displays a Raman spectrum quite similar to that observed in Figure 1 with D and G bands respec-

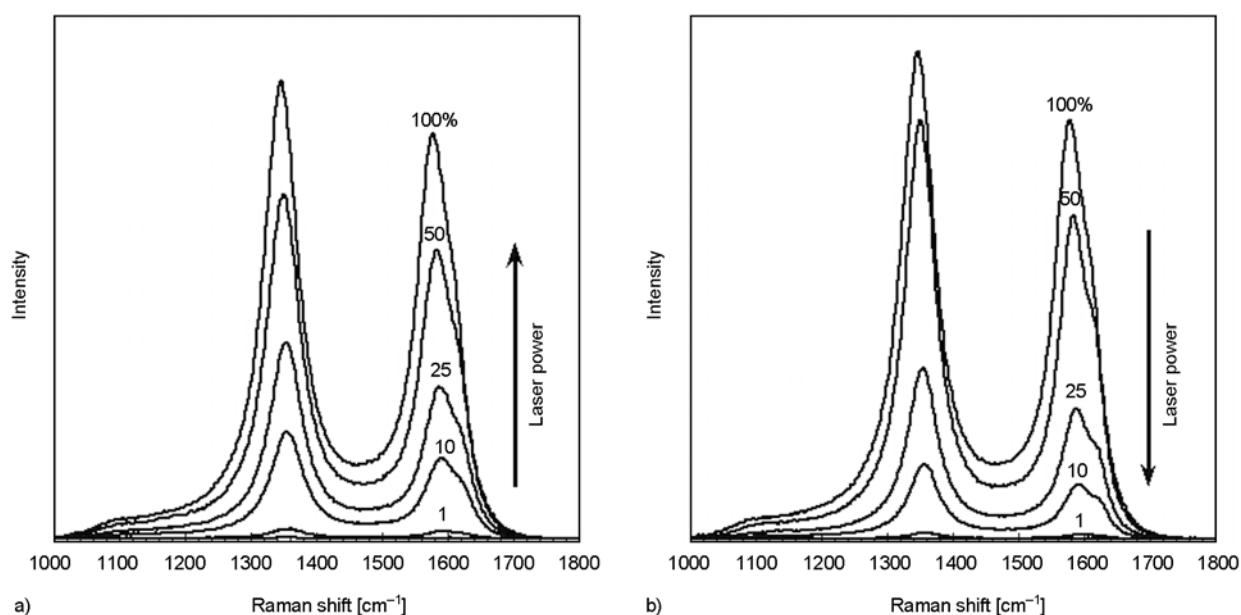


**Figure 5.** Raman spectra of MWCNTs samples irradiated at 514 nm taken at increasing laser power from 1 to 100%·10 mW (a) and decreasing laser power from 100 to 1%·10 mW (b)

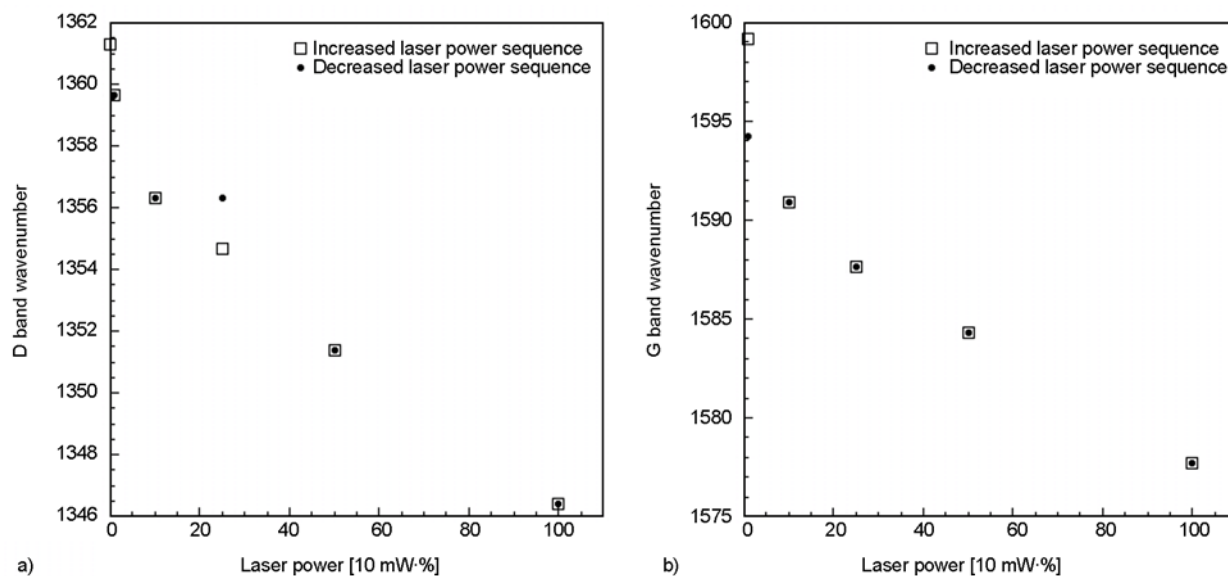


**Figure 6.** Laser power dependences of the D (a) and G (b) bands of MWCNTs

tively located at 1351 and 1588  $\text{cm}^{-1}$ . This result shows that heating the nanotubes does not destroy them which confirms the spectroscopic analysis if, of course, Raman changes under laser irradiation are induced by heating effects.

Raman spectra were also taken at the same spot on SBR/MWCNTs composites for different laser power densities going from low to higher power densities. But for each sample, several experiments at different spots were performed in order to confirm the results. Features of interest are the positions of the D and G bands that downshift, as for non-embedded MWCNTs (Figure 6), with increasing laser power

and the laser-induced frequency shifts are reversible. More surprising is the fact that above a given laser power (10 mW·25% in the spectra of the SBR/5 phr MWCNTs represented Figure 7a), the intensity of the D band becomes lower than that of the G band. The D band remains less intense than the G band upon further increase of the laser power and also after progressive decrease of the laser power from the highest value (Figure 7b). This can be visualized by looking at the dependence of the  $I_D/I_G$  ratio on the laser power represented in Figure 8.  $I_D/I_G$  decreases rapidly with increasing laser power but remains almost unchanged in the subsequent

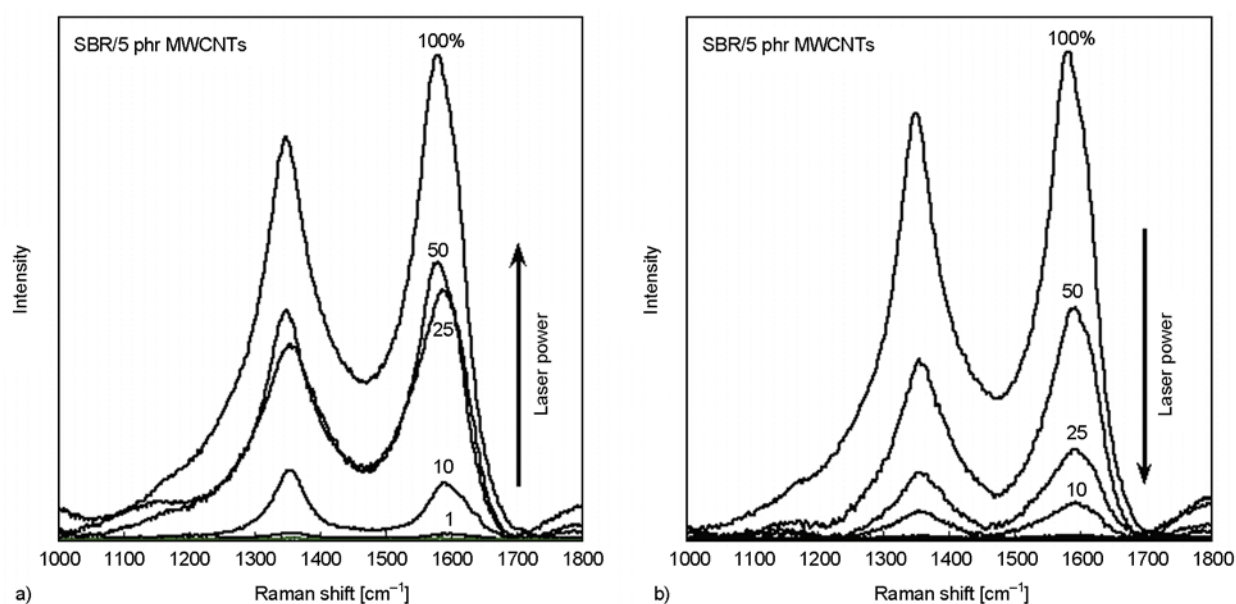


**Figure 7.** Raman spectra of the SBR/5 phr MWCNTs composite irradiated at 514.5 nm taken at increasing (a) and decreasing (b) laser power [10 mW-%]

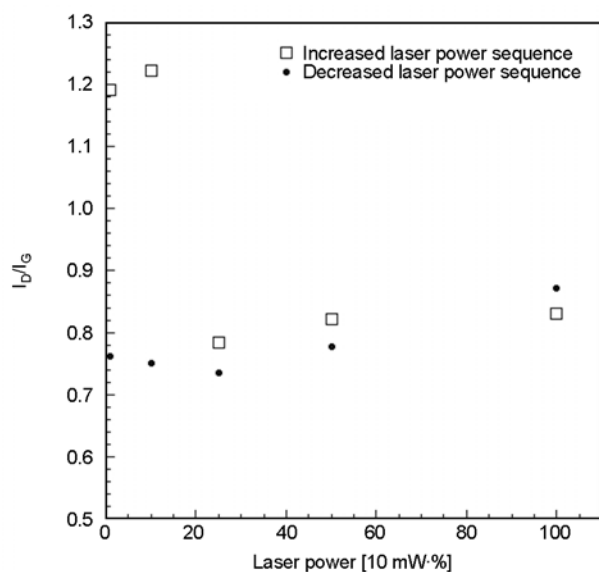


**Figure 8.** Dependence of the  $I_D/I_G$  ratio of the SBR/5 phr MWCNTs composite on the laser power

increase. In contrast,  $I_D/I_G$  is almost unchanged in the decreasing laser power cycle. This result is quite similar to that obtained by Zhang *et al.* [19] in a study devoted to the effects of intense laser irradiation on Raman intensity features of SWCNTs. As the  $I_D/I_G$  ratio reflects the degree of disorder, the authors conclude that the irreversible change in intensity resulting from intense laser irradiation originates from sample purification. But why the change in intensity of the D band only occurs in the MWCNT composites and not in non-embedded MWCNTs?

We think that overheating effects due to laser irradiation are probably more important in the composites on account of the low thermal conductivity of the surrounding matrix. Despite the high thermal conductivity of individual nanotubes – around  $6000 \text{ W}/(\text{m}\cdot\text{K})$  for SWCNTs) and around  $3000 \text{ W}/(\text{m}\cdot\text{K})$  for MWCNTs [32], the SBR matrix can be considered as a thermal insulator since its thermal conductivity, around  $0.120 \text{ W}/(\text{m}\cdot\text{K})$ , is only enhanced by 70% by addition of 10 phr of MWCNTs. So the heat generated by light illumination is not dissipated resulting in high temperature increase of nanotube and purification.

#### 4. Conclusions

In this work, Raman spectroscopy has proved to be a convenient and useful method for carbon nanotube characterization. Nevertheless local increase of the sample temperature due to laser irradiation

may cause irreversible changes in the Raman spectra making difficult the correct spectra acquisition and interpretation.

#### References

- [1] Andrews R., Weisenberger M. C.: Carbon nanotube polymer composites. *Current Opinion in Solid State and Materials Science*, **8**, 31–37 (2004). DOI: [10.1016/j.cossms.2003.10.006](https://doi.org/10.1016/j.cossms.2003.10.006)
- [2] Hu Y., Shenderova O. A., Hu Z., Padgett C. W., Brenner D. W.: Carbon nanostructures for advanced composites. *Reports on Progress in Physics*, **69**, 1847–1895 (2006). DOI: [10.1088/0034-4885/69/6/R05](https://doi.org/10.1088/0034-4885/69/6/R05)
- [3] Coleman J. N., Khan U., Blau W. J., Gun'ko Y. K.: Small but strong: A review of the mechanical properties of carbon nanotube–polymer composites. *Carbon*, **44**, 1624–1652 (2006). DOI: [10.1016/j.carbon.2006.02.038](https://doi.org/10.1016/j.carbon.2006.02.038)
- [4] Moniruzzaman M., Winey K. I.: Polymer nanocomposites containing carbon nanotubes. *Macromolecules*, **39**, 5194–5205 (2006). DOI: [10.1021/ma060733p](https://doi.org/10.1021/ma060733p)
- [5] Bokobza L.: Multiwall carbon nanotube elastomeric composites: A review. *Polymer*, **48**, 4907–4920 (2007). DOI: [10.1016/j.polymer.2007.06.046](https://doi.org/10.1016/j.polymer.2007.06.046)
- [6] Spitalsky Z., Tasis D., Papagelis K., Galiotis C.: Carbon nanotube–polymer composites: Chemistry, processing, mechanical and electrical properties. *Progress in Polymer Science*, **35**, 357–401 (2010). DOI: [10.1016/j.progpolymsci.2009.09.003](https://doi.org/10.1016/j.progpolymsci.2009.09.003)
- [7] Dresselhaus M. S., Jorio A., Hofmann M., Dresselhaus G., Saito R.: Perspectives on carbon nanotubes and graphene Raman spectroscopy. *Nano Letters*, **10**, 751–758 (2010). DOI: [10.1021/nl904286r](https://doi.org/10.1021/nl904286r)
- [8] Jorio A., Pimenta M. A., Souza Filho A. G., Saito R., Dresselhaus G., Dresselhaus M. S.: Characterizing carbon nanotube samples with resonance Raman scattering. *New Journal of Physics*, **5**, 139/1–139/17 (2003). DOI: [10.1088/1367-2630/5/1/139](https://doi.org/10.1088/1367-2630/5/1/139)
- [9] Graupner R.: Raman spectroscopy of covalently functionalized single-wall carbon nanotubes. *Journal of Raman Spectroscopy*, **38**, 673–683 (2007). DOI: [10.1002/jrs.1694](https://doi.org/10.1002/jrs.1694)
- [10] Cuesta A., Dharmelincourt P., Laureyns J., Martínez-Alonso A., Tascón J. M. D.: Raman microprobe studies on carbon materials. *Carbon*, **32**, 1523–1532 (1994). DOI: [10.1016/0008-6223\(94\)90148-1](https://doi.org/10.1016/0008-6223(94)90148-1)
- [11] Rao A. M., Chen J., Richter E., Schlecht U., Eklund P. C., Haddon R. C., Venkateswaran U. D., Kwon Y-K., Tománek D.: Effect of van der Waals interactions on the Raman modes in single walled carbon nanotubes. *Physical Review Letters*, **86**, 3895–3898 (2001). DOI: [10.1103/PhysRevLett.86.3895](https://doi.org/10.1103/PhysRevLett.86.3895)



- [12] Pócsik I., Hundhausen M., Koós M., Ley L.: Origin of the D peak in the Raman spectrum of microcrystalline graphite. *Journal of Non-Crystalline Solids*, **227–230**, 1083–1086 (1998).  
DOI: [10.1016/S0022-3093\(98\)00349-4](https://doi.org/10.1016/S0022-3093(98)00349-4)
- [13] Matthews M. J., Pimenta M. A., Dresselhaus G., Dresselhaus M. S., Endo M.: Origin of dispersive effects of the Raman D band in carbon materials. *Physical Review B*, **59**, R6585–R6588 (1999).  
DOI: [10.1103/PhysRevB.59.R6585](https://doi.org/10.1103/PhysRevB.59.R6585)
- [14] Thomsen C., Reich S.: Double resonant Raman scattering in graphite. *Physical Review Letters*, **85**, 5214–5217 (2000).  
DOI: [10.1103/PhysRevLett.85.5214](https://doi.org/10.1103/PhysRevLett.85.5214)
- [15] Brown S. D. M., Jorio A., Dresselhaus M. S., Dresselhaus G.: Observations of the D-band feature in the Raman spectra of carbon nanotubes. *Physical Review B*, **64**, 073403/1–073403/4 (2001).  
DOI: [10.1103/PhysRevB.64.073403](https://doi.org/10.1103/PhysRevB.64.073403)
- [16] Sood A. K., Gupta R., Asher S. A.: Origin of the unusual dependence of Raman D band on excitation wavelength in graphite-like materials. *Journal of Applied Physics*, **90**, 4494–4497 (2001).  
DOI: [10.1063/1.1408590](https://doi.org/10.1063/1.1408590)
- [17] Kürti J., Zólyomi V., Grüneis A., Kuzmany H.: Double resonant Raman phenomena enhanced by van Hove singularities in single-wall carbon nanotubes. *Physical Review B*, **65**, 165433/1–165433/9 (2002).  
DOI: [10.1103/PhysRevB.65.165433](https://doi.org/10.1103/PhysRevB.65.165433)
- [18] Li H. D., Yue K. T., Lian Z. L., Zhan Y., Zhou L. X., Zhang S. L., Shi Z. J., Gu Z. N., Liu B. B., Yang R. S., Yang H. B., Zou G. T., Zhang Y., Iijima S.: Temperature dependence of the Raman spectra of single-wall carbon nanotubes. *Applied Physics Letters*, **76**, 2053–2055 (2000).  
DOI: [10.1063/1.126252](https://doi.org/10.1063/1.126252)
- [19] Zhang L., Li H., Yue K.-T., Zhang S.-L., Wu X., Zi J., Shi Z., Gu Z.: Effects of intense laser irradiation on Raman intensity features of carbon nanotubes. *Physical Review B*, **65**, 073401/1–073401/4 (2002).  
DOI: [10.1103/PhysRevB.65.073401](https://doi.org/10.1103/PhysRevB.65.073401)
- [20] Zhou Z., Dou X., Ci L., Song L., Liu D., Gao Y., Wang J., Liu L., Zhou W., Xie S., Wan D.: Temperature dependence of the Raman spectra of individual carbon nanotubes. *Journal of Physical Chemistry B*, **110**, 1206–1209 (2006).  
DOI: [10.1021/jp053268r](https://doi.org/10.1021/jp053268r)
- [21] Zhang Y., Son H., Zhang J., Kong J., Liu Z.: Laser-heating effect on Raman spectra of individual suspended single-walled carbon nanotubes. *Journal of Physical Chemistry C*, **111**, 1988–1992 (2007).  
DOI: [10.1021/jp066016e](https://doi.org/10.1021/jp066016e)
- [22] Zhao Q., Wagner H. D.: Raman spectroscopy of carbon–nanotube–based composites. *Philosophical Transactions of the Royal Society A: Mathematical, Physical and Engineering Sciences*, **362**, 2407–2424 (2004).  
DOI: [10.1098/rsta.2004.1447](https://doi.org/10.1098/rsta.2004.1447)
- [23] Kao C. C., Young R. J.: A Raman spectroscopic investigation of heating effects and the deformation behaviour of epoxy/SWNT composites. *Composites Science and Technology*, **64**, 2291–2295 (2004).  
DOI: [10.1016/j.compscitech.2004.01.019](https://doi.org/10.1016/j.compscitech.2004.01.019)
- [24] Kannan P., Eichhorn S. J., Young R. J.: Deformation of isolated single-wall carbon nanotubes in electrospun polymer nanofibres. *Nanotechnology*, **18**, 235707/1–235707/7 (2007).  
DOI: [10.1088/0957-4484/18/23/235707](https://doi.org/10.1088/0957-4484/18/23/235707)
- [25] Mu M., Osswald S., Gogotsi Y., Winey K. I.: An *in situ* Raman spectroscopy study of stress transfer between carbon nanotubes and polymer. *Nanotechnology*, **20**, 335703/1–335703/7 (2009).  
DOI: [10.1088/0957-4484/20/33/335703](https://doi.org/10.1088/0957-4484/20/33/335703)
- [26] Reich S., Thomsen C.: Raman spectroscopy of graphite. *Philosophical Transactions of the Royal Society A: Mathematical, Physical and Engineering Sciences*, **362**, 2271–2288 (2004).  
DOI: [10.1098/rsta.2004.1454](https://doi.org/10.1098/rsta.2004.1454)
- [27] Thomsen C., Reich S., Maultzsch J.: Resonant Raman spectroscopy of nanotubes. *Philosophical Transactions of the Royal Society A: Mathematical, Physical and Engineering Sciences*, **362**, 2337–2359 (2004).  
DOI: [10.1098/rsta.2004.1444](https://doi.org/10.1098/rsta.2004.1444)
- [28] Huang F., Yue K. T., Tan P., Zhang S.-L., Shi Z., Zhou X., Gu Z.: Temperature dependence of the Raman spectra of carbon nanotubes. *Journal of Applied Physics*, **84**, 4022–4024 (1998).  
DOI: [10.1063/1.368585](https://doi.org/10.1063/1.368585)
- [29] Olevik D., Soldatov A. V., Dossot M., Vigolo B., Humbert B., McRae E.: Stability of carbon nanotubes to laser irradiation probed by Raman spectroscopy. *Physica Status Solidi B*, **245**, 2212–2215 (2008).  
DOI: [10.1002/pssb.200879661](https://doi.org/10.1002/pssb.200879661)
- [30] Huong P. V., Cavagnat R., Ajayan P. M., Stephan O.: Temperature-dependent vibrational spectra of carbon nanotubes. *Physical Review B*, **51**, 10048–10051 (1995).  
DOI: [10.1103/PhysRevB.51.10048](https://doi.org/10.1103/PhysRevB.51.10048)
- [31] Meletov K. P., Krestinin A. V., Arvanitidis J., Christofilos D., Kourouklis G. A.: Temperature effects in the Raman spectra of bundled single-wall carbon nanotubes. *Chemical Physics Letters*, **477**, 336–339 (2009).  
DOI: [10.1016/j.cplett.2009.07.001](https://doi.org/10.1016/j.cplett.2009.07.001)
- [32] Hone J., Whitney M., Piskoti C., Zettl A.: Thermal conductivity of single-walled carbon nanotubes. *Physical Review B*, **59**, R2514–R2516 (1999).  
DOI: [10.1103/PhysRevB.59.R2514](https://doi.org/10.1103/PhysRevB.59.R2514)